WVMP SAR Reference 3-13

CRC Handbook of Chemistry and Physics, 75th ed., Chapter 5, CRC Press, Boca Raton, Florida, 1994.

STANDARD THERMODYNAMIC PROPERTIES OF CHEMICAL SUBSTANCES (continued)

Molecular formula	Name	State	$\Delta_f H°$ kJ/mol	$\Delta_f G°$ kJ/mol	$S°$ J/mol K	C_p J/mol K
$AlCl_3$	Aluminum trichloride	cry	–704.2	–628.8	110.7	91.8
		gas	–583.2			
AlF	Aluminum fluoride (AlF)	gas	–258.2	–283.7	215.0	31.9
AlF_3	Aluminum trifluoride	cry	–1510.4	–1431.1	66.5	75.1
		gas	–1204.6	–1188.2	277.1	62.6
AlF_4Na	Sodium tetrafluoroaluminate	gas	–1869.0	–1827.5	345.7	105.9
AlH	Aluminum hydride (AlH)	gas	259.2	231.2	187.9	29.4
AlH_3	Aluminum hydride (AlH_3)	cry	–46.0			
AlH_4K	Potassium tetrahydroaluminate	cry	–183.7			
AlH_4Li	Lithium tetrahydroaluminate	cry	–116.3	–44.7	78.7	83.2
AlI	Aluminum iodide (AlI)	gas	65.5			36.0
AlI_3	Aluminum triiodide	cry	–313.8	–300.8	159.0	98.7
		gas	–207.5			
AlN	Aluminum nitride (AlN)	cry	–318.0	–287.0	20.2	30.1
AlO	Aluminum oxide (AlO)	gas	91.2	65.3	218.4	30.9
AlO_4P	Aluminum phosphate ($AlPO_4$)	cry	–1733.8	–1617.9	90.8	93.2
AlP	Aluminum phosphide (AlP)	cry	–166.5			
AlS	Aluminum sulfide (AlS)	gas	200.9	150.1	230.6	33.4
Al_2	Aluminum (Al_2)	gas	485.9	433.3	233.2	36.4
Al_2Br_6	Aluminum hexabromide	gas	–970.7			
Al_2Cl_6	Aluminum hexachloride	gas	–1290.8	–1220.4	490.0	
Al_2F_6	Aluminum hexafluoride	gas	–2628.0			
Al_2I_6	Aluminum hexaiodide	gas	–516.7			
Al_2O	Aluminum oxide (Al_2O)	gas	–130.0	–159.0	259.4	45.7
Al_2O_3	Aluminum oxide (Al_2O_3)	cry	–1675.7	–1582.3	50.9	79.0
Al_2S_3	Aluminum sulfide (Al_2S_3)	cry	–724.0			
Am	Americium	cry	0.0			
Ar	Argon	gas	0.0		154.8	20.8
As	Arsenic (gray)	cry	0.0		35.1	24.6
	Arsenic (yellow)	cry	14.6			
		gas	302.5	261.0	174.2	20.8
$AsBr_3$	Arsenic tribromide	cry	–197.5			
		gas	–130.0	–159.0	363.9	79.2
$AsCl_3$	Arsenic trichloride	liq	–305.0	–259.4	216.3	
		gas	–261.5	–248.9	327.2	75.7
AsF_3	Arsenic trifluoride	liq	–821.3	–774.2	181.2	126.6
		gas	–785.8	–770.8	289.1	65.6
AsGa	Gallium arsenide (GaAs)	cry	–71.0	–67.8	64.2	46.2
AsH_3	Arsine	gas	66.4	68.9	222.8	38.1
AsH_3O_4	Arsenic acid (H_3AsO_4)	cry	–906.3			
AsI_3	Arsenic triiodide	cry	–58.2	–59.4	213.1	105.8
		gas			388.3	80.6
AsIn	Indium arsenide (InAs)	cry	–58.6	–53.6	75.7	47.8
AsO	Arsenic oxide (AsO)	gas	70.0			
As_2	Arsenic (As_2)	gas	222.2	171.9	239.4	35.0
As_2O_5	Arsenic pentoxide (As_2O_5)	cry	–924.9	–782.3	105.4	116.5
As_2S_3	Arsenic trisulfide (As_2S_3)	cry	–169.0	–168.6	163.6	116.3
At	Astatine	cry	0.0			
Au	Gold	cry	0.0		47.4	25.4
		gas	366.1	326.3	180.5	20.8
AuBr	Gold bromide (AuBr)	cry	–14.0			
$AuBr_3$	Gold bromide ($AuBr_3$)	cry	–53.3			
AuCl	Gold chloride (AuCl)	cry	–34.7			
$AuCl_3$	Gold chloride ($AuCl_3$)	cry	–117.6			
AuF_3	Gold fluoride (AuF_3)	cry	–363.6			
AuH	Gold hydride (AuH)	gas	295.0	265.7	211.2	29.2
AuI	Gold iodide (AuI)	cry	0.0			

STANDARD THERMODYNAMIC PROPERTIES OF CHEMICAL SUBSTANCES (continued)

Molecular formula	Name	State	$\Delta_f H°$ kJ/mol	$\Delta_f G°$ kJ/mol	$S°$ J/mol K	C_p J/mol K
Br_4Ti	Titanium bromide ($TiBr_4$)	cry	−616.7	−589.5	243.5	131.5
		gas	−549.4	−568.2	398.4	100.8
Br_4V	Vanadium bromide (VBr_4)	gas	−336.8			
Br_4Zr	Zirconium bromide ($ZrBr_4$)	cry	−760.7			
Br_5P	Phosphorus pentabromide	cry	−269.9			
Br_5Ta	Tantalum bromide ($TaBr_5$)	cry	−598.3			
Br_6W	Tungsten bromide (WBr_6)	cry	−348.5			
Ca	Calcium	cry	0.0		41.6	25.9
		gas	177.8	144.0	154.9	20.8
$CaCl_2$	Calcium chloride	cry	−795.4	−748.8	108.4	72.9
CaF_2	Calcium fluoride	cry	−1228.0	−1175.6	68.5	67.0
CaH_2	Calcium hydride (CaH_2)	cry	−181.5	−142.5	41.4	41.0
CaH_2O_2	Calcium hydroxide	cry	−985.2	−897.5	83.4	87.5
CaI_2	Calcium iodide	cry	−533.5	−528.9	142.0	
CaN_2O_6	Calcium nitrate	cry	−938.2	−742.8	193.2	149.4
CaO	Calcium oxide	cry	−634.9	−603.3	38.1	42.0
CaO_4S	Calcium sulfate	cry	−1434.5	−1322.0	106.5	99.7
CaS	Calcium sulfide	cry	−482.4	−477.4	56.5	47.4
$Ca_3O_8P_2$	Calcium phosphate	cry	−4120.8	−3884.7	236.0	227.8
Cd	Cadmium	cry	0.0		51.8	26.0
		gas	111.8		167.7	20.8
$CdCl_2$	Cadmium chloride	cry	−391.5	−343.9	115.3	74.7
CdF_2	Cadmium fluoride	cry	−700.4	−647.7	77.4	
CdH_2O_2	Cadmium hydroxide	cry	−560.7	−473.6	96.0	
CdI_2	Cadmium iodide	cry	−203.3	−201.4	161.1	80.0
CdO	Cadmium oxide	cry	−258.4	−228.7	54.8	43.4
CdO_4S	Cadmium sulfate	cry	−933.3	−822.7	123.0	99.6
CdS	Cadmium sulfide	cry	−161.9	−156.5	64.9	
CdTe	Cadmium telluride	cry	−92.5	−92.0	100.0	
Ce	Cerium	cry	0.0		72.0	26.9
		gas	423.0	385.0	191.8	23.1
$CeCl_3$	Cerium chloride ($CeCl_3$)	cry	−1053.5	−977.8	151.0	87.4
CeO_2	Cerium oxide (CeO_2)	cry	−1088.7	−1024.6	62.3	61.6
CeS	Cerium sulfide (CeS)	cry	−459.4	−451.5	78.2	50.0
Ce_2O_3	Cerium oxide (Ce_2O_3)	cry	−1796.2	−1706.2	150.6	114.6
Cf	Californium	cry	0.0			
Cl	Chlorine	gas	121.3	105.3	165.2	21.8
ClCs	Cesium chloride	cry	−443.0	−414.5	101.2	52.5
$ClCsO_4$	Cesium perchlorate	cry	−443.1	−314.3	175.1	108.3
ClCu	Copper chloride (CuCl)	cry	−137.2	−119.9	86.2	48.5
ClF	Chlorine fluoride	gas	−50.3	−51.8	217.9	32.1
$ClFO_3$	Perchloryl fluoride	gas	−23.8	48.2	279.0	64.9
ClGe	Germanium chloride (GeCl)	gas	155.2	124.2	247.0	36.9
ClF_3	Chlorine trifluoride	liq	−189.5			
		gas	−163.2	−123.0	281.6	63.9
ClF_5S	Sulfur chloride pentafluoride	liq	−1065.7			
$ClGeH_3$	Chlorogermane	gas			263.7	54.7
ClH	Hydrogen chloride	gas	−92.3	−95.3	186.9	29.1
ClHO	Hypochlorous acid (HOCl)	gas	−78.7	−66.1	236.7	37.2
$ClHO_4$	Perchloric acid	liq	−40.6			
ClH_3Si	Chlorosilane	gas			250.7	51.0
ClH_4N	Ammonium chloride	cry	−314.4	−202.9	94.6	84.1
ClH_4NO_4	Ammonium perchlorate	cry	−295.3	−88.8	186.2	
ClH_4P	Phosphonium chloride	cry	−145.2			
ClI	Iodine chloride	liq	−23.9	−13.6	135.1	
		gas	17.8	−5.5	247.6	35.6
ClIn	Indium chloride (InCl)	cry	−186.2			

Molecular formula	Name	State	$\Delta_f H°$ kJ/mol	$\Delta_f G°$ kJ/mol	$S°$ J/mol K	C_p J/mol K
		gas	−374.9	−305.0	364.6	112.8
Cl_5Pa	Protactinium chloride ($PaCl_5$)	cry	−1145.0	−1034.0	238.0	
Cl_5Ta	Tantalum chloride ($TaCl_5$)	cry	−859.0			
Cl_6U	Uranium chloride (UCl_6)	cry	−1092.0	−962.0	285.8	
		gas	−1013.0	−928.0	431.0	175.7
Cl_6W	Tungsten chloride (WCl_6)	cry	−602.5			
		gas	−513.8			
Cm	Curium	cry	0.0			
Co	Cobalt	cry	0.0		30.0	
		gas	424.7	380.3	179.5	24.8
CoF_2	Cobalt fluoride (CoF_2)	cry	−692.0	−647.2	82.0	23.0
CoH_2O_2	Cobalt hydroxide ($Co(OH)_2$)	cry	−539.7	−454.3	79.0	68.3
CoI_2	Cobalt iodide (CoI_2)	cry	−88.7			
CoN_2O_6	Cobalt nitrate ($Co(NO_3)_2$)	cry	−420.5			
CoO	Cobalt oxide (CoO)	cry	−237.9	−214.2	53.0	55.2
CoO_4S	Cobalt sulfate ($CoSO_4$)	cry	−888.3	−782.3	118.0	
CoS	Cobalt sulfide (CoS)	cry	−82.8			
Co_2S_3	Cobalt sulfide (Co_2S_3)	cry	−147.3			
Co_3O_4	Cobalt oxide (Co_3O_4)	cry	−891.0	−774.0	102.5	123.4
Cr	Chromium	cry	0.0		23.8	23.4
		gas	396.6	351.8	174.5	20.8
CrF_2	Chromium fluoride (CrF_2)	cry	−778.0			
CrF_3	Chromium fluoride (CrF_3)	cry	−1159.0	−1088.0	93.9	78.7
CrI_2	Chromium iodide (CrI_2)	cry	−156.9			
CrI_3	Chromium iodide (CrI_3)	cry	−205.0			
CrO_2	Chromium oxide (CrO_2)	cry	−598.0			
CrO_4Pb	Lead chromate ($PbCrO_4$)	cry	−930.9			
Cr_2FeO_4	Chromium iron oxide ($FeCr_2O_4$)	cry	−1444.7	−1343.8	146.0	133.6
Cr_2O_3	Chromium oxide (Cr_2O_3)	cry	−1139.7	−1058.1	81.2	118.7
Cr_3O_4	Chromium oxide (Cr_3O_4)	cry	−1531.0			
Cs	Cesium	cry	0.0		85.2	32.2
		gas	76.5	49.6	175.6	20.8
CsF	Cesium fluoride	cry	−553.5	−525.5	92.8	51.1
CsF_2H	Cesium hydrogen fluoride ($CsHF_2$)	cry	−923.8	−858.9	135.2	87.9
CsH	Cesium hydride	cry	−54.2			
CsHO	Cesium hydroxide	cry	−417.2			
$CsHO_4S$	Cesium hydrogen sulfate	cry	−1158.1			
CsH_2N	Cesium amide	cry	−118.4			
CsI	Cesium iodide	cry	−346.6	−340.6	123.1	52.8
$CsNO_3$	Cesium nitrate	cry	−506.0	−406.5	155.2	
CsO_2	Cesium superoxide (CsO_2)	cry	−286.2			
Cs_2O	Cesium oxide (Cs_2O)	cry	−345.8	−308.1	146.9	76.0
Cs_2O_3S	Cesium sulfite	cry	−1134.7			
Cs_2O_4S	Cesium sulfate	cry	−1443.0	−1323.6	211.9	134.9
Cs_2S	Cesium sulfide (Cs_2S)	cry	−359.8			
Cu	Copper	cry	0.0		33.2	24.4
		gas	337.4	297.7	166.4	20.8
CuF_2	Copper fluoride (CuF_2)	cry	−542.7			
CuH_2O_2	Copper hydroxide ($Cu(OH)_2$)	cry	−449.8			
CuI	Copper iodide (CuI)	cry	−67.8	−69.5	96.7	54.1
CuN_2O_6	Copper nitrate ($Cu(NO_3)_2$)	cry	−302.9			
CuO	Copper oxide (CuO)	cry	−157.3	−129.7	42.6	42.3
CuO_4S	Copper sulfate ($CuSO_4$)	cry	−771.4	−662.2	109.2	
CuO_4W	Copper tungstate ($CuWO_4$)	cry	−1105.0			
CuS	Copper sulfide (CuS)	cry	−53.1	−53.6	66.5	47.8
CuSe	Copper selenide (CuSe)	cry	−39.5			
Cu_2	Copper (Cu_2)	gas	484.2	431.9	241.6	96.6

Molecular formula	Name	State	$\Delta_f H°$ kJ/mol	$\Delta_f G°$ kJ/mol	$S°$ J/mol K	C_p J/mol K
FeO	Iron oxide (FeO)	cry	−272.0			
FeO_4S	Iron sulfate ($FeSO_4$)	cry	−928.4	−820.8	107.5	100.6
FeO_4W	Iron tungstate ($FeWO_4$)	cry	−1155.0	−1054.0	131.8	114.6
FeS	Iron sulfide (FeS)	cry	−100.0	−100.4	60.3	50.5
FeS_2	Iron sulfide (FeS_2)	cry	−178.2	−166.9	52.9	62.2
Fe_2O_3	Iron oxide (Fe_2O_3)	cry	−824.2	−742.2	87.4	103.9
Fe_2O_4Si	Iron silicate (Fe_2SiO_4)	cry	−1479.9	−1379.0	145.2	132.9
Fe_3O_4	Iron oxide (Fe_3O_4)	cry	−1118.4	−1015.4	146.4	143.4
Fm	Fermium	cry	0.0			
Fr	Francium	cry	0.0		95.4	
Ga	Gallium	cry	0.0		40.9	25.9
		liq	5.6			
		gas	277.0	238.9	169.1	25.4
GaH_3O_3	Gallium hydroxide ($Ga(OH)_3$)	cry	−964.4	−831.3	100.0	
GaN	Gallium nitride (GaN)	cry	−110.5			
GaO	Gallium oxide (GaO)	gas	279.5	253.5	231.1	32.1
GaP	Gallium phosphide (GaP)	cry	−88.0			
GaSb	Gallium antimonide (GaSb)	cry	−41.8	−38.9	76.1	48.5
Ga_2	Gallium (Ga_2)	gas	438.5			
Ga_2O	Gallium oxide (Ga_2O)	cry	−356.0			
Ga_2O_3	Gallium oxide (Ga_2O_3)	cry	−1089.1	−998.3	85.0	92.1
Gd	Gadolinium	cry	0.0		68.1	37.0
		gas	397.5	359.8	194.3	27.5
Gd_2O_3	Gadolinium oxide (Gd_2O_3)	cry	−1819.6			106.7
Ge	Germanium	cry	0.0		31.1	23.3
		gas	372.0	331.2	167.9	30.7
GeH_3I	Iodogermane	gas			283.2	57.5
GeH_4	Germane	gas	90.8	113.4	217.1	45.0
GeI_4	Germanium tetraiodide	cry	−141.8	−144.3	271.1	
		gas	−56.9	−106.3	428.9	104.1
GeO	Germanium oxide (GeO) (brown)	cry	−261.9	−237.2	50.0	
		gas	−46.2	−73.2	224.3	30.9
GeO_2	Germanium dioxide (tetragonal)	cry	−580.0	−521.4	39.7	52.1
GeP	Germanium phosphide (GeP)	cry	−21.0	−17.0	63.0	
GeS	Germanium sulfide (GeS)	cry	−69.0	−71.5	71.0	
		gas	92.0	42.0	234.0	33.7
Ge_2	Germanium (Ge_2)	gas	473.1	416.3	252.8	35.6
Ge_2H_6	Digermane	liq	137.3			
		gas	162.3			
Ge_3H_8	Trigermane	liq	193.7			
		gas	226.8			
H	Hydrogen	gas	218.0	203.3	114.7	20.8
HI	Hydrogen iodide	gas	26.5	1.7	206.6	29.2
HIO_3	Iodic acid	cry	−230.1			
HK	Potassium hydride	cry	−57.7			
HKO	Potassium hydroxide	cry	−424.8	−379.1	78.9	64.9
HKO_4S	Potassium hydrogen sulfate	cry	−1160.6	−1031.3	138.1	
HLi	Lithium hydride	cry	−90.5	−68.3	20.0	27.9
HLiO	Lithium hydroxide	cry	−484.9	−439.0	42.8	49.7
HN	Imidogen (NH)	gas	351.5	345.6	181.2	29.2
HNO_2	Nitrous acid (HONO)	gas	−79.5	−46.0	254.1	45.6
HNO_3	Nitric acid	liq	−174.1	−80.7	155.6	109.9
		gas	−135.1	−74.7	266.4	53.4
HN_3	Hydrazoic acid	liq	264.0	327.3	140.6	
		gas	294.1	328.1	239.0	43.7
HNa	Sodium hydride	cry	−56.3	−33.5	40.0	36.4
HNaO	Sodium hydroxide	cry	−425.6	−379.5	64.5	59.5

STANDARD THERMODYNAMIC PROPERTIES OF CHEMICAL SUBSTANCES (continued)

Molecular formula	Name	State	$\Delta_f H°$ kJ/mol	$\Delta_f G°$ kJ/mol	$S°$ J/mol K	C_p J/mol K
Li_2O_4S	Lithium sulfate	cry	−1436.5	−1321.7	115.1	117.6
Li_2S	Lithium sulfide (Li_2S)	cry	−441.4			
Li_3O_4P	Lithium phosphate	cry	−2095.8			
Lr	Lawrencium	cry	0.0			
Lu	Lutetium	cry	0.0		51.0	26.9
		gas	427.6	387.8	184.8	20.9
Lu_2O_3	Lutetium oxide (Lu_2O_3)	cry	−1878.2	−1789.0	110.0	101.8
Md	Mendelevium	cry	0.0			
Mg	Magnesium	cry	0.0		32.7	24.9
		gas	147.1	112.5	148.6	20.8
MgN_2O_6	Magnesium nitrate	cry	−790.7	−589.4	164.0	141.9
MgO	Magnesium oxide	cry	−601.6	−569.3	27.0	37.2
MgO_4S	Magnesium sulfate	cry	−1284.9	−1170.6	91.6	96.5
MgO_4Se	Magnesium selenate	cry	−968.5			
MgS	Magnesium sulfide	cry	−346.0	−341.8	50.3	45.6
Mg_2	Magnesium (Mg_2)	gas	287.7			
Mg_2O_4Si	Magnesium silicate	cry	−2174.0	−2055.1	95.1	118.5
Mn	Manganese	cry	0.0		32.0	26.3
		gas	280.7	238.5	173.7	20.8
MnN_2O_6	Manganese nitrate ($Mn(NO_3)_2$)	cry	−576.3			
$MnNa_2O_4$	Sodium permanganate	cry	−1156.0			
MnO	Manganese oxide (MnO)	cry	−385.2	−362.9	59.7	45.4
MnO_2	Manganese oxide (MnO_2)	cry	−520.0	−465.1	53.1	54.1
MnO_3Si	Manganese metasilicate ($MnSiO_3$)	cry	−1320.9	−1240.5	89.1	86.4
MnS	Manganese sulfide (MnS)	cry	−214.2	−218.4	78.2	50.0
MnSe	Manganese selenide (MnSe)	cry	−106.7	−111.7	90.8	51.0
Mn_2O_3	Manganese oxide (Mn_2O_3)	cry	−959.0	−881.1	110.5	107.7
Mn_2O_4Si	Manganese silicate (Mn_2SiO_4)	cry	−1730.5	−1632.1	163.2	129.9
Mn_3O_4	Manganese oxide (Mn_3O_4)	cry	−1387.8	−1283.2	155.6	139.7
Mo	Molybdenum	cry	0.0		28.7	24.1
		gas	658.1	612.5	182.0	20.8
$MoNa_2O_4$	Sodium molybdate	cry	−1468.1	−1354.3	159.7	141.7
MoO_2	Molybdenum oxide (MoO_2)	cry	−588.9	−533.0	46.3	56.0
MoO_3	Molybdenum oxide (MoO_3)	cry	−745.1	−668.0	77.7	75.0
MoO_4Pb	Lead molybdate ($PbMO_4$)	cry	−1051.9	−951.4	166.1	119.7
MoS_2	Molybdenum sulfide (MoS_2)	cry	−235.1	−225.9	62.6	63.6
N	Nitrogen	gas	472.7	455.5	153.3	20.8
$NNaO_2$	Sodium nitrite	cry	−358.7	−284.6	103.8	
$NNaO_3$	Sodium nitrate	cry	−467.9	−367.0	116.5	92.9
NO_2	Nitrogen dioxide	gas	33.2	51.3	240.1	37.2
NO_2Rb	Rubidium nitrite	cry	−367.4	−306.2	172.0	
NO_3Rb	Rubidium nitrate	cry	−495.1	−395.8	147.3	102.1
NO_3Tl	Thallium nitrate	cry	−243.9	−152.4	160.7	99.5
NP	Phosphorus nitride (PN)	cry	−63.0			
		gas	109.9	87.7	211.2	29.7
N_2	Nitrogen (N_2)	gas	0.0		191.6	29.1
N_2O	Nitrous oxide	gas	82.1	104.2	219.9	38.5
N_2O_3	Nitrogen trioxide	liq	50.3			
		gas	83.7	139.5	312.3	65.6
N_2O_4	Nitrogen tetroxide	liq	−19.5	97.5	209.2	142.7
		gas	9.2	97.9	304.3	77.3
N_2O_4Sr	Strontium nitrite	cry	−762.3			
N_2O_5	Nitrogen pentoxide	cry	−43.1	113.9	178.2	143.1
		gas	11.3	115.1	355.7	84.5
N_2O_6Pb	Lead nitrate ($Pb(NO_3)_2$)	cry	−451.9			
N_2O_6Ra	Radium nitrate	cry	−992.0	−796.1	222.0	
N_2O_6Sr	Strontium nitrate	cry	−978.2	−780.0	194.6	149.9

Molecular formula	Name	State	$\Delta_f H°$ kJ/mol	$\Delta_f G°$ kJ/mol	$S°$ J/mol K
N_2O_6Zn	Zinc nitrate	cry	−483.7		
N_3Na	Sodium azide	cry	21.7	93.8	96.9
N_4Si_3	Silicon nitride (Si_3N_4)	cry	−743.5	−642.6	101.3
Na	Sodium	cry	0.0		51.3
		gas	107.5	77.0	153.7
NaO_2	Sodium superoxide (NaO_2)	cry	−260.2	−218.4	115.9
Na_2	Sodium (Na_2)	gas	142.1	103.9	230.2
Na_2O	Sodium oxide (Na_2O)	cry	−414.2	−375.5	75.1
Na_2O_2	Sodium peroxide (Na_2O_2)	cry	−510.9	−447.7	95.0
Na_2O_3S	Sodium sulfite	cry	−1100.8	−1012.5	145.9
Na_2O_3Si	Sodium metasilicate	cry	−1554.9	−1462.8	113.9
Na_2O_4S	Sodium sulfate	cry	−1387.1	−1270.2	149.6
Na_2S	Sodium sulfide (Na_2S)	cry	−364.8	−349.8	83.7
Nb	Niobium	cry	0.0		36.4
		gas	725.9	681.1	186.3
NbO	Niobium oxide (NbO)	cry	−405.8	−378.6	48.1
NbO_2	Niobium oxide (NbO_2)	cry	−796.2	−740.5	54.5
Nb_2O_5	Niobium oxide (Nb_2O_5)	cry	−1899.5	−1766.0	137.2
Nd	Neodymium	cry	0.0		71.5
		gas	327.6	292.4	189.4
Nd_2O_3	Neodymium oxide	cry	−1807.9	−1720.8	158.6
Ne	Neon	gas	0.0		146.3
Ni	Nickel	cry	0.0		29.9
		gas	429.7	384.5	182.2
NiO_4S	Nickel sulfate ($NiSO_4$)	cry	−872.9	−759.7	92.0
NiS	Nickel sulfide (NiS)	cry	−82.0	−79.5	53.0
Ni_2O_3	Nickel oxide (Ni_2O_3)	cry	−489.5		
No	Nobelium	cry	0.0		
O	Oxygen	gas	249.2	231.7	161.1
OP	Phosphorus oxide (PO)	gas	−28.5	−51.9	222.8
OPb	Lead oxide (PbO) (yellow)	cry	−217.3	−187.9	68.7
	Lead oxide (PbO) (red)	cry	−219.0	−188.9	66.5
OPd	Palladium oxide (PdO)	cry	−85.4		
		gas	348.9	325.9	218.0
ORa	Radium oxide	cry	−523.0		
ORb_2	Rubidium oxide (Rb_2O)	cry	−339.0		
ORh	Rhodium oxide (RhO)	gas	385.0		
OS	Sulfur oxide (SO)	gas	6.3	−19.9	222.0
OSe	Selenium oxide (SeO)	gas	53.4	26.8	234.0
OSi	Silicon oxide (SiO)	gas	−99.6	−126.4	211.6
OSn	Tin oxide (SnO) (tetragonal)	cry	−280.7	−251.9	57.2
		gas	15.1	−8.4	232.1
OSr	Strontium oxide	cry	−592.0	−561.9	54.4
OTi	Titanium oxide (TiO)	cry	−519.7	−495.0	50.0
OTl_2	Thallium oxide (Tl_2O)	cry	−178.7	−147.3	126.0
OU	Uranium oxide (UO)	gas	21.0		
OV	Vanadium oxide (VO)	cry	−431.8	−404.2	38.9
OZn	Zinc oxide	cry	−350.5	−320.5	43.7
O_2	Oxygen (O_2)	gas	0.0		205.2
O_2P	Phosphorous oxide (PO_2)	gas	−279.9	−281.6	252.1
O_2Pb	Lead oxide (PbO_2)	cry	−277.4	−217.3	68.6
O_2Rb	Rubidium superoxide (RbO_2)	cry	−278.7		
O_2Rb_2	Rubidium peroxide (Rb_2O_2)	cry	−472.0		
O_2Ru	Ruthenium oxide (RuO_2)	cry	−305.0		
O_2S	Sulfur dioxide	liq	−320.5		
		gas	−296.8	−300.1	248.2
O_2Se	Selenium dioxide	cry	−225.4		

STANDARD THERMODYNAMIC PROPERTIES OF CHEMICAL SUBSTANCES (continued)

Molecular formula	Name	State	$\Delta_f H°$ kJ/mol	$\Delta_f G°$ kJ/mol	$S°$ J/mol K	C_p J/mol K
O_2Si	Silicon dioxide (α–quartz)	cry	–910.7	–856.3	41.5	44.4
		gas	–322.0			
O_2Sn	Tin oxide (SnO_2) (tetragonal)	cry	–577.6	–515.8	49.0	52.6
O_2Te	Tellurium dioxide	cry	–322.6	–270.3	79.5	
O_2Th	Thorium oxide (ThO_2)	cry	–1226.4	–1169.2	65.2	61.8
O_2Ti	Titanium oxide (TiO_2) (rutile)	cry	–944.0	–888.8	50.6	55.0
O_2U	Uranium oxide (UO_2)	cry	–1085.0	–1031.8	77.0	63.6
		gas	–465.7	–471.5	274.6	51.4
O_2W	Tungsten oxide (WO_2)	cry	–589.7	–533.9	50.5	56.1
O_2Zr	Zirconium oxide (ZrO_2)	cry	–1100.6	–1042.8	50.4	56.2
O_3	Ozone	gas	142.7	163.2	238.9	39.2
O_3PbS	Lead sulfite ($PbSO_3$)	cry	–669.9			
O_3PbSi	Lead metasilicate ($PbSiO_3$)	cry	–1145.7	–1062.1	109.6	90.0
O_3Pr_2	Praseodymium oxide (Pr_2O_3)	cry	–1809.6			117.4
O_3Rh_2	Rhodium oxide (Rh_2O_3)	cry	–343.0			103.8
O_3S	Sulfur trioxide	cry	–454.5	–374.2	70.7	
		liq	–441.0	–373.8	113.8	
		gas	–395.7	–371.1	256.8	50.7
O_3Sc_2	Scandium oxide (Sc_2O_3)	cry	–1908.8	–1819.4	77.0	94.2
O_3SiSr	Strontium metasilicate	cry	–1633.9	–1549.7	96.7	88.5
O_3Sm_2	Samarium oxide (Sm_2O_3)	cry	–1823.0	–1734.6	151.0	114.5
O_3Tb_2	Terbium oxide (Tb_2O_3)	cry	–1865.2			115.9
O_3Ti_2	Titanium oxide (Ti_2O_3)	cry	–1520.9	–1434.2	78.8	97.4
O_3Tm_2	Thullium oxide (Tm_2O_3)	cry	–1888.7	–1794.5	139.7	116.7
O_3U	Uranium oxide (UO_3)	cry	–1223.8	–1145.7	96.1	81.7
O_3V_2	Vanadium oxide (V_2O_3)	cry	–1218.8	–1139.3	98.3	103.2
O_3W	Tungsten oxide (WO_3)	cry	–842.9	–764.0	75.9	73.8
O_3Y_2	Yttrium oxide (Y_2O_3)	cry	–1905.3	–1816.6	99.1	102.5
O_3Yb_2	Ytterbium oxide (Yb_2O_3)	cry	–1814.6	–1726.7	133.1	115.4
O_4Os	Osmium oxide (OsO_4)	cry	–394.1	–304.9	143.9	
		gas	–337.2	–292.8	293.8	74.1
O_4PbS	Lead sulfate ($PbSO_4$)	cry	–920.0	–813.0	148.5	103.2
O_4PbSe	Lead selenate ($PbSeO_4$)	cry	–609.2	–504.9	167.8	
O_4Pb_2Si	Lead silicate (Pb_2SiO_4)	cry	–1363.1	–1252.6	186.6	137.2
O_4Pb_3	Lead oxide (Pb_3O_4)	cry	–718.4	–601.2	211.3	146.9
O_4RaS	Radium sulfate	cry	–1471.1	–1365.6	138.0	
O_4Rb_2S	Rubidium sulfate	cry	–1435.6	–1316.9	197.4	134.1
O_4Ru	Ruthenium oxide (RuO_4)	cry	–239.3	–152.2	146.4	
O_4SSr	Strontium sulfate	cry	–1453.1	–1340.9	117.0	
O_4STl_2	Thallium sulfate (Tl_2SO_4)	cry	–931.8	–830.4	230.5	
O_4SZn	Zinc sulfate	cry	–982.8	–871.5	110.5	99.2
O_4SiSr_2	Strontium silicate	cry	–2304.5	–2191.1	153.1	134.3
O_4SiZn_2	Zinc silicate	cry	–1636.7	–1523.2	131.4	123.3
O_4SiZr	Zirconium silicate ($ZrSiO_4$)	cry	–2033.4	–1919.1	84.1	98.7
O_5Ta_2	Tantalum oxide (Ta_2O_5)	cry	–2046.0	–1911.2	143.1	135.1
O_5Ti_3	Titanium oxide (Ti_3O_5)	cry	–2459.4	–2317.4	129.3	154.8
O_5V_2	Vanadium oxide (V_2O_5)	cry	–1550.6	–1419.5	131.0	127.7
O_5V_3	Vanadium oxide (V_3O_5)	cry	–1933.0	–1803.0	163.0	
O_7Re_2	Rhenium oxide (Re_2O_7)	cry	–1240.1	–1066.0	207.1	166.1
		gas	–1100.0	–994.0	452.0	
O_7U_3	Uranium oxide (U_3O_7)	cry	–3427.1	–3242.9	250.5	215.5
O_8S_2Zr	Zirconium sulfate	cry	–2217.1			172.0
O_8U_3	Uranium oxide (U_3O_8)	cry	–3574.8	–3369.5	282.6	238.4
O_9U_4	Uranium oxide (U_4O_9)	cry	–4510.4	–4275.1	334.1	293.3
Os	Osmium	cry	0.0		32.6	24.7
		gas	791.0	745.0	192.6	20.8
P	Phosphorus (white)	cry	0.0		41.1	23.8

WVMP SAR Reference 3-14

"Estimation of Heat Capacities of Solid Mixed Oxides,"
Leitner, J., P. Chuchvalec, D. Sedmidubský, A. Strejc, and
P. Abrman, Thermochim. Acta, 395, 27-46, 2003.

ELSEVIER

Thermochimica Acta 395 (2003) 27–46

thermochimica acta

www.elsevier.com/locate/tca

Estimation of heat capacities of solid mixed oxides

Jindřich Leitner[a,*], Pavel Chuchvalec[b], David Sedmidubský[c], Aleš Strejc[c], Petr Abrman[b]

[a]*Department of Solid State Engineering, Institute of Chemical Technology, Technická 5, 166 28 Praha 6, Czech Republic*
[b]*Department of Physical Chemistry, Institute of Chemical Technology, Technická 5, 166 28 Praha 6, Czech Republic*
[c]*Department of Inorganic Chemistry, Institute of Chemical Technology, Technická 5, 166 28 Praha 6, Czech Republic*

Received 30 October 2001; received in revised form 11 February 2002; accepted 11 March 2002

Abstract

Some empirical methods for the estimation of standard molar heat capacity (C°_{pm}) of solid mixed oxides are reviewed and the reliability of the obtained data in phase equilibria calculations is examined. Following the comparison of predicted values of C°_{pm}(298.15 K) with more than 300 experimental data the most widely used Neumann–Kopp rule (NKR) is found to be very universal but in some cases the mean deviation of 3.3% is too high, giving rise to a relatively large error in equilibrium calculation results. On the other hand, the method based on binary oxide contributions proposed by Berman and Brown [Contrib. Mineral. Petrol. 89 (1985) 168] for the estimation of temperature dependencies $C^{\circ}_{pm}(T)$ of silicates and other minerals formed by Al_2O_3, CaO, FeO, Fe_2O_3, K_2O, MgO, Na_2O, SiO_2 and TiO_2 is less general, but more accurate. In comparison with the NKR, the most pronounced drawback of this method is the necessity to know the experimental values of C°_{pm} for a set of mixed oxides, so that the individual contributions of constituent binary oxides can be evaluated.

Keywords: Mixed oxides; Heat capacity; Estimation; Neumann–Kopp rule; Group contribution methods

1. Introduction

The oxide based materials are presently used in a large number of applications. Let us mention only some of the most important ones in the following outline:

- Glasses (system SiO_2–Al_2O_3–B_2O_3–MgO–CaO–PbO–Na_2O–K_2O, special glasses for optical applications, optical fibers).
- Structural ceramics (system SiO_2–Al_2O_3–MgO, zirconia ceramics, sialon).
- Composite materials (oxides are used as a reinforcement in a metallic matrix or, alternatively, as a matrix toughened by non-oxidic fibres).
- Coatings and thin films (protective coatings for gas-turbine parts—system ZrO_2–Y_2O_3–CaO–MgO, dielectric layers in electronics—SiO_2, chemical sensor active layers—ZnO, SnO_2, Fe_2O_3, etc.).
- Materials for magnetic recording (Fe_2O_3, CrO_2, mixed ferrites $(Zn,Mn,Cu)Fe_2O_4$).
- Structural elements of oxide fuel cells ($(La,Ca)CrO_3$, $(La,Sr)MnO_3$, Y_2O_3–ZrO_2).
- High-temperature superconductors (YBaCuO, BiSrCaCuO, HgBaCaCuO, TlBaCaCuO).

Chemical thermodynamics is frequently used in systematic investigation of processes related with

* Corresponding author. Fax: +420-2-2431-0337.
E-mail address: jindrich.leitner@vscht.cz (J. Leitner).

0040-6031/02/$ – see front matter
PII: S0040-6031(02)00177-6

material synthesis and processing as the powerful tool to understand the interrelationship between chemical composition, structure and properties. The calculations of thermodynamic equilibria require knowledge of input thermodynamic data for each substance involved, namely the values of enthalpies of formation and entropies at 298.15 K, as well as the coefficients of temperature dependencies of isobaric molar heat capacities. Alternatively, the parameters of temperature dependence of molar Gibbs energy can be directly employed. For a number of solid oxides, such data are tabulated for a wide range of temperatures, see, e.g. [2–9] or available in a form of computer databases. In addition, comprehensive data files for silicates and other oxidic minerals are disposable, e.g. [1,10–16].

The molar heat capacity (C°_{pm}) is one of the fundamental thermodynamic functions of solid substances. Various calorimetric methods being presently applicable from very low temperatures (approx. 10^{-1} K) up to melting points are used for experimental determination of C°_{pm}. The calorimetric measurements have been taken for practically all binary oxides and a considerable number of mixed oxides. The obtained data are available in literature. However, in many cases the experimental data are still missing. Hence, a lot of empirical methods for estimation of C°_{pm} of inorganic compounds have been proposed in order to overcome this lack. These methods are described in some review papers [7,17,18].

The aim of this paper is to summarize the as yet proposed methods for estimation of molar heat capacities of solid mixed oxides,[1] to verify their credibility and to examine the reliability of estimated values in equilibrium calculations in oxide systems. The paper follows the previous study [19] focused to prediction of C°_{pm} for binary oxides.

2. Method description

Let us consider the formation of a ternary oxide $A_{2a}B_{3b}O_x$ from binary oxides A_aO_m and B_bO_n ($x = 2m + 3n$) according to the following equation:

$$2A_aO_m(s) + 3B_bO_n(s) \rightarrow A_{2a}B_{3b}O_x(s) \quad \text{(R1)}$$

The change of isobaric heat capacity accompanying the reaction, $\Delta C^\circ_{pm}(ox)$, can be expressed as:

$$\Delta C^\circ_{pm}(ox) = C^\circ_{pm}(A_{2a}B_{3b}O_x) - 2C^\circ_{pm}(A_aO_m) - 3C^\circ_{pm}(B_bO_n) \quad (1)$$

The values of $\Delta C^\circ_{pm}(ox)$ for more than 300 mixed oxides evaluated from the experimental (calorimetric) data of C°_{pm} using Eq. (1) are plotted in Fig. 1. The dispersion of the obtained values falls roughly in the interval of ± 30 J K^{-1} mol^{-1} and their average is close to zero. All below-mentioned methods can be classified into two essential groups according to whether the condition $\Delta C^\circ_{pm}(ox) = 0$ is fulfilled or not.

2.1. $\Delta C^\circ_{pm}(ox) = 0$

2.1.1. Neumann–Kopp rule

The Neumann–Kopp rule (NKR) represents presumably the simplest approach for estimation of $C^\circ_{pm}(298.15)$ as well as for temperature dependence $C^\circ_{pm}(T)$. Based on this method, the molar heat capacity of a mixed oxide is calculated as a weighted sum of heat capacities of the constituent binary oxides. For example, the heat capacity of the above-mentioned ternary oxide with the stoichiometry $A_{2a}B_{3b}O_x$ reads

$$C^\circ_{pm}(A_{2a}B_{3b}O_x) = 2C^\circ_{pm}(A_aO_m) + 3C^\circ_{pm}(B_bO_n) \quad (2)$$

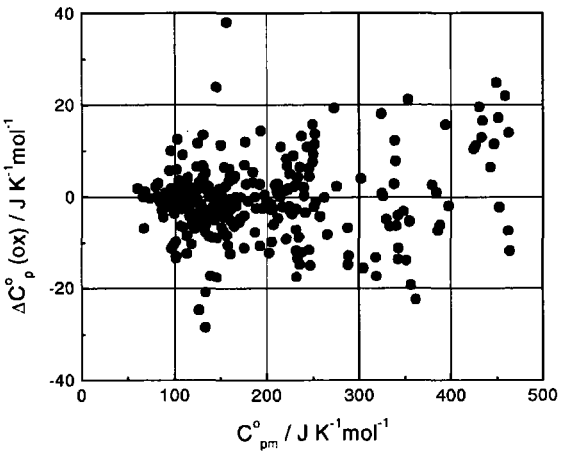

Fig. 1. Heat capacity change, $\Delta C^\circ_{pm}(ox)$, accompanying the formation of mixed oxides from constituent binary oxides at the temperature of 298.15 K.

[1] The term "mixed oxides" stands here for ternary or higher compounds of oxygen (as an anion O^{2-}) with two or more cations, as well as for compounds consisting of complex anions, which can be considered as salts of oxidic acids (chromates, wolframates) including those cases when the anions form chains, sheets of three-dimensional networks (e.g. silicates).

Such an approximation results in the case of silicates and other natural minerals in the average estimation error of approx. 5% [20]. The main advantage of the NKR lies in the availability of experimental temperature dependencies of $C^{\circ}_{pm}(T)$ for the respective binary oxides.

As an improvement of basic the NKR let us mention the procedure proposed by Helgeson et al. [20] for the estimation of C°_{pm} of silicates and other oxide minerals. This method is based upon the assumption of zero change of heat capacity in the course of an exchange reaction

$$A_aB_bO_x(s) + C_cO_y(s) = B_bO_z(s) + A_aC_cO_{x+y-z} \quad (R2)$$

between structurally similar substances. The unknown data for a ternary oxide $A_aC_cO_{x+y-z}$ can be thus obtained directly from the data of binary oxides B_bO_z, C_cO_y, and a mixed oxide $A_aB_bO_x$. The accuracy of estimation may be increased to about 2% in this manner.

However, the substantial drawback of this method inheres in the dependence, in many cases very important, on the choice of the given exchange reaction (R2).

A method analogous to that of Helgeson has been proposed by Ukleba et al. [21] for the estimation of $C^{\circ}_{pm}(298.15)$, in which the exchange reaction between two ternary oxides is considered. The mean estimation error for the set of 124 selected ternary oxides amounts to approx. 3%. In case of more possible exchange reactions, averaging of the relevant values is recommended [21].

2.2. $\Delta C^{\circ}_{pm}(ox) \neq 0$

2.2.1. Contribution methods—atomic and ionic contributions

For the estimation of molar heat capacities of mixed oxides, several contribution methods can be used, which have been reviewed in the previous paper [19] dealing with binary oxides. In cases when the contributions of individual cations (atoms) and the anion O^{2-} (atom O) are considered, the obtained value corresponds to $\Delta C^{\circ}_{pm}(ox) = 0$ (for the calculation of $\Delta C^{\circ}_{pm}(ox)$ according to Eq. (1), the estimated (not experimental) values of C°_{pm} of constituent binary oxides must be used).

Based on the method proposed by Kellogg [22] and later extended by Kubaschewski and Ünal [23], the particular contributions to $C^{\circ}_{pm}(298.15\,K)$ were evaluated for 25 different complex anions constituted from oxygen and another element (Al, B, Cr, Fe, Ge, Hf, Mo, Nb, Se, Si, Ti, U, V, W, and Zr) [18]. As the complex anion contributions differ from the sum of contributions of respective cations and the anion O^{2-}, the resulting value $\Delta C^{\circ}_{pm}(ox) = 0$ in such a case. The evaluated contributions are listed in Tables 1 and 2.

Kubaschewski and Ünal [23] have further proposed the method for estimation of parameters A, B, and C in a simple temperature dependence of $C^{\circ}_{pm}(T)$ in the form

$$C^{\circ}_{pm} = A + BT + \frac{C}{T^2} \quad (3)$$

The parameters A and B are estimated using the relations

$$A = \frac{10^{-3}T_m[C^{\circ}_{pm}(298.15\,K) + 4.7n] - 1.25n \times 10^5(T_m)^{-2} - 9.05n}{10^{-3}T_m - 0.298} \quad (4)$$

$$B = \frac{25.6n + 4.2n \times 10^5(T_m)^{-2} - C^{\circ}_{pm}(298.15\,K)}{10^{-3}T_m - 0.298} \quad (5)$$

where n is the number of ions (contributions) in the formula unit. The generalized value of the third parameter was set to $C = -4.2n$. The described approach can be employed only for substances whose melting temperature T_m is lower than approx. 2300 K.

The ionic contributions of complex anions consisting of oxygen and other elements (Al, B, Cr, Fe, Ge, Mn, Mo, Nb, Re, Se, Si, Ta, Tc, Ti, U, V, W, and Zr), as well as the contributions of individual cations (in this case differing for unlike valencies) were also evaluated by Kumok [24].

2.2.2. Contribution methods—structural and simple oxides contributions

A number of contribution methods has been developed directly for mixed oxides. The values of $C^{\circ}_{pm}(298.15\,K)$ or the parameters of $C^{\circ}_{pm}(T)$ dependence are additively calculated from contributions of constituent oxides or from structural contributions.

Table 1
Cationic contributions to heat capacity at 298.15 K

Cation	Contributions to $C^{\circ}_{pm}(298)$ (J K^{-1} mol^{-1})		Cation	Contributions to $C^{\circ}_{pm}(298)$ (J K^{-1} mol^{-1})		Cation	Contributions to $C^{\circ}_{pm}(298)$ (J K^{-1} mol^{-1})	
	[18,23]	[17,24]		[18,23]	[17,24]		[18,23]	[17,24]
Ag^{2+}	25.73	28.60	Ho^{2+}	23.01	26.10	Se^{6+}	21.34	
Al^{3+}	19.66	17.60	Ho^{3+}	23.01	29.60	Si^{4+}		12.10
As^{3+}	25.10	26.70	In^{+}	24.27	23.70	Sm^{2+}	25.10	35.70
As^{5+}	25.10		In^{2+}	24.27	26.50	Sm^{3+}	25.10	34.40
B^{3+}		6.10	In^{3+}	24.27	25.70	Sn^{2+}	23.43	27.80
Ba^{2+}	26.36	28.40	Ir^{3+}	23.85		Sn^{4+}	23.43	25.80
Be^{2+}	9.62	12.60	Ir^{4+}	23.85		Sr^{2+}	25.52	29.30
Bi^{3+}	26.78	29.00	K^{+}	25.94	28.00	Ta^{3+}	23.01	27.70
Ca^{2+}	24.69	27.30	La^{2+}	25.52	29.50	Ta^{4+}	23.01	
Cd^{2+}	23.01	28.00	La^{3+}	25.52	29.30	Ta^{5+}	23.01	26.30
Ce^{2+}	23.43	27.60	Li^{+}	19.66	20.70	Tb^{2+}		24.30
Ce^{3+}	23.43	31.40	Lu^{3+}		28.70	Tb^{3+}		33.00
Ce^{4+}	23.43	28.20	Mg^{2+}	19.66	22.20	Tc^{4+}		30.50
Co^{2+}	28.03	31.30	Mn^{2+}	23.43	27.90	Th^{2+}	25.52	26.10
Co^{3+}	28.03	12.40	Mn^{3+}	23.43	25.00	Th^{3+}	25.52	29.70
Cr^{2+}	23.01	21.00	Mn^{4+}	23.43	21.20	Th^{4+}	25.52	28.20
Cr^{3+}	23.01	29.10	Mo^{2+}		23.60	Ti^{2+}	21.76	21.30
Cr^{4+}	23.01	21.80	Mo^{4+}		21.40	Ti^{3+}	21.76	23.30
Cr^{6+}	23.01		Na^{+}	25.94	26.80	Ti^{4+}	21.76	25.50
Cs^{+}	26.36	31.10	Nb^{3+}	23.01	23.00	Ti^{5+}	21.76	
Cu^{+}	25.10	25.50	Nb^{4+}	23.01	23.50	Tl^{+}	27.61	30.90
Cu^{2+}	25.10	25.00	Nb^{5+}	23.01	26.70	Tl^{3+}	27.61	
Dy^{2+}		84.00	Nd^{3+}	24.27	28.30	Tm^{3+}		33.30
Dy^{3+}		31.00	Ni^{2+}	27.61	26.70	U^{2+}		30.00
Er^{3+}		29.10	P^{5+}	14.23		U^{3+}	26.78	34.10
Eu^{2+}		29.10	Pb^{2+}	26.78	29.30	U^{4+}	26.78	30.80
Eu^{3+}		33.30	Pb^{4+}	26.78	47.30	U^{5+}	26.78	33.80
Fe^{2+}	25.94	28.70	Pd^{2+}		20.60	U^{6+}	26.78	34.20
Fe^{3+}	25.94	26.20	Pm^{3+}		31.40	V^{2+}	22.18	21.60
Fr^{+}		29.50	Pr^{3+}	24.27	31.50	V^{3+}	22.18	27.10
Ga^{+}	20.92	23.90	Pr^{4+}	24.27		V^{4+}	22.18	26.90
Ga^{2+}	20.92	22.75	Pt^{4+}		24.20	V^{5+}	22.18	
Ga^{3+}	20.92	21.60	Pu^{2+}		40.70	W^{4+}		21.60
Gd^{3+}	23.43	27.80	Pu^{3+}		28.40	Y^{2+}	25.10	22.50
Ge^{2+}	20.08	25.80	Pu^{4+}		35.10	Y^{3+}	25.10	24.00
Ge^{4+}	20.08	23.00	Ra^{2+}		29.60	Yb^{2+}		29.00
Hf^{2+}	25.52		Rb^{+}	26.36	30.80	Yb^{3+}		32.60
Hf^{3+}	25.52		Sb^{3+}	23.85	30.30	Zn^{2+}	21.76	25.50
Hf^{4+}	25.52	20.20	Sc^{3+}		21.20	Zr^{2+}	23.85	24.70
Hg^{+}	25.10	26.30	Se^{4+}	21.34		Zr^{3+}	23.85	25.00
Hg^{2+}	25.10	27.70	Se^{5+}	21.34		Zr^{4+}	23.85	22.90

These methods are confined to a certain family of mixed oxides, though.

Several different methods have been brought in for the estimation of $C^{\circ}_{pm}(T)$ of silicates and other oxide materials. Robinson and Haas [25] suggested a model based on structural contributions corresponding to individual cations in particular coordination (number of the nearest neighbors O^{2-}). The parameters of the temperature function

$$C^{\circ}_{pm} = a + bT + \frac{c}{T^2} + fT^2 + \frac{g}{T^{1/2}} \quad (6)$$

Table 2
Anionic contributions to heat capacity at 298.15 K

Anion	Contributions to $C^\circ_{pm}(298)$ ($J\,K^{-1}\,mol^{-1}$)		Anion	Contributions to $C^\circ_{pm}(298)$ ($J\,K^{-1}\,mol^{-1}$)	
	[18,23]	[17,24]		[18,23]	[17,24]
$(AlO_2)^-$	49.26	47.40	$(SeO_3)^{2-}$	73.32	72.50
$(AlO_3)^{3-}$	67.73		$(SeO_4)^{2-}$		86.60
$(BO_2)^-$	41.19	40.30	$(SiO_3)^{2-}$	62.93	59.30
$(BO_3)^{3-}$	55.60	52.00	$(SiO_4)^{4-}$	78.34	73.50
$(B_4O_7)^{2-}$	134.26		$(Si_2O_5)^{2-}$	106.79	103.80
$(CrO_2)^-$	62.67	52.40	$(TaO_3)^-$		79.80
$(CrO_3)^{3-}$		84.90	$(TcO_4)^-$		95.30
$(CrO_4)^{2-}$	92.27	86.40	$(TiO_3)^{2-}$	74.45	71.90
$(Cr_2O_7)^{2-}$		166.50	$(TiO_4)^{4-}$	92.52	85.90
$(FeO_2)^-$	63.03	59.70	$(Ti_2O_5)^{2-}$	124.69	120.80
$(GeO_3)^{2-}$	72.08	68.20	$(UO_3)^-$		82.10
$(HfO_3)^{2-}$	78.47		$(UO_4)^{2-}$	107.11	97.90
$(MnO_4)^-$		91.10	$(U_2O_7)^{2-}$		171.40
$(MnO_4)^{2-}$		86.80	$(VO_3)^-$	71.54	70.90
$(MnO_4)^{3-}$		97.50	$(VO_4)^{3-}$	89.20	87.74
$(MoO_4)^{2-}$	92.77	89.80	$(V_2O_7)^{4-}$	163.50	158.90
$(Mo_2O_7)^{2-}$		163.60	$(WO_4)^{2-}$	97.49	89.70
$(NbO_3)^-$	78.00	74.90	$(W_2O_7)^{2-}$		161.30
$(ReO_4)^-$		96.40	$(ZrO_3)^{2-}$	75.06	73.40

are calculated additively from such structural contributions. A set of 20 different contributions has been assessed from the available experimental data for 61 minerals. The original experimental values have been reproduced with an accuracy higher than 2%.

For the estimation of the temperature dependence $C^\circ_{pm}(T)$ of minerals formed from binary oxides Al_2O_3, CaO, FeO, Fe_2O_3, K_2O, MgO, Na_2O, SiO_2 and TiO_2 in the form

$$C^\circ_{pm} = k_0 + \frac{k_1}{T^{1/2}} + \frac{k_2}{T^2} + \frac{k_3}{T^3} \quad (7)$$

Berman and Brown [1] evaluated the contributions of the binary oxides to parameters k_0, k_1, k_2, and k_3. They employed the calorimetric data for 101 minerals for the least square fitting of contributions. The estimation error did not exceed 2% for a large majority of substances even in this case. The calculated values of contributions at 298.15 K for the above-mentioned oxides along with the respective experimental data $C^\circ_{pm}(298.15\ K)$ and the relative differences are given in Table 3. These differences are substantial only for FeO and K_2O. Consequently, for the mixed oxides

Table 3
Contributions of binary oxides to heat capacity at 298.15 K [1]

Oxide	Contributions to $C^\circ_{pm}(298)$ ($J\,K^{-1}\,mol^{-1}$)	$C^\circ_{pm}(298)$ ($J\,K^{-1}\,mol^{-1}$) of binary oxide	Difference (%)
Al_2O_3	77.41	79.01	−2.03
CaO	43.18	42.42	1.80
Fe_2O_3	105.17	104.77	0.39
FeO	43.38	48.04	−9.69
K_2O	71.70	84.53	−15.17
MgO	37.31	37.26	0.15
Na_2O	69.18	68.56	0.91
SiO_2	43.95	44.42	−1.05
TiO_2	55.44	55.10	0.61

formed by Al_2O_3, CaO, Fe_2O_3, MgO, Na_2O, SiO_2 and TiO_2, the values predicted by the Berman–Brown method will be very close to those ones obtained from the NKR.

Another significant family of mixed oxides is represented by high-temperature superconductors and related phases. The contributions to the estimation of parameters k_0, k_1, and k_2 to the temperature dependence of $C^\circ_{pm}(T)$ according to Eq. (7) have been proposed by Voronin and Uspenskaya [26] for mixed oxides in the system Y–Ba–Cu–O. Analyzing the experimental data for five mixed oxides, they evaluated the contributions for binary oxides Y_2O_3, BaO, CuO, and Cu_2O and predicted the parameters of Eq. (7) for another seven ternary and quaternary oxides.

2.2.3. *Empirical rules in homological series and groups of chemically related substances (oxides)*

Goncharov and Vorobev [27] developed the method for estimation of temperature dependency $C^\circ_{pm}(T)$ for garnets of Fe, Al and Ga with rare earth (RE) elements starting from an assumption of $\Delta C^\circ_{pm}(ox)$ being equal for the same family of substances (e.g. $RE_3Fe_5O_{12}$, $RE_3Al_5O_{12}$, $RE_3Ga_5O_{12}$) irrespective of the particular RE element. Such assumption was found to be well satisfied with the experimental data for ferrogarnets of Y, Sm, Eu, Gd, Tb, and Lu yielding the error did not exceed 2%. Accordingly, the generalized temperature dependence of $\Delta C^\circ_{pm}(ox)$ for $RE_3Al_5O_{12}$ and $RE_3Ga_5O_{12}$ has been obtained from data for $Y_3Al_5O_{12}$ [28] and $Gd_3Ga_5O_{12}$ [29], respectively.

The prediction method of $C^\circ_{pm}(298.15\ K)$ using ionic contributions brought in by Aldabergenov et al. [30,31]

was based on the idea that in homological series like $A_m(B_xO_y)_n$, the molar heat capacity is a linear function of coefficient n specifying the number of complex anions $(B_xO_y)^{z-}$ in the formula unit. Thus for alkaline aluminates, the series

$$AlO_2^- \overset{+AlO_2^-}{\rightarrow} Al_2O_4^{2-} \overset{+AlO_2^-}{\rightarrow} Al_3O_6^{3-} \cdots$$

is considered, in which each higher anion differs from the previous one in an increment $(AlO_2)^-$. The higher anion contributions are considered as n-multiples of the primary anion $(AlO_2)^-$, whose value is determined from the available experimental data of $C^\circ_{pm}(298.15\ K)$ for $KAlO_2$, $LiAlO_2$ and $NaAlO_2$ as well as from the ionic contributions for the respective cations K^+, $Li^+$and Na^+ obtained from their standard molar entropies in an infinitely diluted solution.

3. Comparison of selected methods

In the following part three selected methods, namely the NKR, the Kellogg's method of ionic contributions [22] with ionic contributions taken from Spencer [18] (KK), and the binary oxide contribution method by Berman and Brown [1] (BB) are compared. The values of $C^\circ_{pm}(298.15\ K)$ for binary oxides used in the NKR are listed in Table 4. The methods are examined both in terms of their universality, i.e. according to the number of mixed oxides whose

Table 4
Selected values of heat capacity of solid binary oxides at 298.15 K [19]

Oxide	Phase	$C^\circ_{pm}(298)$ ($J\ K^{-1}\ mol^{-1}$)	Oxide	Phase	$C^\circ_{pm}(298)$ ($J\ K^{-1}\ mol^{-1}$)
Ag_2O	Sol	66.32	MgO	Sol	37.26
Al_2O_3	Sol	79.01	Mn_2O_3	Sol	99.04
B_2O_3	Sol	62.98	MnO	Sol	44.76
BaO	Sol	47.06	MnO_2	Sol	54.42
BeO	Sol-A	24.98	MoO_2	Sol	55.99
Bi_2O_3	Sol-A	112.13	MoO_3	Sol	75.14
CaO	Sol	42.42	Na_2O	Sol-A	68.56
CdO	Sol	44.16	Nb_2O_5	Sol	132.13
Ce_2O_3	Sol	117.05	Nd_2O_3	Sol-A	111.34
CeO_2	Sol	61.53	NiO	Sol-A	44.29
CoO	Sol	55.22	PbO	Red	45.74
Cr_2O_3	Sol	114.26	Pr_2O_3	Sol	116.63
CrO_3	Sol	79.12	Rh_2O_3	Sol	89.12
Cs_2O	Sol	75.90	Sc_2O_3	Sol	93.94
Cu_2O	Sol	62.47	SiO_2	Quartz(L)	44.42
CuO	Sol	42.26	Sm_2O_3	Sol-A	115.82
Dy_2O_3	Sol-A	116.26	SrO	Sol	45.15
Er_2O_3	Sol	108.49	Ta_2O_5	Sol	131.48
Eu_2O_3	Cubic	124.68	TeO_2	Sol	63.88
Fe_2O_3	Sol-A	104.77	TeO_3	Sol	71.47
FeO	Sol	48.04	TiO_2	Rutile	55.10
Ga_2O_3	Sol	93.86	Tl_2O_3	Sol	105.46
Gd_2O_3	Cubic	105.51	Tm_2O_3	Sol-A	116.72
GeO_2	Hexagonal	51.95	UO_2	Sol	63.59
HfO_2	Sol-A	60.26	UO_3	Sol	81.19
HgO	Sol	43.89	V_2O_5	Sol	127.37
Ho_2O_3	Sol	114.96	WO_3	Sol-A	72.80
K_2O	Sol	84.53	Y_2O_3	Sol-A	102.51
La_2O_3	Sol	108.78	Yb_2O_3	Sol-A	115.36
Li_2O	Sol	54.25	ZnO	Sol	41.07
Lu_2O_3	Sol	101.76	ZrO_2	Sol-A	56.21

C°_{pm}(298.15 K) and/or $C^{\circ}_{pm}(T)$ can be obtained, and concerning credibility of the predicted values as well.

3.1. C°_{pm}(298.15 K) experimental data set

The predicted values of C°_{pm}(298.15 K) were compared with available experimental data in order to qualitatively compare the selected estimation methods. 326 mixed oxide phases formed by 71 binary oxides of 57 elements were included into the data set given in Table 5. The values of C°_{pm}(298.15 K) were taken from more than 100 literature sources—data collections, review articles and original papers. The presented data come in all cases either from direct (calorimetric) experiments or from simultaneous processing (optimization) of more experimental data. The accuracy of the calorimetric data depends on the particular method used. The most precise values were obtained by direct measurements of C°_{pm} in adiabatic calorimeters (the determination error does not exceed 0.2–0.5% at an ambient temperature). The experimental error of C°_{pm}(298.15 K) measured in DSC calorimeters (in continuous or stepwise mode) is higher, about 1–2%. Even the higher error (2–3%) must be taken into account in case of heat content measurements, $H_T - H_{Tref}$, using drop calorimeters. The direct result here is the temperature dependence of the integral function, relative enthalpy, usually measured above 450 °C. The $C^{\circ}_{pm}(T)$ dependence is then obtained by differentiating it with respect to temperature and C°_{pm}(298.15 K) by extrapolation.

In some cases, the available experimental data were not taken into account for assessment of the reliability of the estimation methods. For instance, the values of $C^{\circ}_{pm}(T)$ above 400 K and extrapolated C°_{pm}(298.15 K) reported by Gospodinov et al. for ternary oxides formed by TeO_2 and MnO [32], MgO [33], Al_2O_3, Ga_2O_3, In_2O_3 and Tl_2O_3 [34], or CuO [35] are not treated as much reliable. Indeed, their data of C°_{pm}(298.15 K) for ternary oxides $BaZrO_3$, $CaZrO_3$ and $SrZrO_3$ [36], measured on the same calorimeter and evaluated using the same procedure, are obviously quite different from values reported by other authors [37], and, moreover, some errors have been found in the evaluation of experimental results [38]. Similarly, the data for ternary oxides of Sb_2O_5, BaO, CaO and SrO [39], CoO, NiO and ZnO [40], all reported by Kasenov et al., as well as for quaternary oxides of type $RE_2AE_2Mn_4O_{11}$, (RE: Gd, AE: Ba) [41], (RE: Dy, AE: Sr) [42], (RE: Er, Gd, Ho, La, Lu, Nd, AE: Sr) [43], (RE: La, AE: Ca) [44], and (RE: Er, Gd, Nd, AE: Ca) [45] were not included in the experimental data set. In all latter studies, the conventional calorimeter ICT-400 has been employed for C°_{pm} measurements providing the results with the relatively large error of about 10%. For example, the average value of $181 \pm 17\ J\ K^{-1}\ mol^{-1}$ resulting from five measurements of $NiSb_2O_6$ is referred in [40], which exceeds severalfold the errors of other data and would therefore, depreciate the comparison of experimental and estimated values.

In addition to complex mixed oxides, the oxides of Me_3O_4 type with a cation of one element in two valence states, $Me^{2+}$and Me^{3+}(Me: Co, Cr, Fe, Mn, Pb), have been also included in the experimental data set. For the sake of completeness, even those mixed oxides are listed in the Table 5, which C°_{pm} cannot be predicted by any of the tested methods.

3.2. Neumann–Kopp rule (NKR)

The NKR is the most universal from all considered methods—within the given experimental data set the total number of 295 values of C°_{pm}(298.15 K) can be estimated using this rule. The NKR cannot be applied only in the following cases:

- The experimental values of C°_{pm}(298.15 K) for binary oxides forming a particular mixed oxide are not available. So far the experimental data for Co_2O_3, CrO_2, MnO_3, Rb_2O, RuO_3 and Tb_2O_3 are missing, and thus only their estimated values are reported in thermodynamic tables. Since the mean prediction error of contribution methods for binary oxides varies by 5% (for C°_{pm}(298.15 K)) [19], the application of the estimated data could significantly decrease the quality of NKR results.
- A given mixed oxide cannot be obtained from a chemical reaction of bare solid binary oxides. Let us mention a quaternary oxide $YBa_2Cu_3O_7$ as the example, which formation can be described as

$$\tfrac{1}{2}Y_2O_3 + 2\,BaO + 3\,CuO + \tfrac{1}{4}O_2 \rightarrow YBa_2Cu_3O_7 \quad (R3)$$

Here the gaseous oxygen occurs as one of the starting compounds. The NKR is based on a simple

Table 5
Comparison of experimental and estimated values of heat capacity at 298.15 K of solid mixed oxides

No.	Mixed oxide	Binary oxides combination	Phase	Reference	$C^{\circ}_{pm}(298)$ ($J\,K^{-1}\,mol^{-1}$)	$C^{\circ}_{pm}(298)$(NKR) ($J\,K^{-1}\,mol^{-1}$)	ΔC°_{pm} (%)	$C^{\circ}_{pm}(298)$(KK) ($J\,K^{-1}\,mol^{-1}$)	ΔC°_{pm} (%)	$C^{\circ}_{pm}(298)$(BB) ($J\,K^{-1}\,mol^{-1}$)	ΔC°_{pm} (%)
1	Ag_2WO_4	$Ag_2O{\cdot}WO_3$	Sol	[47]	150.36	139.12	−7.48	148.95	−0.94		
2	$Al_{18}B_4O_{33}$	$9Al_2O_3{\cdot}2B_2O_3$	Sol	[6]	823.19	837.05	1.68				
3	Al_2SiO_5	$Al_2O_3{\cdot}SiO_2$	Andalusite	[1]	123.40	123.47	0.06			121.36	−1.65
4	Al_2SiO_5	$Al_2O_3{\cdot}SiO_2$	Kyanite	[1]	122.19	123.47	1.05			121.36	−0.68
5	Al_2SiO_5	$Al_2O_3{\cdot}SiO_2$	Sillimanite	[1]	122.93	123.47	0.44			121.36	−1.28
6	Al_2TiO_5	$Al_2O_3{\cdot}TiO_2$	Sol	[6]	136.40	134.11	−1.68			132.85	−2.60
7	$Al_4B_2O_9$	$2Al_2O_3{\cdot}B_2O_3$	Sol	[6]	222.64	221.00	−0.74				
8	$Al_6Si_2O_{13}$	$3Al_2O_3{\cdot}2SiO_2$	Sol	[1]	325.99	325.87	−0.04			320.13	−1.80
9	$Ba_2Si_3O_8$	$2BaO{\cdot}3SiO_2$	Sol	[8]	224.60	227.38	1.24	222.44	−0.96		
10	Ba_2TiO_4	$2BaO{\cdot}TiO_2$	Sol	[6]	149.15	149.22	0.05	145.24	−2.62		
11	$Ba_3B_2O_6$	$3BaO{\cdot}B_2O_3$	Sol	[48]	215.01	204.16	−5.05	190.28	−11.50		
12	$Ba_3LaNb_3O_{12}$	$(6BaO{\cdot}La_2O_3{\cdot}3Nb_2O_5)/2$	Sol	[49]	387.61	393.77	1.59				
13	$BaAl_2O_4$	$BaO{\cdot}Al_2O_3$	Sol	[6]	113.70	126.07	10.88	112.28	−1.25		
14	$BaAl_2Si_2O_8$	$BaO{\cdot}Al_2O_3{\cdot}2SiO_2$	Sol	[50]	221.71	214.91	−3.07	222.36	0.29		
15	$BaCeO_3$	$BaO{\cdot}CeO_2$	Sol	[51]	111.91	108.59	−2.97				
16	$BaCuO_2$	$BaO{\cdot}CuO$	Sol	[52]	95.00	89.32	−5.98				
17	$BaCuO_{2.09}$		Sol	[53]	96.89						
18	$BaMoO_4$	$BaO{\cdot}MoO_3$	Sol	[54]	122.00	122.20	0.16	119.13	−2.35		
19	$BaSiO_3$	$BaO{\cdot}SiO_2$	Sol	[6]	89.02	91.48	2.77	89.29	0.31		
20	$BaSrFe_4O_8$	$BaO{\cdot}SrO{\cdot}2Fe_2O_3$	Sol	[55]	288.90	301.75	4.45	304.00	5.23		
21	$BaTiO_3$	$BaO{\cdot}TiO_2$	Sol	[6]	102.45	102.16	−0.29	100.81	−1.60		
22	$BaUO_4$	$BaO{\cdot}UO_3$	Sol	[8]	133.50	128.25	−3.93	133.47	−0.02		
23	$BaZrO_3$	$BaO{\cdot}ZrO_2$	Sol	[37]	101.71	103.27	1.53	101.42	−0.29		
24	Be_2SiO_4	$2BeO{\cdot}SiO_2$	Sol	[6]	93.48	94.38	0.96	87.96	−5.90		
25	$Be_3B_2O_6$	$3BeO{\cdot}B_2O_3$	Sol	[6]	138.44	137.92	−0.37	140.06	1.17		
26	$BeAl_2O_4$	$BeO{\cdot}Al_2O_3$	Sol	[6]	104.94	103.99	−0.91	108.14	3.05		
27	$BeAl_6O_{10}$	$BeO{\cdot}3Al_2O_3$	Sol	[6]	261.92	262.01	0.03				
28	$BeWO_4$	$BeO{\cdot}WO_3$	Sol	[8]	96.92	97.78	0.89	107.11	10.52		
29	$Bi_2Ca_2O_5$	$Bi_2O_3{\cdot}2CaO$	Sol	[56]	197.44	196.97	−0.24				
30	Bi_2CaO_4	$Bi_2O_3{\cdot}CaO$	Sol	[56]	151.32	154.55	2.13				
31	Bi_2CuO_4	$Bi_2O_3{\cdot}CuO$	Sol	[57]	151.73	154.39	1.75				
32	$Bi_2Sr_2CuO_6$	$Bi_2O_3{\cdot}2SrO{\cdot}CuO$	Sol	[58]	241.30	244.69	1.40				
33	$Bi_2Sr_2Ca_{1.2}Cu_{1.8}O_{8.5}$		Sol	[59]	346.70						
34	$Bi_2Sr_3Cu_2O_8$	$Bi_2O_3{\cdot}3SrO{\cdot}2CuO$	Sol	[58]	353.28	332.10	−6.00				
35	$Bi_6Ca_4O_{13}$	$3Bi_2O_3{\cdot}4CaO$	Sol	[56]	504.06	506.07	0.40				
36	$Ca_{12}Al_{14}O_{33}$	$12CaO{\cdot}7Al_2O_3$	Sol	[8]	1084.82	1062.11	−2.09			1060.03	−2.29
37	$Ca_2Al_2SiO_7$	$2CaO{\cdot}Al_2O_3{\cdot}SiO_2$	Sol	[1]	205.51	208.27	1.34	210.83	2.59	207.72	1.08

Table 5 (*Continued*)

No.	Mixed oxide	Binary oxides combination	Phase	Reference	$C^{\circ}_{pm}(298)$ ($J\,K^{-1}\,mol^{-1}$)	$C^{\circ}_{pm}(298)$(NKR) ($J\,K^{-1}\,mol^{-1}$)	ΔC°_{pm} (%)	$C^{\circ}_{pm}(298)$(KK) ($J\,K^{-1}\,mol^{-1}$)	ΔC°_{pm} (%)	$C^{\circ}_{pm}(298)$(BB) ($J\,K^{-1}\,mol^{-1}$)	ΔC°_{pm} (%)
38	$Ca_2B_2O_5$	$2CaO{\cdot}B_2O_3$	Sol-A	[6]	147.08	147.82	0.51	146.17	−0.62		
39	$Ca_2Fe_2O_5$	$2CaO{\cdot}Fe_2O_3$	Sol	[1]	192.38	189.61	−1.44			191.53	−0.44
40	$Ca_2MgSi_2O_7$	$2CaO{\cdot}MgO{\cdot}2SiO_2$	Sol	[1]	210.97	210.94	−0.01	210.31	−0.31	211.57	0.28
41	Ca_2SiO_4	$2CaO{\cdot}SiO_2$	Sol-A	[60]	125.76	129.26	2.78	127.72	1.56	130.31	3.62
42	$Ca_3Al_2O_6$	$3CaO{\cdot}Al_2O_3$	Sol	[1]	208.79	206.27	−1.21	209.53	0.35	206.95	−0.88
43	$Ca_3Al_2Si_3O_{12}$	$3CaO{\cdot}Al_2O_3{\cdot}3SiO_2$	Sol	[1]	333.15	339.53	1.92	348.41	4.58	338.80	1.70
44	$Ca_3B_2O_6$	$3CaO{\cdot}B_2O_3$	Sol	[6]	187.86	190.24	1.27	185.27	−1.38		
45	$Ca_3Fe_2Si_3O_{12}$	$3CaO{\cdot}Fe_2O_3{\cdot}3SiO_2$	Sol	[15]	351.38	365.29	3.96	360.97	2.73	366.56	4.32
46	$Ca_3Ga_2Ge_3O_{12}$	$3CaO{\cdot}Ga_2O_3{\cdot}3GeO_2$	Sol	[61]	379.50	376.97	−0.67				
47	$Ca_3MgSi_2O_8$	$3CaO{\cdot}MgO{\cdot}2SiO_2$	Sol	[8]	252.26	253.36	0.44	250.41	−0.73	254.75	0.99
48	$Ca_3Si_2O_7$	$3CaO{\cdot}2SiO_2$	Sol	[60]	211.51	216.10	2.17	215.34	1.81	217.44	2.81
49	Ca_3SiO_5	$3CaO{\cdot}SiO_2$	Sol	[60]	171.61	171.68	0.04			173.49	1.10
50	$Ca_3Ti_2O_7$	$3CaO{\cdot}2TiO_2$	Sol	[6]	239.59	237.46	−0.89	241.04	0.61	240.42	0.35
51	$Ca_4Ti_3O_{10}$	$4CaO{\cdot}3TiO_2$	Sol	[6]	337.77	334.98	−0.83	340.18	0.71	339.04	0.38
52	$CaAl_2O_4$	$CaO{\cdot}Al_2O_3$	Sol	[6]	120.60	121.43	0.69	123.21	2.17	120.59	−0.01
53	$CaAl_2Si_2O_8$	$CaO{\cdot}Al_2O_3{\cdot}2SiO_2$	Sol	[8]	211.31	210.27	−0.49	220.69	4.44	208.49	−1.33
54	$CaAl_2SiO_6$	$CaO{\cdot}Al_2O_3{\cdot}SiO_2$	Sol	[1]	165.82	165.85	0.02			164.54	−0.77
55	$CaAl_4O_7$	$CaO{\cdot}2Al_2O_3$	Sol	[6]	199.57	200.44	0.44			198.00	−0.79
56	CaB_2O_4	$CaO{\cdot}B_2O_3$	Sol	[6]	103.99	105.40	1.36	107.07	2.97		
57	CaB_4O_7	$CaO{\cdot}2B_2O_3$	Sol	[6]	157.85	168.38	6.67	158.95	0.70		
58	$CaCrO_4$	$CaO{\cdot}CrO_3$	Sol	[62]	113.18	121.54	7.39	116.96	3.34		
59	$CaCr_2O_4$	$CaO{\cdot}Cr_2O_3$	Sol-B	[62]	139.31	156.68	12.47	150.03	7.70		
60	$CaFe_2O_4$	$CaO{\cdot}Fe_2O_3$	Sol	[6]	153.65	147.19	−4.20	150.75	−1.89	148.35	−3.45
61	$CaFeSi_2O_6$	$CaO{\cdot}FeO{\cdot}2SiO_2$	Sol	[15]	175.37	179.30	2.24	176.49	0.64	174.46	−0.52
62	$CaHfTi_2O_7$	$CaO{\cdot}HfO_2{\cdot}2TiO_2$	Sol	[63]	206.90	212.88	2.89	217.18	4.97		
63	$CaMgSi_2O_6$	$CaO{\cdot}MgO{\cdot}2SiO_2$	Sol	[1]	166.63	168.52	1.13	170.21	2.15	168.39	1.06
64	$CaMgSiO_4$	$CaO{\cdot}MgO{\cdot}SiO_2$	Sol	[6]	123.22	124.10	0.71	122.69	−0.43	124.44	0.99
65	$CaNb_2O_6$	$CaO{\cdot}Nb_2O_5$	Sol	[6]	177.34	174.55	−1.57	180.69	1.89		
66	$CaSiO_3$	$CaO{\cdot}SiO_2$	Sol-A	[60]	86.42	86.84	0.49	87.62	1.39	87.13	0.83
67	$CaTiO_3$	$CaO{\cdot}TiO_2$	Sol-A	[6]	97.70	97.52	−0.18	99.14	1.48	98.62	0.95
68	$CaTiSiO_5$	$CaO{\cdot}TiO_2{\cdot}SiO_2$	Sol	[1]	139.11	141.94	2.03	140.43	0.95	142.57	2.49
69	$CaUO_4$	$CaO{\cdot}UO_3$	Sol-A	[6]	130.45	123.61	−5.24	131.80	1.04		
70	$CaWO_4$	$CaO{\cdot}WO_3$	Sol	[6]	113.24	115.22	1.75	122.18	7.90		
71	$CaZrO_3$	$CaO{\cdot}ZrO_2$	Sol	[37]	99.91	98.63	−1.28	99.75	−0.16		
72	$CaZrTi_2O_7$	$CaO{\cdot}ZrO_2{\cdot}2TiO_2$	Sol	[64]	211.73	208.83	−1.37	215.51	1.78		
73	$CdTiO_3$	$CdO{\cdot}TiO_2$	Sol-A	[6]	98.50	99.26	0.77	97.46	−1.06		
74	$Ce_2Si_2O_7$	$Ce_2O_3{\cdot}2SiO_2$	Sol-B	[65]	204.41	205.89	0.72	188.13	−7.96		
75	$Ce_2Zr_2O_7$	$Ce_2O_3{\cdot}2ZrO_2$	Sol	[66]	233.74	229.47	−1.83				
76	Co_2SiO_4	$2CoO{\cdot}SiO_2$	Sol	[6]	133.95	154.86	15.61	134.40	0.33		
77	Co_2TiO_4	$2CoO{\cdot}TiO_2$	Sol	[6]	160.49	165.54	3.15	148.58	−7.42		

Table 5 (*Continued*)

No.	Mixed oxide	Binary oxides combination	Phase	Reference	$C^{\circ}_{pm}(298)$ ($J\,K^{-1}\,mol^{-1}$)	$C^{\circ}_{pm}(298)$(NKR) ($J\,K^{-1}\,mol^{-1}$)	ΔC°_{pm} (%)	$C^{\circ}_{pm}(298)$(KK) ($J\,K^{-1}\,mol^{-1}$)	ΔC°_{pm} (%)	$C^{\circ}_{pm}(298)$(BB) ($J\,K^{-1}\,mol^{-1}$)	ΔC°_{pm} (%)
78	Co_3O_4	$CoO{\cdot}Co_2O_3$	Sol	[6]	123.42						
79	$CoFe_2O_4$	$CoO{\cdot}Fe_2O_3$	Sol	[6]	152.58	159.99	4.86	154.09	0.99		
80	$CoTa_2O_6$	$CoO{\cdot}Ta_2O_5$	Sol	[67]	175.59	186.70	6.33				
81	$CoTiO_3$	$CoO{\cdot}TiO_2$	Sol	[6]	107.77	110.32	2.37	102.48	−4.91		
82	$CoWO_4$	$CoO{\cdot}WO_3$	Sol-A	[6]	129.94	128.02	−1.47	125.52	−3.40		
83	Cr_3O_4	$CrO{\cdot}Cr_2O_3$	Sol	[68]	135.64						
84	$CsBO_2$	$(Cs_2O{\cdot}B_2O_3)/2$	Sol	[6]	69.48	69.44	−0.05	67.55	−2.77		
85	$Cs_2Cr_2O_7$	$Cs_2O{\cdot}2CrO_3$	Sol-A	[54]	231.54	234.14	1.12				
86	Cs_2CrO_4	$Cs_2O{\cdot}CrO_3$	Sol-A	[54]	146.06	155.02	6.13	144.99	−0.73		
87	Cs_2MnO_4	$Cs_2O{\cdot}MnO_3$	Sol-A	[69]	149.24						
88	$Cs_2Mo_2O_7$	$Cs_2O{\cdot}2MoO_3$	Sol	[70]	224.14	226.18	0.91				
89	Cs_2MoO_4	$Cs_2O{\cdot}MoO_3$	Sol-A	[6]	148.67	151.04	1.59	145.49	−2.14		
90	Cs_2RuO_4	$Cs_2O{\cdot}RuO_3$	Sol-A	[69]	156.14						
91	$Cs_2Si_2O_5$	$Cs_2O{\cdot}2SiO_2$	Sol	[6]	176.73	164.74	−6.78	159.51	−9.74		
92	$Cs_2Si_4O_9$	$Cs_2O{\cdot}4SiO_2$	Sol	[6]	272.86	253.58	−7.06				
93	Cs_2SiO_3	$Cs_2O{\cdot}SiO_2$	Sol	[6]	122.23	120.32	−1.56	115.65	−5.38		
94	$Cs_2Te_2O_5$	$Cs_2O{\cdot}2TeO_2$	Sol	[54]	193.00	203.66	5.52				
95	$Cs_2Te_4O_{12}$	$Cs_2O{\cdot}TeO_2{\cdot}3TeO_3$	Sol	[54]	343.00	354.19	3.26				
96	$Cs_2Te_4O_9$	$Cs_2O{\cdot}4TeO_2$	Sol	[54]	318.20	331.42	4.16				
97	Cs_2TeO_3	$Cs_2O{\cdot}TeO_2$	Sol	[54]	133.87	139.78	4.42				
98	Cs_2TeO_4	$Cs_2O{\cdot}TeO_3$	Sol	[54]	148.35	147.37	−0.66				
99	$Cs_2U_2O_7$	$Cs_2O{\cdot}2UO_3$	Sol	[54]	231.23	238.28	3.05				
100	$Cs_2U_4O_{12}$	$Cs_2O{\cdot}UO_2{\cdot}3UO_3$	Sol-A	[54]	384.01	383.06	−0.25				
101	Cs_2UO_4	$Cs_2O{\cdot}UO_3$	Sol	[6]	152.75	157.09	2.84	159.83	4.64		
102	Cs_2ZrO_3	$Cs_2O{\cdot}ZrO_2$	Sol	[71]	129.79	132.11	1.79	127.78	−1.55		
103	Cs_3CrO_4	$(3Cs_2O{\cdot}CrO_2{\cdot}CrO_3)/2$	Sol-A	[54]	179.92						
104	$CsAlO_2$	$(Cs_2O{\cdot}Al_2O_3)/2$	Sol	[72]	79.76	77.46	−2.89	75.62	−5.19		
105	$CuFe_2O_4$	$CuO{\cdot}Fe_2O_3$	Sol-A	[6]	148.81	147.03	−1.19	151.16	1.58		
106	$CuFeO_2$	$(Cu_2O{\cdot}Fe_2O_3)/2$	Sol-A	[6]	84.18	85.12	1.12	88.13	4.69		
107	$Dy_3Fe_5O_{12}$	$(3Dy_2O_3{\cdot}5Fe_2O_3)/2$	Sol	[73]	442.72	436.32	−1.45				
108	Dy_3NbO_7	$(3Dy_2O_3{\cdot}Nb_2O_5)/2$	Sol	[74]	251.85	240.46	−4.52				
109	$DyCrO_3$	$(Dy_2O_3{\cdot}Cr_2O_3)/2$	Sol	[75]	102.33	115.26	12.64				
110	$Er_3Fe_5O_{12}$	$(3Er_2O_3{\cdot}5Fe_2O_3)/2$	Sol	[76]	449.52	424.66	−5.53				
111	Er_3NbO_7	$(3Er_2O_3{\cdot}Nb_2O_5)/2$	Sol	[74]	233.02	228.80	−1.81				
112	$ErCrO_3$	$(Er_2O_3{\cdot}Cr_2O_3)/2$	Sol	[75]	101.74	111.38	9.48				
113	$ErMnO_3$	$(Er_2O_3{\cdot}Mn_2O_3)/2$	Sol	[77]	104.81	103.77	−0.99				
114	$Eu_3Fe_5O_{12}$	$(3Eu_2O_3{\cdot}5Fe_2O_3)/2$	Sol	[76]	462.89	448.95	−3.01				
115	Eu_3NbO_7	$(3Eu_2O_3{\cdot}Nb_2O_5)/2$	Sol	[74]	251.01	253.09	0.83				
116	$Fe_2Al_4Si_5O_{18}$	$2FeO{\cdot}2Al_2O_3{\cdot}5SiO_2$	Sol	[15]	464.41	476.20	2.54	491.40	5.81	461.33	−0.66
117	Fe_2SiO_4	$2FeO{\cdot}SiO_2$	Sol	[8]	132.90	140.50	5.72	130.22	−2.02	130.71	−1.65

Table 5 (*Continued*)

No.	Mixed oxide	Binary oxides combination	Phase	Reference	$C^{\circ}_{pm}(298)$ ($J\,K^{-1}\,mol^{-1}$)	$C^{\circ}_{pm}(298)(NKR)$ ($J\,K^{-1}\,mol^{-1}$)	ΔC°_{pm} (%)	$C^{\circ}_{pm}(298)(KK)$ ($J\,K^{-1}\,mol^{-1}$)	ΔC°_{pm} (%)	$C^{\circ}_{pm}(298)(BB)$ ($J\,K^{-1}\,mol^{-1}$)	ΔC°_{pm} (%)
118	Fe_2TiO_4	$2FeO{\cdot}TiO_2$	Sol	[8]	142.30	151.18	6.24	144.40	1.48	142.20	−0.07
119	Fe_2TiO_5	$Fe_2O_3{\cdot}TiO_2$	Sol	[1]	163.85	159.87	−2.43			160.61	−1.98
120	$Fe_3Al_2Si_3O_{12}$	$3FeO{\cdot}Al_2O_3{\cdot}3SiO_2$	Sol	[15]	342.74	356.39	3.98	352.16	2.75	339.40	−0.97
121	Fe_3O_4	$FeO{\cdot}Fe_2O_3$	Sol	[6]	151.78	152.81	0.68	152.00	0.14	148.55	−2.13
122	$FeAl_2O_4$	$FeO{\cdot}Al_2O_3$	Sol	[15]	131.40	127.05	−3.31	124.46	−5.28	120.79	−8.07
123	$FeCr_2O_4$	$FeO{\cdot}Cr_2O_3$	Sol	[6]	133.81	162.30	21.29	151.28	13.06		
124	$FeSiO_3$	$FeO{\cdot}SiO_2$	Sol	[15]	88.12	92.46	4.93	88.87	0.85	87.33	−0.90
125	$FeTa_2O_6$	$FeO{\cdot}Ta_2O_5$	Sol	[67]	184.87	179.52	−2.89				
126	$FeTiO_3$	$FeO{\cdot}TiO_2$	Sol	[6]	99.50	103.14	3.66	100.39	0.89	98.82	−0.69
127	$Gd_3Fe_5O_{12}$	$(3Gd_2O_3{\cdot}5Fe_2O_3)/2$	Sol	[78]	433.06	420.19	−2.97				
128	$Gd_3Ga_5O_{12}$	$(3Gd_2O_3{\cdot}5Ga_2O_3)/2$	Sol	[61]	385.64	392.92	1.89				
129	Gd_3NbO_7	$(3Gd_2O_3{\cdot}Nb_2O_5)/2$	Sol	[74]	237.49	224.33	−5.54				
130	$GdCrO_3$	$(Gd_2O_3{\cdot}Cr_2O_3)/2$	Sol	[75]	99.52	109.89	10.42				
131	$Hg_{0.97}Ba_2CuO_{4.05}$		Sol	[79]	189.53						
132	$HgBaO_2$	$HgO{\cdot}BaO$	Sol	[80]	103.48	90.95	−12.11				
133	$HgCaO_2$	$HgO{\cdot}CaO$	Sol	[81]	96.31	86.31	−10.38				
134	$HgSrO_2$	$HgO{\cdot}SrO$	Sol	[80]	89.90	89.04	−0.96				
135	$Ho_3Fe_5O_{12}$	$(3Ho_2O_3{\cdot}5Fe_2O_3)/2$	Sol	[82]	451.52	434.37	−3.80				
136	Ho_3NbO_7	$(3Ho_2O_3{\cdot}Nb_2O_5)/2$	Sol	[74]	252.14	238.51	−5.41				
137	Ho_6WO_{12}	$3Ho_2O_3{\cdot}WO_3$	Sol	[83]	434.20	417.68	−3.80				
138	$HoCrO_3$	$(Ho_2O_3{\cdot}Cr_2O_3)/2$	Sol	[75]	101.60	114.61	12.81				
139	$K_2B_4O_7$	$K_2O{\cdot}2B_2O_3$	Sol	[6]	170.30	210.49	23.60	186.14	9.30		
140	$K_2B_6O_{10}$	$K_2O{\cdot}3B_2O_3$	Sol	[6]	265.34	273.47	3.07				
141	$K_2B_8O_{13}$	$K_2O{\cdot}4B_2O_3$	Sol	[6]	319.06	336.45	5.45				
142	K_2CrO_4	$K_2O{\cdot}CrO_3$	Sol-A	[6]	146.05	163.65	12.05	144.15	−1.30		
143	$K_2Si_2O_5$	$K_2O{\cdot}2SiO_2$	Sol-A	[6]	160.95	173.37	7.72	158.67	−1.41	159.60	−0.84
144	$K_2Si_4O_9$	$K_2O{\cdot}4SiO_2$	Sol	[84]	247.20	262.21	6.07			247.50	0.12
145	K_2SiO_3	$K_2O{\cdot}SiO_2$	Sol	[6]	118.70	128.95	8.64	114.81	−3.28	115.65	−2.57
146	$K_2W_2O_7$	$K_2O{\cdot}2WO_3$	Sol	[85]	221.00	230.13	4.13				
147	$K_2W_3O_{10}$	$K_2O{\cdot}3WO_3$	Sol	[85]	288.10	302.93	5.15				
148	$K_2W_4O_{13}$	$K_2O{\cdot}4WO_3$	Sol	[85]	356.40	375.73	5.42				
149	K_2WO_4	$K_2O{\cdot}WO_3$	Sol-A	[6]	150.81	157.33	4.32	149.37	−0.95		
150	$KAl_3Si_3O_{11}$	$(K_2O{\cdot}3Al_2O_3{\cdot}6SiO_2)/2$	Sol	[1]	287.37	294.04	2.32	304.53	5.97	283.82	−1.24
151	$KAlSi_2O_6$	$(K_2O{\cdot}Al_2O_3{\cdot}4SiO_2)/2$	Sol	[6]	164.30	170.61	3.84	171.46	4.36	162.46	−1.12
152	$KAlSi_3O_8$	$(K_2O{\cdot}Al_2O_3{\cdot}6SiO_2)/2$	Microcline	[1]	202.84	215.03	6.01	215.32	6.15	206.41	1.76
153	$KAlSi_3O_8$	$(K_2O{\cdot}Al_2O_3{\cdot}6SiO_2)/2$	Sanidine	[1]	205.28	215.03	4.75	215.32	4.89	206.41	0.55
154	$KAlSiO_4$	$(K_2O{\cdot}Al_2O_3{\cdot}2SiO_2)/2$	Sol	[6]	119.90	126.19	5.25	123.94	3.37	118.51	−1.16
155	KBO_2	$(K_2O{\cdot}B_2O_3)/2$	Sol	[6]	66.96	73.76	10.15	67.13	0.25		
156	$KDyMo_2O_8$	$(K_2O{\cdot}Dy_2O_3{\cdot}4MoO_3)/2$	Sol	[86]	235.90	250.68	6.26				

Table 5 (*Continued*)

No.	Mixed oxide	Binary oxides combination	Phase	Reference	$C^{\circ}_{pm}(298)$ ($J\,K^{-1}\,mol^{-1}$)	$C^{\circ}_{pm}(298)$(NKR) ($J\,K^{-1}\,mol^{-1}$)	ΔC°_{pm} (%)	$C^{\circ}_{pm}(298)$(KK) ($J\,K^{-1}\,mol^{-1}$)	ΔC°_{pm} (%)	$C^{\circ}_{pm}(298)$(BB) ($J\,K^{-1}\,mol^{-1}$)	ΔC°_{pm} (%)
157	$KErMo_2O_8$	$(K_2O{\cdot}Er_2O_3{\cdot}4MoO_3)/2$	Sol	[87]	233.40	246.79	5.74				
158	$KGdMo_2O_8$	$(K_2O{\cdot}Gd_2O_3{\cdot}4MoO_3)/2$	Sol-A	[88]	233.20	245.30	5.19	234.91	0.73		
159	$KHoMo_2O_8$	$(K_2O{\cdot}Ho_2O_3{\cdot}4MoO_3)/2$	Sol	[89]	232.50	250.03	7.54	234.49	0.86		
160	$KLuMo_2O_8$	$(K_2O{\cdot}Lu_2O_3{\cdot}4MoO_3)/2$	Sol	[90]	234.70	243.43	3.72				
161	$KTbMo_2O_8$	$(K_2O{\cdot}Tb_2O_3{\cdot}4MoO_3)/2$	Sol	[91]	236.80						
162	$KYbMo_2O_8$	$(K_2O{\cdot}Yb_2O_3{\cdot}4MoO_3)/2$	Sol	[92]	238.10	250.23	5.09				
163	$KYMo_2O_8$	$(K_2O{\cdot}Y_2O_3{\cdot}4MoO_3)/2$	Sol	[93]	232.10	243.80	5.04	236.58	1.93		
164	La_2CuO_4	$La_2O_3{\cdot}CuO$	Sol	[94]	151.30	151.04	−0.17				
165	$La_2Mo_3O_{12}$	$La_2O_3{\cdot}3MoO_3$	Sol	[6]	329.36	334.20	1.47	329.35	0.00		
166	La_2NiO_4	$La_2O_3{\cdot}NiO$	Sol	[95]	159.14	153.07	−3.81				
167	$La_2Si_2O_7$	$La_2O_3{\cdot}2SiO_2$	Sol-B	[65]	195.18	197.62	1.25	192.31	−1.47		
168	$La_2Zr_2O_7$	$La_2O_3{\cdot}2ZrO_2$	Sol	[66]	223.05	221.20	−0.83				
169	La_3NbO_7	$(3La_2O_3{\cdot}Nb_2O_5)/2$	Sol	[74]	235.68	229.24	−2.74				
170	$LaAlO_3$	$(La_2O_3{\cdot}Al_2O_3)/2$	Sol	[6]	92.64	93.90	1.36	93.25	0.66		
171	$LaCoO_3$	$(La_2O_3{\cdot}Co_2O_3)/2$	Sol	[96]	107.51						
172	$LaCrO_3$	$(La_2O_3{\cdot}Cr_2O_3)/2$	Sol	[75]	111.20	111.52	0.29				
173	$LaFeO_3$	$(La_2O_3{\cdot}Fe_2O_3)/2$	Sol	[96]	108.65	106.78	−1.72				
174	$LaMnO_3$	$(La_2O_3{\cdot}Mn_2O_3)/2$	Sol	[97]	102.79	103.91	1.09				
175	$LaMnO_{3.15}$		Sol	[80]	110.10						
176	$Li_2B_4O_7$	$Li_2O{\cdot}2B_2O_3$	Sol	[6]	179.32	180.21	0.50	173.58	−3.20		
177	$Li_2B_8O_{13}$	$Li_2O{\cdot}4B_2O_3$	Sol	[6]	324.23	306.17	−5.57				
178	$Li_2Si_2O_5$	$Li_2O{\cdot}2SiO_2$	Sol-A	[6]	138.77	143.09	3.11	146.11	5.29		
179	Li_2SiO_3	$Li_2O{\cdot}SiO_2$	Sol	[6]	100.00	98.67	−1.33	102.25	2.25		
180	$Li_2Ti_3O_7$	$Li_2O{\cdot}3TiO_2$	Sol	[98]	228.51	219.55	−3.92				
181	Li_2TiO_3	$Li_2O{\cdot}TiO_2$	Sol-A	[6]	109.68	109.35	−0.30	113.77	3.73		
182	Li_2ZrO_3	$Li_2O{\cdot}ZrO_2$	Sol	[99]	114.60	110.46	−3.61	114.38	−0.19		
183	Li_4SiO_4	$2Li_2O{\cdot}SiO_2$	Sol	[100]	155.23	152.92	−1.49	156.98	1.13		
184	$Li_4Ti_5O_{12}$	$2Li_2O{\cdot}5TiO_2$	Sol	[98]	361.54	384.00	6.21				
185	Li_8ZrO_6	$4Li_2O{\cdot}ZrO_2$	Sol	[99]	275.46	273.21	−0.82				
186	$LiAlO_2$	$(Li_2O{\cdot}Al_2O_3)/2$	Sol	[8]	67.83	66.63	−1.77	68.92	1.61		
187	$LiAlSi_2O_6$	$(Li_2O{\cdot}Al_2O_3{\cdot}4SiO_2)/2$	Sol-A	[6]	158.92	155.47	−2.17	165.18	3.94		
188	$LiAlSiO_4$	$(Li_2O{\cdot}Al_2O_3{\cdot}2SiO_2)/2$	Sol-A	[101]	111.15	111.05	−0.09	117.66	5.86		
189	LiB_3O_5	$(Li_2O{\cdot}3B_2O_3)/2$	Sol	[6]	145.52	121.60	−16.44				
190	$LiBO_2$	$(Li_2O{\cdot}B_2O_3)/2$	Sol	[6]	60.44	58.62	−3.02	60.85	0.68		
191	$LiFeO_2$	$(Li_2O{\cdot}Fe_2O_3)/2$	Sol	[6]	82.46	79.51	−3.58	82.62	0.19		
192	$Lu_3Fe_5O_{12}$	$(3Lu_2O_3{\cdot}5Fe_2O_3)/2$	Sol	[102]	424.90	414.57	−2.43				
193	Lu_3NbO_7	$(3Lu_2O_3{\cdot}Nb_2O_5)/2$	Sol	[74]	220.14	218.71	−0.65				
194	Lu_6WO_{12}	$3Lu_2O_3{\cdot}WO_3$	Sol	[83]	393.75	378.08	−3.98				
195	$Mg_2Al_4Si_5O_{18}$	$2MgO{\cdot}2Al_2O_3{\cdot}5SiO_2$	Sol	[1]	452.38	454.64	0.50	478.84	5.85	449.19	−0.71
196	Mg_2SiO_4	$2MgO{\cdot}SiO_2$	Sol	[6]	118.43	118.94	0.43	117.66	−0.65	118.57	0.12

Table 5 (*Continued*)

No.	Mixed oxide	Binary oxides combination	Phase	Reference	$C^{\circ}_{pm}(298)$ ($J\,K^{-1}\,mol^{-1}$)	$C^{\circ}_{pm}(298)(NKR)$ ($J\,K^{-1}\,mol^{-1}$)	ΔC°_{pm} (%)	$C^{\circ}_{pm}(298)(KK)$ ($J\,K^{-1}\,mol^{-1}$)	ΔC°_{pm} (%)	$C^{\circ}_{pm}(298)(BB)$ ($J\,K^{-1}\,mol^{-1}$)	ΔC°_{pm} (%)
197	Mg_2TiO_4	$2MgO{\cdot}TiO_2$	Sol	[6]	128.17	129.62	1.13	131.84	2.87	130.06	1.48
198	$Mg_3Al_2Si_3O_{12}$	$3MgO{\cdot}Al_2O_3{\cdot}3SiO_2$	Sol	[1]	324.76	324.05	−0.22	333.32	2.64	321.19	−1.10
199	$MgAl_2O_4$	$MgO{\cdot}Al_2O_3$	Sol	[6]	115.96	116.27	0.27	118.18	1.92	114.72	−1.07
200	$MgAl_2SiO_6$	$MgO{\cdot}Al_2O_3{\cdot}SiO_2$	Sol	[15]	160.27	160.69	0.26			158.67	−1.00
201	$MgCr_2O_4$	$MgO{\cdot}Cr_2O_3$	Sol	[6]	126.80	151.52	19.50	145.00	14.36		
202	$MgFe_2O_4$	$MgO{\cdot}Fe_2O_3$	Sol	[1]	142.94	142.03	−0.64	145.72	1.94	142.48	−0.32
203	$MgRh_2O_4$	$MgO{\cdot}Rh_2O_3$	Sol	[103]	129.84	126.38	−2.66				
204	$MgSiO_3$	$MgO{\cdot}SiO_2$	Sol-A	[6]	81.90	81.68	−0.27	82.59	0.84	81.26	−0.78
205	$MgTa_2O_6$	$MgO{\cdot}Ta_2O_5$	Sol	[67]	175.73	168.74	−3.98				
206	$MgTi_2O_5$	$MgO{\cdot}2TiO_2$	Sol	[6]	146.64	147.46	0.56	144.35	−1.56	148.19	1.06
207	$MgTiO_3$	$MgO{\cdot}TiO_2$	Sol	[6]	91.19	92.36	1.28	94.11	3.20	92.75	1.71
208	$MgUO_4$	$MgO{\cdot}UO_3$	Sol	[6]	156.51	118.45	−24.32	126.77	−19.00		
209	MgV_2O_6	$MgO{\cdot}V_2O_5$	Sol	[6]	156.35	164.63	5.30	162.74	4.09		
210	$MgWO_4$	$MgO{\cdot}WO_3$	Sol	[6]	109.89	110.06	0.16	117.15	6.61		
211	$Mn_2Al_4Si_5O_{18}$	$2MnO{\cdot}2Al_2O_3{\cdot}5SiO_2$	Sol	[15]	462.33	469.64	1.58	486.38	5.20		
212	$Mn_2Mo_3O_8$	$2MnO{\cdot}3MoO_2$	Sol	[104]	245.90	257.49	4.71				
213	Mn_2SiO_4	$2MnO{\cdot}SiO_2$	Sol	[6]	129.87	133.94	3.13	125.20	−3.60		
214	Mn_2TiO_4	$2MnO{\cdot}TiO_2$	Sol	[6]	144.60	144.62	0.01	139.38	−3.61		
215	$Mn_3Al_2Si_3O_{12}$	$3MnO{\cdot}Al_2O_3{\cdot}3SiO_2$	Sol	[15]	340.30	346.55	1.84	344.63	1.27		
216	Mn_3O_4	$MnO{\cdot}Mn_2O_3$	Tetra	[6]	140.53	143.80	2.33				
217	$MnMoO_4$	$MnO{\cdot}MoO_3$	Sol	[104]	115.77	119.90	3.57	116.20	0.37		
218	$MnSiO_3$	$MnO{\cdot}SiO_2$	Sol	[6]	86.39	89.18	3.23	86.36	−0.04		
219	$MnTiO_3$	$MnO{\cdot}TiO_2$	Sol	[6]	99.83	99.86	0.03	97.88	−1.95		
220	$MnWO_4$	$MnO{\cdot}WO_3$	Sol	[6]	124.08	117.56	−5.25	120.92	−2.55		
221	$Na_2B_4O_7$	$Na_2O{\cdot}2B_2O_3$	Sol	[6]	186.92	194.52	4.07	186.14	−0.42		
222	NaB_3O_5	$(Na_2O{\cdot}3B_2O_3)/2$	Sol	[6]	121.84	128.75	5.67				
223	$Na_2B_8O_{13}$	$Na_2O{\cdot}4B_2O_3$	Sol	[6]	304.89	320.48	5.11				
224	Na_2CrO_4	$Na_2O{\cdot}CrO_3$	Sol-A	[6]	142.78	147.68	3.43	144.15	0.96		
225	$Na_2Mo_2O_7$	$Na_2O{\cdot}2MoO_3$	Sol	[6]	216.67	218.84	1.00				
226	Na_2MoO_4	$Na_2O{\cdot}MoO_3$	Sol-A	[6]	141.46	143.70	1.58	144.65	2.26		
227	$Na_2Si_2O_5$	$Na_2O{\cdot}2SiO_2$	Sol-A	[6]	156.50	157.40	0.57	158.67	1.39	157.08	0.37
228	Na_2SiO_3	$Na_2O{\cdot}SiO_2$	Sol	[6]	111.81	112.98	1.04	114.81	2.68	113.13	1.18
229	$Na_2Ti_2O_5$	$Na_2O{\cdot}2TiO_2$	Sol	[6]	193.13	178.76	−7.44	176.57	−8.57	180.06	−6.77
230	$Na_2Ti_3O_7$	$Na_2O{\cdot}3TiO_2$	Sol	[1]	249.66	233.86	−6.33			235.50	−5.67
231	$Na_2Ti_6O_{13}$	$Na_2O{\cdot}6TiO_2$	Sol	[105]	397.23	399.16	0.49			401.82	1.16
232	Na_2TiO_3	$Na_2O{\cdot}TiO_2$	Sol-A	[1]	126.77	123.66	−2.45	126.33	−0.35	124.62	−1.70
233	$Na_2U_2O_7$	$Na_2O{\cdot}2UO_3$	Sol-A	[106]	227.26	230.94	1.62				
234	Na_2UO_4	$Na_2O{\cdot}UO_3$	Sol-A	[6]	146.74	149.75	2.05	158.99	8.35		
235	Na_2WO_4	$Na_2O{\cdot}WO_3$	Sol-A	[6]	141.77	141.36	−0.29	149.37	5.36		
236	$Na_2W_2O_7$	$Na_2O{\cdot}2WO_3$	Sol	[107]	214.22	214.16	−0.03				

Table 5 (*Continued*)

No.	Mixed oxide	Binary oxides combination	Phase	Reference	$C^{\circ}_{pm}(298)$ ($J\,K^{-1}\,mol^{-1}$)	$C^{\circ}_{pm}(298)(NKR)$ ($J\,K^{-1}\,mol^{-1}$)	ΔC°_{pm} (%)	$C^{\circ}_{pm}(298)(KK)$ ($J\,K^{-1}\,mol^{-1}$)	ΔC°_{pm} (%)	$C^{\circ}_{pm}(298)(BB)$ ($J\,K^{-1}\,mol^{-1}$)	ΔC°_{pm} (%)
237	$Na_2W_4O_{13}$	$Na_2O{\cdot}4WO_3$	Sol	[107]	354.45	359.76	1.50				
238	Na_2ZrO_3	$Na_2O{\cdot}ZrO_2$	Sol-A	[6]	131.20	124.77	−4.90	126.94	−3.25		
239	Na_4SiO_4	$2Na_2O{\cdot}SiO_2$	Sol	[6]	184.72	181.54	−1.72	182.10	−1.42	182.31	−1.30
240	$NaAlO_2$	$(Na_2O{\cdot}Al_2O_3)/2$	Sol-A	[6]	73.52	73.79	0.36	75.23	2.33	73.30	−0.30
241	$NaAlSi_2O_6$	$(Na_2O{\cdot}Al_2O_3{\cdot}4SiO_2)/2$	Sol	[6]	159.88	162.63	1.72	171.46	7.25	161.20	0.83
242	$NaAlSi_3O_8$	$(Na_2O{\cdot}Al_2O_3{\cdot}6SiO_2)/2$	Sol-A	[6]	204.85	207.05	1.07	215.32	5.11	205.15	0.15
243	$NaAlSiO_4$	$(Na_2O{\cdot}Al_2O_3{\cdot}2SiO_2)/2$	Sol	[8]	115.81	118.21	2.07	123.94	7.02	117.25	1.24
244	$NaBO_2$	$(Na_2O{\cdot}B_2O_3)/2$	Sol	[6]	65.85	65.77	−0.12	67.13	1.94		
245	$NaCrO_2$	$(Na_2O{\cdot}Cr_2O_3)/2$	Sol	[6]	89.41	91.41	2.24	88.61	−0.89		
246	$NaFeSi_2O_6$	$(Na_2O{\cdot}Fe_2O_3{\cdot}4SiO_2)/2$	Sol	[1]	170.17	175.51	3.14	177.74	4.45	175.08	2.89
247	$NaUO_3$	$(Na_2O{\cdot}UO_2{\cdot}UO_3)/2$	Sol	[108]	108.87	106.67	−2.02				
248	Nd_2NiO_4	$Nd_2O_3{\cdot}NiO$	Sol	[109]	160.22	155.63	−2.86				
249	Nd_3NbO_7	$(3Nd_2O_3{\cdot}Nb_2O_5)/2$	Sol	[74]	243.89	233.08	−4.44				
250	$NdAlO_3$	$(Nd_2O_3{\cdot}Al_2O_3)/2$	Sol	[110]	97.05	95.18	−1.93	92.00	−5.20		
251	$NdCrO_3$	$(Nd_2O_3{\cdot}Cr_2O_3)/2$	Sol	[75]	106.48	112.80	5.94				
252	$NdGaO_3$	$(Nd_2O_3{\cdot}Ga_2O_3)/2$	Sol	[111]	105.80	102.60	−3.02				
253	Ni_2SiO_4	$2NiO{\cdot}SiO_2$	Sol	[6]	127.02	133.00	4.71	133.56	5.15		
254	$NiTa_2O_6$	$NiO{\cdot}Ta_2O_5$	Sol	[67]	171.15	175.77	2.70				
255	$NiTiO_3$	$NiO{\cdot}TiO_2$	Sol	[6]	99.25	99.39	0.14	102.06	2.83		
256	Pb_2SiO_4	$2PbO{\cdot}SiO_2$	Sol-A	[6]	136.92	135.90	−0.74	131.90	−3.67		
257	Pb_3O_4	$PbO{\cdot}Pb_2O_3$	Sol	[6]	154.94						
258	Pb_4SiO_6	$4PbO{\cdot}SiO_2$	Sol	[6]	229.73	227.38	−1.02				
259	$PbSiO_3$	$PbO{\cdot}SiO_2$	Sol	[6]	89.13	90.16	1.16	89.71	0.66		
260	$PbTiO_3$	$PbO{\cdot}TiO_2$	Sol-A	[6]	104.40	100.84	−3.41	101.23	−3.04		
261	$PbWO_4$	$PbO{\cdot}WO_3$	Sol	[6]	119.64	118.54	−0.92	124.27	3.87		
262	Pr_2NiO_4	$Pr_2O_3{\cdot}NiO$	Sol	[95]	165.46	160.92	−2.74				
263	Pr_3NbO_7	$(3Pr_2O_3{\cdot}Nb_2O_5)/2$	Sol	[74]	250.21	241.01	−3.68				
264	$PrCrO_3$	$(Pr_2O_3{\cdot}Cr_2O_3)/2$	Sol	[75]	108.92	115.45	6.00				
265	$Rb_2Cr_2O_7$	$Rb_2O{\cdot}2CrO_3$	Sol	[112]	230.17	*236.94*	*2.94*				
266	$Rb_2Mo_2O_7$	$Rb_2O{\cdot}2MoO_3$	Sol	[70]	209.72	*228.98*	*9.18*				
267	$Rb_2Si_2O_5$	$Rb_2O{\cdot}2SiO_2$	Sol	[6]	170.72	*167.54*	*−1.86*	159.51	−6.56		
268	$Rb_2Si_4O_9$	$Rb_2O{\cdot}4SiO_2$	Sol	[6]	270.89	*256.38*	*−5.36*				
269	Rb_2SiO_3	$Rb_2O{\cdot}SiO_2$	Sol	[6]	117.45	*123.12*	*4.83*	115.65	−1.53		
270	$Rb_2U_2O_7$	$Rb_2O{\cdot}2UO_3$	Sol	[72]	258.24	*241.08*	*−6.65*				
271	$RbAlO_2$	$(Rb_2O{\cdot}Al_2O_3)/2$	Sol	[72]	77.31	*78.86*	*1.99*	75.62	−2.19		
272	$RbBO_2$	$(Rb_2O{\cdot}B_2O_3)/2$	Sol	[6]	73.46	*70.84*	*−3.57*	67.55	−8.05		
273	$ScMnO_3$	$(Sc_2O_3{\cdot}Cr_2O_3)/2$	Sol	[113]	102.40	96.49	−5.77				
274	$Sm_3Fe_5O_{12}$	$(3Sm_2O_3{\cdot}5Fe_2O_3)/2$	Sol	[114]	447.10	435.66	−2.56				
275	Sm_3NbO_7	$(3Sm_2O_3{\cdot}Nb_2O_5)/2$	Sol	[74]	240.06	239.80	−0.11				
276	$SmCrO_3$	$(Sm_2O_3{\cdot}Cr_2O_3)/2$	Sol	[75]	101.62	115.04	13.21				

Table 5 (*Continued*)

No.	Mixed oxide	Binary oxides combination	Phase	Reference	$C^{\circ}_{pm}(298)$ ($J\,K^{-1}\,mol^{-1}$)	$C^{\circ}_{pm}(298)(NKR)$ ($J\,K^{-1}\,mol^{-1}$)	ΔC°_{pm} (%)	$C^{\circ}_{pm}(298)(KK)$ ($J\,K^{-1}\,mol^{-1}$)	ΔC°_{pm} (%)	$C^{\circ}_{pm}(298)(BB)$ ($J\,K^{-1}\,mol^{-1}$)	ΔC°_{pm} (%)
277	$SmNiO_3$		Sol	[115]	110.58						
278	Sr_2CuO_3	$2SrO{\cdot}CuO$	Sol	[116]	134.87	132.56	−1.71				
279	Sr_2SiO_4	$2SrO{\cdot}SiO_2$	Sol	[6]	130.80	134.72	3.00	129.38	−1.08		
280	Sr_2TiO_4	$2SrO{\cdot}TiO_2$	Sol	[6]	143.68	145.40	1.19	143.56	−0.09		
281	$Sr_3MgSi_2O_8$	$3SrO{\cdot}MgO{\cdot}2SiO_2$	Sol	[117]	257.35	261.55	1.63	252.90	−1.73		
282	$Sr_3U_{11}O_{33}$	$3SrO{\cdot}3UO_2{\cdot}8UO_3$	Sol	[118]	1064.20	975.74	−8.31				
283	$Sr_3U_2O_9$	$3SrO{\cdot}2UO_3$	Sol	[118]	301.80	297.83	−1.32				
284	$Sr_4Ti_3O_{10}$	$4SrO{\cdot}3TiO_2$	Sol	[6]	341.89	345.90	1.17	343.50	0.47		
285	$Sr_{14}Cu_{24}O_{41}$		Sol	[116]	1730.76						
286	$SrAl_2O_4$	$SrO{\cdot}Al_2O_3$	Sol-A	[6]	119.03	124.16	4.31	124.04	4.21		
287	$SrAl_2Si_2O_8$	$SrO{\cdot}Al_2O_3{\cdot}2SiO_2$	Sol	[50]	221.22	213.00	−3.71	221.52	0.14		
288	$SrCeO_3$	$SrO{\cdot}CeO_2$	Sol	[119]	108.87	106.68	−2.01				
289	$SrCuO_2$	$SrO{\cdot}CuO$	Sol	[116]	86.75	87.41	0.76				
290	$SrMnO_3$	$SrO{\cdot}MnO_2$	Sol	[80]	108.73	99.57	−8.43				
291	$SrMoO_4$	$SrO{\cdot}MoO_3$	Sol	[6]	117.06	120.29	2.76	118.29	1.05		
292	$SrSiO_3$	$SrO{\cdot}SiO_2$	Sol	[120]	89.61	89.57	−0.04	88.45	−1.29		
293	$SrTiO_3$	$SrO{\cdot}TiO_2$	Sol	[6]	99.10	100.25	1.16	99.97	0.87		
294	$SrWO_4$	$SrO{\cdot}WO_3$	Sol	[6]	131.43	117.95	−10.26	123.01	−6.41		
295	$SrZrO_3$	$SrO{\cdot}ZrO_2$	Sol	[37]	103.43	101.36	−2.00	100.58	−2.76		
296	$SrZrSi_2O_7$	$SrO{\cdot}ZrO_2{\cdot}2SiO_2$	Sol	[121]	187.81	190.20	1.27	190.64	1.51		
297	$Tb_3Fe_5O_{12}$	$(3Tb_2O_3{\cdot}5Fe_2O_3)/2$	Sol	[122]	444.40	*425.28*	*−4.30*				
298	Tb_3NbO_7	$(3Tb_2O_3{\cdot}Nb_2O_5)/2$	Sol	[74]	243.48	*229.42*	*−5.78*				
299	$TbFeO_3$	$(Tb_2O_3{\cdot}Fe_2O_3)/2$	Sol	[123]	105.02	*106.84*	*1.73*				
300	$Tl_2Ba_2Ca_2Cu_3O_{10}$	$Tl_2O_3{\cdot}2BaO{\cdot}2CaO{\cdot}3CuO$	Sol	[124]	430.73	411.20	−4.53				
301	$Tl_2Ba_2CaCu_2O_8$	$Tl_2O_3{\cdot}2BaO{\cdot}CaO{\cdot}2CuO$	Sol	[124]	338.70	326.52	−3.60				
302	$Tl_{2.1}Ba_2CaCu_2O_{8.15}$	$1.05\ Tl_2O_3{\cdot}2BaO{\cdot}CaO{\cdot}2CuO$	Sol	[125]	339.56	331.79	−2.29				
303	$Tl_2Ba_2CuO_6$	$Tl_2O_3{\cdot}2BaO{\cdot}CuO$	Sol	[124]	249.37	241.84	−3.02				
304	$Tm_3Fe_5O_{12}$	$(3Tm_2O_3{\cdot}5Fe_2O_3)/2$	Sol	[82]	458.98	437.01	−4.79				
305	Tm_3NbO_7	$(3Tm_2O_3{\cdot}Nb_2O_5)/2$	Sol	[74]	245.52	241.15	−1.78				
306	$TmBa_2Cu_3O_7$		Sol	[126]	288.80						
307	$Y_2Cu_2O_5$	$Y_2O_3{\cdot}2CuO$	Sol	[127]	187.04	187.03	−0.01				
308	$Y_3Al_5O_{12}$	$(3Y_2O_3{\cdot}5Al_2O_3)/2$	Sol	[128]	348.13	351.29	0.91	358.54	2.99		
309	$Y_3Fe_5O_{12}$	$(3Y_2O_3{\cdot}5Fe_2O_3)/2$	Sol	[123]	426.77	415.69	−2.60				
310	Y_3NbO_7	$(3Y_2O_3{\cdot}Nb_2O_5)/2$	Sol	[74]	224.85	219.83	−2.23				
311	Yb_3NbO_7	$(3Yb_2O_3{\cdot}Nb_2O_5)/2$	Sol	[74]	245.21	239.11	−2.49				
312	$YBa_2Cu_3O_{6.7}$		Sol	[129]	285.80						
313	$YBa_2Cu_3O_{6.85}$		Sol	[129]	285.80						

Table 5 (*Continued*)

No.	Mixed oxide	Binary oxides combination	Phase	Reference	$C^{\circ}_{pm}(298)$ ($J\,K^{-1}\,mol^{-1}$)	$C^{\circ}_{pm}(298)$(NKR) ($J\,K^{-1}\,mol^{-1}$)	ΔC°_{pm} (%)	$C^{\circ}_{pm}(298)$(KK) ($J\,K^{-1}\,mol^{-1}$)	ΔC°_{pm} (%)	$C^{\circ}_{pm}(298)$(BB) ($J\,K^{-1}\,mol^{-1}$)	ΔC°_{pm} (%)
314	$YBa_2Cu_3O_{6.9}$		Sol	[130]	282.25						
315	$YBa_2Cu_3O_{6.96}$		Sol	[131]	281.20						
316	$YBa_2Cu_4O_8$		Sol	[130]	320.10						
317	$YbMnO_3$	$(Yb_2O_3{\cdot}Mn_2O_3)/2$	Sol	[132]	108.70	107.20	−1.38				
318	$YCrO_3$	$(Y_2O_3{\cdot}Cr_2O_3)/2$	Sol	[75]	97.21	108.39	11.50				
319	$YMnO_3$	$(Y_2O3{\cdot}Mn_2O_3)/2$	Sol	[132]	98.37	100.78	2.45				
320	Zn_2SiO_4	$2ZnO{\cdot}SiO_2$	Sol	[6]	121.83	126.56	3.88	121.86	0.02		
321	Zn_2TiO_4	$2ZnO{\cdot}TiO_2$	Sol	[6]	137.33	137.24	−0.06	136.04	−0.94		
322	$ZnFe_2O_4$	$ZnO{\cdot}Fe_2O_3$	Sol	[6]	137.33	145.84	6.19	147.82	7.64		
323	$ZnMn_2O_4$	$ZnO{\cdot}Mn_2O_3$	Sol	[133]	140.30	140.11	−0.14				
324	$ZnWO_4$	$ZnO{\cdot}WO_3$	Sol	[6]	125.50	113.87	−9.27	119.25	−4.98		
325	$ZrTiO_4$	$ZrO_2{\cdot}TiO2$	Sol	[134]	114.03	111.31	−2.39	116.37	2.05		
326	$ZrSiO_4$	$ZrO_2{\cdot}SiO_2$	Sol	[6]	98.57	100.63	2.09	102.19	3.67		

assumption that the predominant contribution to C°_{pm} of solids results from the lattice vibrational contribution and does not practically alter during the solid state reaction between the constituent compounds. On the contrary, the translational and, in case of polyatomic molecules, also rotational contributions dominate in gaseous state.

The average error of the estimated values was found 3.3%, whereas for 74 substances (25%) the error did not exceed 1%.

3.3. Kellogg's method

From the ionic contributions proposed by Spencer [18], the values of $C^{\circ}_{pm}(298.15\,\mathrm{K})$ were estimated for 169 mixed oxides with the average error of 3.1%, whereas for 47 substances (28%) the error did not exceed 1%. The accuracy of this method is comparable to that of the NKR—using the same set of substances the average error of the NKR was 3.2% and for 44 compounds did not exceed 1%. As to the universality, the NKR is better than the KK. Indeed, the KK is inapplicable almost for one half of mixed oxides included in the primary set.

3.4. Berman and Brown's method (BB)

Using the BB method the coefficients of $C^{\circ}_{pm}(T)$ dependence in Eq. (7) were estimated and the values of $C^{\circ}_{pm}(298.15\,\mathrm{K})$ for 68 mixed oxides were evaluated with the average error of 1.5%. For 31 compounds (46%), the error did not exceed 1%. The higher accuracy than for the NKR (average error 2.2% with the same set) is due to smaller universality of the BB method, which is applicable only for the one fifth of substances from the primary set.

4. Influence of C°_{pm} estimation error on the results of equilibrium calculations

Let us consider the formation reaction of the mixed oxide $RE_2Cu_2O_5$ (RE, rare earth element) in order to demonstrate the influence of molar heat capacity error on the results of equilibrium calculations. The reaction from binary oxides is described by the equation

$$2\,CuO(s) + Ln_2O_3(s) \rightarrow Ln_2Cu_2O_5(s) \qquad (R4)$$

As all involved substances are single-species phases, they can all coexist at certain equilibrium temperature, at which ΔG°_{r} (further denoted $\Delta G^{\circ}(ox)$) is equal zero. Since in general

$$\Delta G^{\circ}_{r} = \Delta H^{\circ}_{r} - T\Delta S^{\circ}_{r} \qquad (8)$$

this equilibrium temperature is given by the relation

$$T_{eq} = \frac{\Delta H^{\circ}(ox)}{\Delta S^{\circ}(ox)} \qquad (9)$$

The standard enthalpy and entropy, $\Delta H^{\circ}(ox)$ and $\Delta S^{\circ}(ox)$, respectively, of reaction (R4) are temperature dependent:

$$\Delta H^{\circ}(ox) = \Delta H^{\circ}(ox)(298.15\,\mathrm{K}) + \int_{298}^{T} \Delta C^{\circ}_{pm}(ox)\,dT \qquad (10)$$

$$\Delta S^{\circ}(ox) = \Delta S^{\circ}(ox)(298.15\,\mathrm{K}) + \int_{298}^{T} \frac{\Delta C^{\circ}_{pm}(ox)}{T}\,dT \qquad (11)$$

For the numerical calculation, the experimental data for $Yb_2Cu_2O_5$ reported by Jacob et al. [46] will be employed. The standard Gibbs energy of reaction (R4) has been obtained from the EMF measurements with solid electrolyte in the form of the linear temperature dependence

$$\Delta G^{\circ}(ox) = 9920 - 13.90T(J)$$
$$(T = 970\text{–}1323\,\mathrm{K}) \qquad (12)$$

The comparison with Eq. (8) yields for $Yb_2Cu_2O_5$ the values of $\Delta H^{\circ}(ox) = 9920$ J and $\Delta S^{\circ}(ox) = 13.9$ J. mol which can be assigned to the mean temperature of 1146.5 K. Under the assumption of both $\Delta H^{\circ}(ox)$ and $\Delta S^{\circ}(ox)$ being independent of temperature, i.e. $\Delta C^{\circ}_{pm}(ox) = 0$, the equilibrium temperature of $T_{eq} = 714$ K can be calculated from Eq. (9). For more precise calculation, the temperature dependencies of both $\Delta H^{\circ}(ox)$ and $\Delta S^{\circ}(ox)$ (Eqs. (10) and (11), respectively) are to be considered. As the experimental C°_{pm} data for $Yb_2Cu_2O_5$ are not available we have no choice but to use the estimated value. If we use the NKR $C^{\circ}_{pm}(Yb_2Cu_2O_5)(298.15\,\mathrm{K}) = 199.9\,\mathrm{J\,K^{-1}\,mol^{-1}}$ with the average estimation error 3.3%. We can expect $\Delta C^{\circ}_{pm}(ox)$ to fall in the interval $\langle -6.6; 6.6\rangle\,\mathrm{J\,K^{-1}\,mol^{-1}}$. Then, if $\Delta C^{\circ}_{pm}(ox)$ is temperature independent we obtain $T_{eq} = 750$ K and $T_{eq} = 654$ K

for the ultimate values of $\Delta C^{\circ}_{pm}(\mathrm{ox}) = 6.6$ and $-6.6\ \mathrm{J\ K^{-1}\ mol^{-1}}$, respectively.

5. Conclusions

The detailed assessment of three selected empirical methods applicable for prediction of heat capacities of mixed oxides revealed that the NKR can be used for rough estimates of $C^{\circ}_{pm}(298.15\ \mathrm{K})$. This method is highly universal, but in many cases the estimation error can exceed 5% (60 from 278 tested oxides), which is not acceptable in some types of thermodynamic calculations. More accurate values can be obtained using methods based on the individual contributions of binary oxides forming a given mixed oxide. The universality of such an approach is in the first place due to the extent of the evaluated contribution set. For instance, from the file of contributions assessed by Berman and Brown, a number of heat capacities of silicates and other oxide minerals can be predicted. The mean accuracy of such estimates is nearly comparable with experimental errors of DSC or drop calorimetry measurements of heat capacity. Thus a further extension and generalization of this method to other mixed oxide families like high-temperature oxide superconductors and related mixed oxides seem to be very promising. However, the oxygen non-stoichiometry of some phases will have to be taken into account (see Eq. (R3)) by evaluating the oxygen or O^{2-} anion contribution.

Acknowledgements

This work was supported by the Grant Agency of the Czech Republic, Grant No. 106/00/0568.

References

[1] R.G. Berman, T.H. Brown, Contrib. Mineral. Petrol. 89 (1985) 168.
[2] O. Kubaschewski, High Temp.—High Press. 4 (1972) 1.
[3] V.P. Glushko, L.V. Gurvich, G.A. Bergman, I.V. Veic, V.A. Medvedev, G.A. Khachkuruzov, V.S. Yungman, Thermodynamic Properties of Individual Substances, Tom I–IV, Nauka, Moskva, 1978–1982 (in Russian).
[4] L.B. Pankratz, Thermodynamic Properties of Elements and Oxides, Bulletin 672, US Bureau of Mines, Washington, 1982.
[5] I.S. Kulikov, Thermodynamics of Oxides, Metallurgiya, Moscow, 1986 (in Russian).
[6] O. Knacke, O. Kubaschewski, K. Hesselmann, Thermochemical Properties of Inorganic Substances, 2nd Edition, Springer, Berlin, 1991.
[7] O. Kubaschewski, C.B. Alcock, P.J. Spencer, Materials Thermochemistry, 6th Edition, Pergamon Press, Oxford, 1993.
[8] I. Barin, Thermochemical Data of Pure Substances, 3rd Edition, Wiley/VCH, Weinheim, 1995.
[9] M.W. Chase, Jr. (Ed.), NIST-JANAF Thermochemical Tables, 4th Edition, J. Phys. Chem. Ref. Data, Monograph No. 9, 1998.
[10] R.G. Berman, J. Petrol. 29 (1988) 445.
[11] T.J.B. Holland, R. Powel, J. Metamorphic Geol. 8 (1990) 89.
[12] S.K. Saxena, N. Chatterjee, Y. Fei, G. Shen, Thermodynamic Data on Oxides and Silicates, Springer, Berlin, 1993.
[13] R.A. Robie, B.S. Hemingway, Thermodynamic Properties of Minerals and Related Substances at 298.15 K and 1 bar Pressure and at Higher Temperatures, US Government and Printing Office, Washington 1995.
[14] M. Gottschalk, Eur. J. Miner. 9 (1997) 175.
[15] T.J.B. Holland, R. Powell, J. Metamorph. Geol. 16 (1998) 309.
[16] N.D. Chatterjee, R. Kruger, G. Haller, W. Olbricht, Contrib. Mineral. Petrol. 133 (1998) 149.
[17] G.K. Moiseev, J. Šesták, Prog. Cryst. Growth Charact. 30 (1995) 23.
[18] P.J. Spencer, Thermochim. Acta 314 (1998) 1.
[19] J. Leitner, P. Chuchvalec, D. Sedmidubský, Chem. Listy 95 (2001) 2.
[20] H.C. Helgeson, J.M. Delany, H.W. Nesbitt, D.K. Bird, Am. J. Sci. A 278 (1978) 1.
[21] K. Ukleba, G. Gvelesiani, J. Baratashvili, D. Tsagareishvili, J. Omiadze, A. Nadiradze, Bull. Georgian Acad. Sci. 156 (1997) 66.
[22] H.H. Kellogg, in: G.R. Fitterer (Ed.), Applications of Fundamental Thermodynamics to Metallurgical Processes, Gordon and Breach, London, 1967, p. 357.
[23] O. Kubaschewski, H. Ünal, High Temp.—High Press. 9 (1977) 361.
[24] V.N. Kumok, Problem of Correlation Methods for Evaluation of Thermodynamic Characteristics, Direct and Reverse Tasks of Chemical Thermodynamics, Nauka, Novosibirsk, 1987, p. 108 (in Russian).
[25] G.R. Robinson Jr., J.L. Haas Jr., Am. Miner. 68 (1983) 541.
[26] G.F. Voronin, I.A. Uspenskaya, Zh. Fiz. Khim. 71 (1997) 1927.
[27] O.Yu. Goncharov, Yu.P. Vorobev, Zh. Fiz. Khim. 73 (1999) 23.
[28] A.S. Pashinkin, A.S. Malkova, A.A. Ivanov, Neorg. Mater. 31 (1995) 1604.
[29] A.S. Malkova, A.S. Pashinkin, Neorg. Mater. 28 (1993) 240.
[30] M.K. Aldabergenov, G.T. Balakaeva, Zh. Fiz. Khim. 67 (1993) 425.
[31] M.K. Aldabergenov, G.T. Balakaeva, G.T. Kokibasova, Zh. Fiz. Khim. 72 (1998) 808.

[32] G.G. Gospodinov, D.I. Mihov, J. Chem. Thermodyn. 25 (1993) 1249.
[33] G.G. Gospodinov, J. Chem. Thermodyn. 26 (1994) 143.
[34] G.G. Gospodinov, J. Chem. Thermodyn. 26 (1994) 713.
[35] G.G. Gospodinov, J. Chem. Thermodyn. 26 (1994) 1111.
[36] G.G. Gospodinov, V.M. Marchev, Thermochim. Acta 222 (1993) 137.
[37] M.E. Huntelaar, E.H.P. Cordfunke, R.R. van der Laan, Thermochim. Acta 274 (1996) 101.
[38] K. Gavritchev, Thermochim. Acta 343 (2000) 63.
[39] B.K. Kasenov, M.A. Mukhanova, Sh.B. Kasenova, E.S. Mustafin, Zh. Fiz. Khim. 70 (1996) 24.
[40] Sh.B. Kasenova, B.K. Kasenov, E.S. Mustafin, M.K. Aldabergenov, Zh. Fiz. Khim. 71 (1997) 751.
[41] E.S. Mustafin, A.T. Oralova, B.K. Kasenov, Neorg. Mater. 30 (1994) 863.
[42] E.S. Mustafin, A.T. Oralova, B.K. Kasenov, Inorg. Mater. 31 (1995) 914.
[43] A.T. Oralova, B.K. Kasenov, M.M. Mataev, B.Z. Nurgaliev, Zh. Fiz. Khim. 70 (1996) 944.
[44] A.T. Oralova, E.S. Mustafin, B.K. Kasenov, Inorg. Mater. 32 (1996) 111.
[45] A.T. Oralova, B.K. Kasenov, E.S. Mustafin, High Temp. 34 (1996) 645.
[46] K.T. Jacob, T. Mathews, J.P. Hajra, High Temp. Mater. Processes 12 (1993) 251.
[47] P.G. Hall, D.A. Armitage, R.G. Linford, J. Chem. Thermodyn. 17 (1985) 657.
[48] E.H.P. Cordfunke, R.J.M. Konings, R.R. van der Laan, W. Ouweltjes, J. Chem. Thermodyn. 25 (1993) 343.
[49] N.F. Menshenina, A.A. Evdokimov, A.N. Klimenko, Zh. Neorg. Khim. 30 (1985) 568.
[50] I.V. Chernyshova, Yu.V. Semenov, V.M. Agoshov, M. Gambino, P. Gaune, J.P. Bros, Thermochim. Acta 175 (1991) 119.
[51] M.J. Scholten, J. Schoonman, J.C. van Miltenburg, E.H.P. Cordfunke, Thermochim. Acta 268 (1995) 161.
[52] K.S. Gavrichev, V.E. Gorbunov, L.N. Golushina, G.E. Nikiforova, G.A. Totrova, I.S. Shaplygin, Neorg. Mater. 29 (1993) 645.
[53] Yu.F. Minekov, N.I. Matskevich, Yu.G. Stenin, P.P. Samoilov, Thermochim. Acta 278 (1996) 1.
[54] E.H.P. Cordfunke, R.J.M. Konings (Eds.), Thermochemical Data for Reactor Materials and Fission Products, Elsevier, Amsterdam, 1990.
[55] M.E. Huntelaar, E.H.P. Cordfunke, G.D. Elzinga, R.R. van der Laan, J. Chem. Thermodyn. 32 (2000) 671.
[56] P. Abrman, D. Sedmidubský, A. Strejc, P. Voňka, J. Leitner, Thermochim. Acta 381 (2002) 1.
[57] M. Castro, R. Burriel, R. Ibanez, S. Fernando, IEEE Trans. Magn. 30 (1994) 1163.
[58] J. Leitner, D. Sedmidubský, A. Strejc, P. Abrman, B. Doušová, M. Nevřiva, in: B. Taraba (Ed.), Proceedings of the Calorim. Seminar 2000, University Ostrava, Ostrava, 2000, p. 9 (in Czech).
[59] K.S. Gavrichev, V.E. Gorbunov, I.A. Konovalova, V.B. Lazarev, E.A. Tishchenko, I.S. Shaplygin, Izv. Akad. Nauk SSSR, Neorg. Mater. 26 (1990) 1102.
[60] J.R. Taylor, A.T. Dinsdale, CALPHAD 14 (1990) 71.
[61] A.S. Malkova, A.S. Pashinkin, Neorg. Mater. 28 (1993) 240.
[62] M.Y. Lee, C.L. Nassaralla, Thermochim. Acta 371 (2001) 1.
[63] R.L. Putnam, A. Navrotsky, B.F. Woodfield, J.L. Shapiro, R. Stevens, J. Boerio-Goates, Mat. Res. Soc. Symp. Proc. 556 (1999) 11.
[64] B.F. Woodfield, J. Boerio-Goates, J.L. Shapiro, R.L. Putnam, A. Navrotsky, J. Chem. Thermodyn. 31 (1999) 245.
[65] M. Bolech, E.H.P. Cordfunke, A.C.G. van Genderen, R.R. van der Laan, F.J.J.G. Janssen, J.C. van Miltenburg, Thermochim. Acta 284 (1996) 253.
[66] M. Bolech, E.H.P. Cordfunke, A.C.G. van Genderen, R.R. van der Laan, F.J.J.G. Janssen, J.C. van Miltenburg, J. Phys. Chem. Solids 58 (1997) 433.
[67] M.A. White, G. Neshvad, J. Chem. Thermodyn. 23 (1991) 455.
[68] J.R. Taylor, A.T. Dinsdale, Z. Metallkd. 81 (1990) 354.
[69] E.H.P. Cordfunke, R.R. van der Laan, E.F. Westrum Jr., J. Chem. Thermodyn. 24 (1992) 815.
[70] R. Kohli, Thermochim. Acta 237 (1994) 241.
[71] R.P.C. Schram, V.M. Smit-Groen, E.H.P. Cordfunke, J. Chem. Thermodyn. 31 (1999) 43.
[72] R. Kohli, J. Therm. Anal. 49 (1997) 1321.
[73] T.B. Mirianashvili, T.A. Pavleniashvili, V.S. Varazashvili, D.I. Khutsishvili, M.S. Tsarakhov, G.D. Chachanidze, D.Sh. Tsagareishvili, Neorg. Mater. 29 (1993) 876.
[74] A.N. Klimenko, Yu.S. Kozlov, V.S. Sergeev, E.A. Pastukhov, Thermochim. Acta 209 (1992) 331.
[75] H. Satoh, S. Koseki, M. Takagi, W.Y. Chung, N. Kamegashira, J. Alloys Compd. 259 (1997) 176.
[76] V.S. Varazashvili, M.S. Tsarakhov, G.D. Chachanidze, Izv. Akad. Nauk SSSR, Neorg. Mater. 26 (1990) 602.
[77] H. Satoh, T. Shoji, J. Iwasaki, N. Kamegashira, Thermochim. Acta 261 (1995) 47.
[78] V.S. Varazashvili, T.A. Pavleniashvili, M.S. Tsarakhov, D.I. Khutsishvili, Neorg. Mater. 28 (1992) 2029.
[79] V.A. Aleshin, M.V. Gorbacheva, A.F. Maiorova, D.A. Mikhailova, S.N. Mudretsova, Zh. Fiz. Khim. 72 (1998) 421.
[80] D. Sedmidubský, A. Strejc, Unpublished results, 2000.
[81] D. Sedmidubský, J. Leitner, K. Knížek, A. Strejc, M. Veverka, Physica C 329 (2000) 191.
[82] V.S. Varazashvili, T.B. Mirianashvili, M.S. Tsarakhov, D.S. Tsagareishvili, Soobshch. Akad. Nauk Gruz. 142 (1991) 337.
[83] V.P. Marin, A.N. Klimenko, V.A. Levitskii, Yu.V. Menshenin, Yu.Ya. Skolis, Izv. Akad. Nauk SSSR, Neorg. Mater. 20 (1984) 461.
[84] D.W. Fasshauer, B. Wunder, N. Chatterjee, G.W.H. Hohne, Contrib. Mineral. Petrol. 131 (1998) 210.
[85] Q. Chen, S. Liu, P. Zhang, J. Chem. Thermodyn. 31 (1999) 531.
[86] G.I. Frolova, P.V. Klevtsov, I.E. Paukov, Zh. Fiz. Khim. 56 (1982) 710.
[87] G.I. Frolova, S.G. Kozlova, I.E. Paukov, Zh. Fiz. Khim. 55 (1981) 512.
[88] G.I. Frolova, L.P. Kozeeva, I.E. Paukov, Zh. Fiz. Khim. 57 (1983) 2150.

[89] G.A. Berezovskii, L.P. Kozeeva, I.E. Paukov, G.I. Frolova, S.V. Khegai, Zh. Fiz. Khim. 59 (1985) 49.
[90] G.I. Frolova, L.P. Kozeeva, I.E. Paukov, Zh. Fiz. Khim. 54 (1980) 336.
[91] G.A. Berezovskii, L.P. Kozeeva, I.E. Paukov, G.I. Frolova, S.V. Khegai, Zh. Fiz. Khim. 59 (1985) 744.
[92] G.I. Frolova, L.P. Kozeeva, I.E. Paukov, Zh. Fiz. Khim. 58 (1984) 2629.
[93] G.I. Frolova, L.P. Kozeeva, I.E. Paukov, Zh. Fiz. Khim. 57 (1983) 1802.
[94] V.E. Gorbunov, K.S. Gavrichev, G.A. Sharpataya, I.S. Shaplygin, V.L. Zalukaev, Zh. Neorg. Khim. 26 (1981) 547.
[95] M. Castro, R. Burriel, Thermochim. Acta 269/270 (1995) 537.
[96] S. Stølen, F. Grønvold, H. Brinks, T. Atake, H. Mori, J. Chem. Thermodyn. 30 (1998) 365.
[97] H. Satoh, M. Takagi, K. Kinukawa, N. Kamegashira, Thermochim. Acta 299 (1997) 123.
[98] V.I. Kolotyrkin, J.A. Kessler, V.A. Shchelkotunov, I.V. Gordeyev, Yu.G. Metlin, Yu.D. Tretyakov, Thermochim. Acta 43 (1981) 27.
[99] E.H.P. Cordfunke, R.R. van der Laan, G.P. Wyers, J.C. van Miltenburg, J. Chem. Thermodyn. 24 (1992) 1251.
[100] M. Asou, T. Terai, Y. Takahashi, J. Chem. Thermodyn. 24 (1992) 273.
[101] D.W. Fasshauer, N. Chatterjee, L. Cemic, Contrib. Mineral. Petrol. 133 (1998) 186.
[102] T.B. Mirianashvili, V.S. Varazashvili, M.S. Tsarakhov, K.S. Gavrichev, L.M. Golushina, V.E. Gorbunov, D.Sh. Tsagareishvili, Zh. Fiz. Khim. 72 (1998) 16.
[103] J. Nell, H.St.C. O'Neill, Geochim. Cosmochim. Acta 61 (1997) 4159.
[104] V.G. Bessergenev, Yu.A. Kovalenskaya, I.E. Paukov, M.A. Starikov, H. Oppermann, W. Reichelt, J. Chem. Thermodyn. 24 (1992) 85.
[105] M.J. Ferrante, Rep. Invest.—US, Bur. Mines, RI 9018 (1986).
[106] E.H.P. Cordfunke, R.P. Muis, W. Ouweltjes, H.E. Flotow, P.A.G. O'Hare, J. Chem. Thermodyn. 14 (1982) 313.
[107] S. Liu, Q. Chen, P. Zhang, Thermochim. Acta 371 (2001) 7.
[108] W.G. Lyon, D.W. Osborne, H.E. Flotow, H.R. Hoekstra, J. Chem. Thermodyn. 9 (1977) 201.
[109] M. Castro, R. Burriel, Thermochim. Acta 269/270 (1995) 523.
[110] R.R. van der Laan, R.J.M. Konings, A.C.G. van Genderen, J.C. van Miltenburg, Thermochim. Acta 329 (1999) 1.
[111] K.S. Gavrichev, V.E. Gorbunov, L.N. Golushina, G.A. Totrova, E.A. Tishchenko, Yu.G. Nadtochii, Ya.B. Polyarkov, Neorg. Mater. 30 (1994) 1443.
[112] R. Kohli, Thermochim. Acta 237 (1994) 235.
[113] H.W. Xu, J. Iwasaki, T. Shimizu, H. Satoh, N. Kamegashira, J. Alloys Compd. 221 (1995) 274.
[114] T.A. Pavlenishvili, M.S. Tsarakhov, V.S. Varazashvili, D.I. Khutsishvili, G.D. Chachanidze, Izv. Akad. Nauk SSSR, Neorg. Mater. 27 (1991) 99.
[115] J. Peréz, J. Blasco, J. García, M. Castro, J. Stankiewicz, M.C. Sánchez, R.D. Sánchez, J. Magn. Magn. Mater. 196/197 (1999) 541.
[116] R. Shaviv, E.F. Westrum Jr., T.L. Yang, C.B. Alcock, B. Li, J. Chem. Thermodyn. 22 (1990) 1025.
[117] M.E. Huntelaar, A.S. Booij, E.H.P. Cordfunke, R.R. van der Laan, J. Chem. Thermodyn. 30 (1998) 497.
[118] S. Dash, Z. Singh, R. Prasad, V. Venugopal, J. Nucl. Mater. 279 (2000) 84.
[119] E.H.P. Cordfunke, A.S. Booij, M.E. Huntelaar, J. Chem. Thermodyn. 30 (1998) 437.
[120] M.E. Huntelaar, E.H.P. Cordfunke, E.F. Westrum Jr., J. Phys. Chem. Solids 53 (1992) 801.
[121] M.E. Huntelaar, E.H.P. Cordfunke, J.C. van Miltenburg, Thermochim. Acta 254 (1995) 11.
[122] M.S. Tsarakhov, K.S. Gavrichev, V.S. Varazashvili, V.E. Gorbunov, L.N. Golushina, Zh. Fiz. Khim. 64 (1990) 550.
[123] V.A. Shchelkotunov, V.N. Danilob, L.A. Reznitskii, A.V. Korobeinikova, Izv. Akad. Nauk SSSR, Neorg. Mater. 11 (1975) 1633.
[124] A. Junod, D. Eckert, G. Triscone, V.Y. Lee, J. Muller, Phusica C 159 (1989) 215.
[125] T. Atake, H. Kawaji, M. Itoh, T. Nakamura, Y. Saito, Thermochim. Acta 183 (1991) 143.
[126] T. Atake, H. Kawaji, S. Takanabe, Y. Saito, Thermochim. Acta 139 (1989) 169.
[127] K.S. Gavrichev, V.E. Gorbunov, L.N. Golushina, V.B. Lazarev, G.E. Nikiforova, N.F. Vedernikov, G.A. Totrova, I.S. Shaplygin, Zh. Neorg. Khim. 37 (1992) 1583.
[128] R.J.M. Konings, R.R. van der Laan, A.C.G. van Genderen, J.C. van Miltenburg, Thermochim. Acta 313 (1998) 201.
[129] K.S. Gavrichev, V.E. Gorbunov, I.A. Konovalova, V.B. Lazarev, E.A. Tishchenko, I.S. Shaplygin, Izv. Akad. Nauk SSSR, Neorg. Mater. 24 (1988) 343.
[130] A. Junod, D. Eckert, T. Graf, E. Kaldis, J. Karpinski, S. Rusiecki, D. Sanchez, G. Triscone, J. Muller, Phusica C 168 (1990) 47.
[131] T. Atake, A. Honda, H. Kawaji, Physica C 190 (1991) 70.
[132] H. Satoh, J. Iwasaki, K. Kawase, N. Kamegashira, J. Alloys Compd. 268 (1998) 42.
[133] K. Chhor, J.F. Bocquet, C. Pommier, B. Chardon, J. Chem. Thermodyn. 18 (1986) 89.
[134] B.K. Hom, R. Stevens, B.F. Woodfield, J. Boero-Goates, R.L. Putnam, K.B. Helean, A. Navrotsky, J. Chem. Thermodyn. 33 (2001) 165.

WVMP SAR Reference 3-15

Spent Fuel Transportation Package Response to the Baltimore Tunnel Fire Scenario, NUREG/CR-686, Revision 2 (PNNL-15313), Adkins, H.E., Jr., J.M. Cuta, B.J. Koeppel, A.D. Guzman, and C.S. Bajwa, U. S. Nuclear Regulatory Commission, Washington, D.C., February 2009.

U.S.NRC
United States Nuclear Regulatory Commission
Protecting People and the Environment

NUREG/CR-6886, Rev. 2
PNNL-15313

Spent Fuel Transportation Package Response to the Baltimore Tunnel Fire Scenario

Office of Nuclear Materials Safety and Safeguards

AVAILABILITY OF REFERENCE MATERIALS IN NRC PUBLICATIONS

NRC Reference Material

As of November 1999, you may electronically access NUREG-series publications and other NRC records at NRC's Public Electronic Reading Room at http://www.nrc.gov/reading-rm.html. Publicly released records include, to name a few, NUREG-series publications; *Federal Register* notices; applicant, licensee, and vendor documents and correspondence; NRC correspondence and internal memoranda; bulletins and information notices; inspection and investigative reports; licensee event reports; and Commission papers and their attachments.

NRC publications in the NUREG series, NRC regulations, and *Title 10, Energy*, in the Code of *Federal Regulations* may also be purchased from one of these two sources.

1. The Superintendent of Documents
   U.S. Government Printing Office
   Mail Stop SSOP
   Washington, DC 20402–0001
   Internet: bookstore.gpo.gov
   Telephone: 202-512-1800
   Fax: 202-512-2250
2. The National Technical Information Service
   Springfield, VA 22161–0002
   www.ntis.gov
   1–800–553–6847 or, locally, 703–605–6000

A single copy of each NRC draft report for comment is available free, to the extent of supply, upon written request as follows:

Address: U.S. Nuclear Regulatory Commission
Office of Administration
Mail, Distribution and Messenger Team
Washington, DC 20555-0001
E-mail: DISTRIBUTION@nrc.gov
Facsimile: 301–415–2289

Some publications in the NUREG series that are posted at NRC's Web site address http://www.nrc.gov/reading-rm/doc-collections/nuregs are updated periodically and may differ from the last printed version. Although references to material found on a Web site bear the date the material was accessed, the material available on the date cited may subsequently be removed from the site.

Non-NRC Reference Material

Documents available from public and special technical libraries include all open literature items, such as books, journal articles, and transactions, *Federal Register* notices, Federal and State legislation, and congressional reports. Such documents as theses, dissertations, foreign reports and translations, and non-NRC conference proceedings may be purchased from their sponsoring organization.

Copies of industry codes and standards used in a substantive manner in the NRC regulatory process are maintained at—

The NRC Technical Library
Two White Flint North
11545 Rockville Pike
Rockville, MD 20852–2738

These standards are available in the library for reference use by the public. Codes and standards are usually copyrighted and may be purchased from the originating organization or, if they are American National Standards, from—

American National Standards Institute
11 West 42nd Street
New York, NY 10036–8002
www.ansi.org
212–642–4900

Legally binding regulatory requirements are stated only in laws; NRC regulations; licenses, including technical specifications; or orders, not in NUREG-series publications. The views expressed in contractor-prepared publications in this series are not necessarily those of the NRC.

The NUREG series comprises (1) technical and administrative reports and books prepared by the staff (NUREG–XXXX) or agency contractors (NUREG/CR–XXXX), (2) proceedings of conferences (NUREG/CP–XXXX), (3) reports resulting from international agreements (NUREG/IA–XXXX), (4) brochures (NUREG/BR–XXXX), and (5) compilations of legal decisions and orders of the Commission and Atomic and Safety Licensing Boards and of Directors' decisions under Section 2.206 of NRC's regulations (NUREG–0750).

U.S.NRC
United States Nuclear Regulatory Commission
Protecting People and the Environment

NUREG/CR-6886, Rev. 2
PNNL-15313

Spent Fuel Transportation Package Response to the Baltimore Tunnel Fire Scenario

Manuscript Completed: October 2006
Date Published: February 2009

Prepared by
H. E. Adkins, Jr. (PNNL)
J.M. Cuta (PNNL)
B.J. Koeppel (PNNL)
A.D. Guzman (PNNL)
C.S. Bajwa (NRC)

Pacific Northwest National Laboratory
902 Battelle Boulevard
Richland, WA 99352

C.S. Bajwa, NRC Project Manager

NRC Job Code J5167

Office of Nuclear Materials Safety and Safeguards

ABSTRACT

On July 18, 2001, a freight train carrying hazardous (non-nuclear) materials derailed and caught fire while passing through the Howard Street railroad tunnel in downtown Baltimore, Maryland. The United States Nuclear Regulatory Commission (USNRC), one of the agencies responsible for ensuring the safe transportation of radioactive materials in the United States, undertook an investigation of the train derailment and fire to determine the possible regulatory implications of this particular event for the transportation of spent nuclear fuel by railroad.

The USNRC met with the National Transportation Safety Board (NTSB) to discuss the details of the accident and the ensuing fire. Following these discussions, the USNRC assembled a team of experts from the National Institute of Standards and Technology (NIST), the Center for Nuclear Waste Regulatory Analyses (CNWRA), and Pacific Northwest National Laboratory (PNNL) to determine the thermal conditions that existed in the Howard Street tunnel fire and analyze the potential effects of those conditions on various spent nuclear fuel transportation package designs.

The Fire Dynamics Simulator (FDS) code developed by NIST was used to determine the thermal environment in the Howard Street tunnel during the fire. The FDS results were used as boundary conditions for the COBRA-SFS and ANSYS® computer models developed to evaluate the thermal performance of different package designs. The staff concluded that larger transportation packages resembling the TransNuclear Model No. TN-68 and HOLTEC Model No. HI-STAR 100 would withstand a fire with thermal conditions similar to those that existed in the Baltimore tunnel fire event with only minor damage to peripheral components. This is due to their sizable thermal inertia and design specifications in compliance with currently imposed regulatory requirements.

For the TN-68 and the NAC International Model No. LWT (legal weight truck) transportation package, the maximum temperatures predicted in the regions of the lid and the vent and drain ports exceed the seals' rated service temperatures, making it possible for a small release to occur, due to CRUD that might spall off the surfaces of the fuel rods. While a release is not expected to occur for these conditions, any release that could occur would be very small due to a number of factors. These include (1) the tight clearances maintained between the lid and cask body by the closure bolts, (2) the low pressure differential between the package interior and exterior, (3) the tendency of such small clearances to plug, and (4) the tendency of CRUD particles to settle or plate out.

USNRC staff evaluated the radiological con-sequences of the package responses to the Baltimore tunnel fire. The analysis indicates that the regulatory dose rate limits specified in 10 CFR 71.51 for accident conditions would not be exceeded by releases or direct radiation from any of these packages in this fire scenario. All three packages are designed to maintain regulatory dose rate limits even with a complete loss of neutron shielding (as documented in their respective SAR analyses). While highly unlikely, the NAC LWT could experience some decrease in gamma shielding due to slump in the lead as a consequence of this fire scenario, but a conservative analysis shows that the regulatory dose rate limits would not be exceeded.

The results of this evaluation also strongly indicate that neither spent nuclear fuel (SNF) particles nor fission products would be released from a spent fuel transportation package carrying intact spent fuel involved in a severe tunnel fire such as the Baltimore tunnel fire. None of the three package designs analyzed for the Baltimore tunnel fire scenario (TN-68, HI-STAR 100, and NAC LWT) experienced internal temperatures that would result in rupture of the fuel cladding. Therefore, radioactive material (i.e., SNF particles or fission products) would be retained within the fuel rods.

There would be no release from the HI-STAR 100, because the inner welded canister remains leak tight. While a release is unlikely, the potential releases calculated for the TN-68 rail package and the NAC LWT truck package indicate that any release of CRUD from either package would be very small - less than an A_2 quantity (see Section 8.2).

CONTENTS

FIGURES

TABLES

APPENDICES

ABBREVIATIONS

APDL	ANSYS® Parametric Design Language
BTF	Baltimore Tunnel Fire
BWR	Boiling Water Reactor
CFD	Computational Fluid Dynamics
CoC	Certificate of Compliance
CNWRA	Center for Nuclear Waste Regulatory Analyses
CRUD	Chalk River Unknown Deposit (generic term for various residues deposited on fuel rod surfaces, originally coined by Atomic Energy of Canada, Ltd. (AECL) to describe deposits observed on fuel removed from the test reactor at Chalk River.)
DOT	Department of Transportation
FDS	Fire Dynamics Simulator (computational fluid dynamics computer code)
FEA	Finite Element Analysis
HLW	High Level Waste
IAEA	International Atomic Energy Agency
ISO	International Organization for Standardization (The International Organization for Standardization has decreed the use of the initials ISO for reference to the organization, regardless of the word order of the organization's name in any given language. This defines a uniform acronym in all languages.)
MPC	Multi-Purpose Canister
NIST	National Institute of Standards and Technology
NTSB	National Transportation Safety Board
OFA	Optimized Fuel Assembly
PB	Personnel Barrier
PNNL	Pacific Northwest National Laboratory

PWR	Pressurized Water Reactor
SFST	USNRC Division of Spent Fuel Storage and Transportation
SNF	Spent nuclear fuel
USNRC	United States Nuclear Regulatory Commission

1 INTRODUCTION

Current USNRC regulations specify that spent nuclear fuel (SNF) transportation packages must be designed to survive exposure to a fully engulfing fire accident lasting no less than 30 minutes with an average flame temperature of no less than 1475°F (802°C) [1]. The package must maintain containment, shielding, and criticality functions throughout the fire event and post-fire cool down in order to meet USNRC requirements. (The term "package" refers to both the contents, in this case spent nuclear fuel, and the protective enclosing structure in which the contents are placed.)

The intent of the regulations is to ensure that spent fuel packages survive real world accidents, including those involving severe fires. The performance of spent fuel packages in severe accidents has been examined in previous studies by the NRC, as documented in NUREG-0170 (*Final Environmental Statement on the Transportation of Radioactive Material by Air and Other Modes*[1]), NUREG/CR-4829 (*Shipping Container Response to Severe Highway and Railway Accident Conditions*[2], also known as the "Modal Study"), and NUREG/CR-6672 (*Re-examination of Spent Fuel Shipment Risk Estimates*[3]). However, these studies did not explicitly examine historical accidents involving severe rail tunnel fires.

On July 18, 2001, a CSX freight train carrying hazardous (non-nuclear) materials derailed and caught fire while passing through the Howard Street railroad tunnel in downtown Baltimore, Maryland. (The event is described in Section 1.3.) The staff of the USNRC Division of Spent Fuel Storage and Transportation (SFST), formerly the Spent Fuel Project Office, undertook an investigation of the derailment and fire in order to determine what impact this event might have on the risk associated with spent nuclear fuel transportation by rail. This evaluation included an assessment of the potential severity of a tunnel fire compared to a fully engulfing fire, a review of the frequency of rail transportation accidents involving severe fires, and an analytical evaluation of the response of representative licensed SNF transportation packages to the conditions of the Baltimore tunnel fire.

1.1 Evaluation of Tunnel Fire Characteristics

The 30-minute fully engulfing fire prescribed in the current USNRC regulations defines a bounding fire for essentially all credible fire accidents involving SNF shipping packages. A fully engulfing open pool fire would generally be expected to subject a package to the hottest possible conditions for a given fuel supply. However, when considering potential accidents involving rail transport of SNF or high level waste (HLW), it is arguable that a rail tunnel fire could also present one of the more severe thermal challenges to a spent fuel transportation package. This is one of the reasons the staff chose to study the Baltimore tunnel fire event.

In examining real-world accidents that could involve a spent fuel transportation package, a number of significant differences are apparent between tunnel fires and severe fires occurring in an open (non-tunnel) environment. These factors include: 1) the possible position of a spent fuel package in relation to

[1] NUREG -0170, US Nuclear Regulatory Commission, Washington D.C., December 1977.
[2] NUREG/CR-4829, US Nuclear Regulatory Commission, Washington, D.C., February 1987.

the fire location; 2) the nature of the flammable material involved; 3) the rail bed materials; 4) the types of fires that can occur and; 5) emergency response to fire accidents.

In a fully engulfing fire, in which the fuel is generally assumed to form a pool, the most severe conditions, by definition, occur in the hottest flaming region of the fire. In a typical regulatory fire analysis (defined by the fire conditions in 10 CFR 71.73[1]), a SNF package is assumed to be located within the flaming region of the fire 3.3 ft (1 meter) above the surface of the pool. However, because many railroad tracks are elevated above grade and are constructed on porous substrate, pooling of spilled flammable liquid is less likely in an open environment when compared with a tunnel environment, where the rail bed surface is often rock, concrete, or pavement. Historically many of the fires resulting from rail accidents have involved the leakage of flammable gas (such as propane), rather than a liquid. A flammable gas cannot form a pool. If ignited, flammable gas leaking from a tank car will generally result in a localized pressure fire that is incapable of engulfing a spent fuel transportation package.

In a rail accident involving a fire, it is extremely unlikely that a spent fuel transportation package would end up directly adjacent to a tank car carrying flammable liquid. Federal regulations issued by the Department of Transportation (DOT), in 49 CFR 174.85, require very specifically defined spacing between rail cars carrying radioactive materials and hazardous materials of any kind, including flammable liquids. Typical requirements specify that a rail car carrying radioactive material must be separated from cars carrying other hazardous material by at least one buffer car. A rail car carrying a spent fuel package would not be coupled directly to a tank car carrying flammable or combustible liquid. Figure 1.1 shows an example of this arrangement in an actual radioactive material shipment by rail.

Figure 1.1. Radioactive Material Rail Shipment

[3] NUREG/CR-6672, US Nuclear Regulatory Commission, Washington D.C., March 2000.

The location of the spent fuel package relative to the fire, for a fire in an open environment (i.e., a non-tunnel fire), will determine the amount of heat absorbed by the package (assuming a direct exposure to the fire). This is because thermal radiation is the main mechanism[4] for heat transfer from the fire to the package. In an open environment, the energy imparted to the package from the fire falls off rapidly with distance from the fire. In a tunnel environment, by contrast, the fire may result in elevated temperatures on adjacent tunnel surfaces, which could result in a package being subjected to an "oven" effect due to heat radiating from hot tunnel surfaces for an extended period of time, possibly for several hours after the fire has been extinguished.

In rail accidents involving fires and hazardous materials in tank cars (including flammable gas or liquid), emergency responders follow the DOT Emergency Response Guidebook[5]. Emergency personnel are directed to provide water spray cooling to tank cars, to prevent boiling liquid expanding vapor explosions (BLEVEs) from occurring. In tunnel fires, space restrictions may make it difficult or impossible to mount an effective emergency response, either to cool tank cars or extinguish the fire. This could result in a fire burning unchecked, having a longer duration, and possibly reaching higher temperatures, compared to a fire with essentially the same fuel supply occurring in an unobstructed (non-enclosed) environment. Based on these factors, fires occurring in tunnels have the potential of being more severe than fires occurring in non-tunnel environments. The only significant limiting factor in a tunnel fire, which would not affect a fire in an open environment, is the potential for limited ventilation in a tunnel (due to tunnel length or small degree of slope), which could greatly reduce the amount of oxygen available for combustion. This would tend to reduce the burn rate, which would reduce the intensity of the fire, and thus tend to produce lower temperatures, even for a longer fire duration.

1.2 Review of Rail Transportation Accidents

As part of its investigation of the impact of the Baltimore tunnel fire on the transportation of spent nuclear fuel, NRC staff conducted a detailed survey of rail transportation accidents in the United States. The staff reviewed accident reports (particularly those of the NTSB), historical media accounts, and data from the Federal Railroad Administration (FRA) safety database, and from the Association of American Railroads (AAR). This review showed that severe rail fires, either in tunnels or open environments, are extremely infrequent events.

The staff's review revealed several facts about rail accidents in the United States in general, and those involving hazardous materials specifically. These facts, which are summarized below, aid in putting the Howard Street tunnel fire into perspective.

- In nearly 34 billion kilometers (21 billion miles) of travel on American railroads between 1975 and 2005, there have been 1700 reported incidents involving release of hazardous materials.

---

[4] For a discussion of this phenomenon see NUREG/CR-4892, *Shipping Container Response to Severe Highway and Railway Accident Conditions*, Vol. II, pages 175 to 178.

[5] 2004 Emergency Response Guidebook, U.S. Department of Transportation, Pages 115 and 128.

- Many of the 1700 incidents involved minor releases of non-flammable hazardous materials. None of the incidents reviewed involved the release of any radioactive material.

- Of the 1700 incidents, there were 8 that involved a significant quantity of flammable material and that resulted in a long duration fire. These incidents[6] were as follows:

  1) Derailment of CSXT freight train, Baltimore, Maryland, July 18, 2001 (the subject of this report)
  2) Derailment of Union Pacific Freight train, Eunice, Louisiana, May 27, 2000 [NTSB report RAR-02-03; NTIS report PB2002-916303]
  3) Derailment of Wisconsin Central freight train, Weyauwega, Wisconsin March 4, 1996[7]
  4) Derailment of BNSF freight train, Cajon Pass, California, February 1, 1996 [NTSB report RAR-96-05; NTIS report PB96-916305]
  5) Derailment of CSXT freight train, Akron, Ohio, February 26, 1989 [NTSB report HZM-90-02; NTIS report PB90-917006]
  6) Derailment of MT Rail freight train, Helena, Montana, February 2, 1989 [NTSB report RAR-89-05; NTIS report PB89-916305]
  7) Derailment of CSXT freight train, Miamisburg, OH, July 8, 1986 [NTSB report HZM-87-01; NTIS report PB-87-917004]
  8) Derailment of Illinois Gulf Central freight train, Livingston, Louisiana, September 28, 1982 [NTSB report RAR-83-05; NTIS report PB83-916305]

Of these eight accidents, only one (the Baltimore tunnel fire) occurred in a tunnel. Based on an examination of the NTSB accident reports on the seven accidents listed above that did not occur in a tunnel, the staff concluded that none of them could have provided a fully engulfing fire environment for a spent fuel package, had one been involved in the event.

This conclusion is based on three mitigating factors present in the accidents examined above: the potential proximity of a hypothetical SNF transportation package to the fire that occurred, the available fuel for the fire, and the emergency response time for each accident. These factors are expanded upon below:

(1) Proximity: Using diagrams of the rail car configurations in the seven accidents, as given in the NTSB reports, a rail car carrying a spent fuel package and its required buffer cars could not have been located close enough to any tank cars that ruptured in these accidents. An SNF package, had one been involved, would not have been positioned near enough to the burning flammable material in these accidents to be fully engulfed.

(2) Fuel for the fire: The flammable material involved in a majority of the accidents were gasses that resulted in localized pressure fires, so these accidents did not involve the pooling of

---

[6] The reports on these incidents are available on the NTSB web site, www.ntsb.gov, under the link "Accident Reports", or from the National Technical Information Service (NTIS) web site, www.ntis.gov.

[7] The NTSB did not issue a report on this accident. Information describing the accident is available in the public docket, *National Transportation Safety Board Public Docket for Railroad Accident at Weyauwega, WI, March 4, 1996*. Docket ID: 8867, Released August 18, 1997, Washington, D.C. This document is available on the website: http://www.postcrescent.com/specials/assets/APCweyauweatrain/default.htm.

flammable liquids. In those that did involve flammable liquids, pooling did not occur because of the nature of the track bed, which is elevated over porous media.

(3) Response time: The emergency response times were extremely rapid in these seven accidents (most were responded to within 1-2 hours), and response efforts included cooling the tank cars, effectively minimizing fire intensity and duration.

The Howard Street rail tunnel derailment and fire is unique in that none of the mitigating factors noted above (for non-tunnel fires) were acting to significantly limit the severity or duration of the fire. However, the staff's examination of the FRA database shows that the Howard Street tunnel derailment and fire is the only severe rail tunnel fire involving hazardous materials shipments that has occurred in the nearly 21 billion rail miles of transportation that took place in the United States between 1975 and 2005.

When this accident frequency is coupled with the expected number of shipments of radioactive material in the future, the risk of an accident of this type still remains low. In addition, several factors work to reduce the risk of this type of accident even further. These include:

(1) The intent of the Department of Energy (DOE) to ship the bulk of SNF and HLW to the Proposed Geological Repository for the Disposal of SNF and HLW at Yucca Mountain (Yucca Mountain) via dedicated rail[8];

(2) FRA consideration of enactment of regulations that would require the use of dedicated trains[9] for the shipment of SNF and HLW;

(3) AAR enacting, at the recommendation of the NRC, a "no-pass" rule[10] for single bore dual-track rail tunnels. The rule specifies that trains carrying tank cars containing hazardous materials, such as flammable or combustible liquids, and trains carrying SNF or HLW may not pass one another within the same tunnel.

This investigation has shown that accidents involving hazardous materials and long duration fires on railroads in general and in rail tunnels in particular occur with extremely low frequency. As discussed above, DOE, FRA, and AAR have taken steps to further preclude the possibility of such an accident involving SNF or HLW and other hazardous (flammable or combustible) materials in a rail tunnel. Consequently, the frequency of any rail accident involving an SNF or HLW shipment in conjunction with a long duration fire in a rail tunnel essentially approaches zero. Detailed conservative analyses of the Baltimore tunnel fire show that the potential consequences of such an accident, were it to actually occur, are minimal (as discussed in Chapter 8 of this report). The NRC staff therefore concludes that the risk to public health and safety posed by this type of transportation accident is close to nonexistent.

---

[8] Letter to Stakeholders from Paul M. Golan, Principal Deputy Director Office of Civilian Radioactive Waste Management, July 18, 2005.

[9] This consideration is mandated pursuant to Section 5105(b) of the Hazardous Materials Transportation Uniform Safety Act of 1990, As Amended.

[10] Circular No. OT-55-I (CPC-1174), American Association of Railroads, July 17, 2006.

1.3 The Baltimore Tunnel Fire Event

The Howard Street tunnel in Baltimore is a single track railroad tunnel of concrete and refractory brick. Originally constructed in 1895, later additions extended it to its current length of 1.65 mi (2.7 km). The tunnel has an average upward grade of only 0.8% from the west portal to the east portal, and at the time of the accident, the active ventilation system was not in operation. The tunnel is approximately 22 ft (6.7 m) high by 27 ft (8.2 m) wide in the vicinity of the accident; however, the dimensions vary along the length.

The freight train involved in the accident had a total of 60 cars pulled by 3 locomotives, and was carrying paper products and pulp board in boxcars as well as hydrochloric acid, liquid tripropylene[11], and other hazardous liquids in tank cars [4, 5]. As the train was passing through the tunnel, 11 of the 60 rail cars derailed. A tank car (Figure 1.2) containing approximately 28,600 gallons (108,263 liters) of liquid tripropylene had a 1.5-inch (3.81-cm) diameter hole punctured in it (Figure 1.3) by the car's brake mechanism during the derailment.

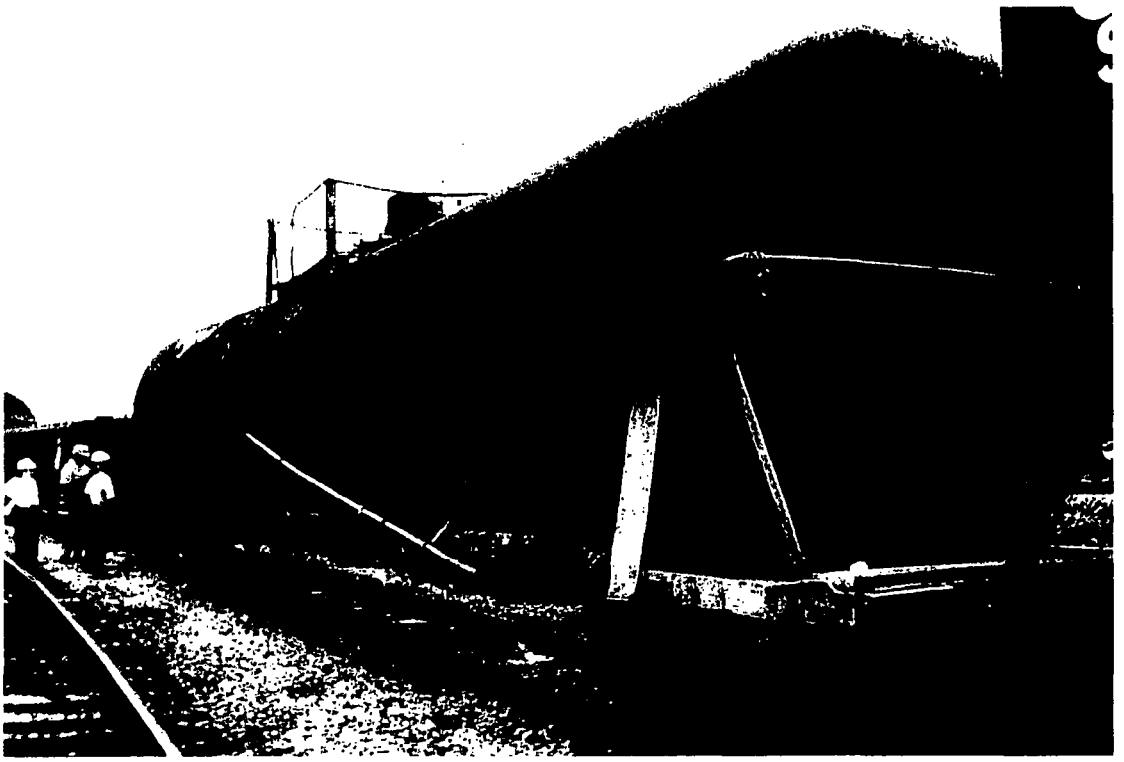

Figure 1.2. Liquid Tripropylene Tank Car

[11] Tripropylene carries an NFPA hazards rating of 3 for flammability, which is the same as that of gasoline.

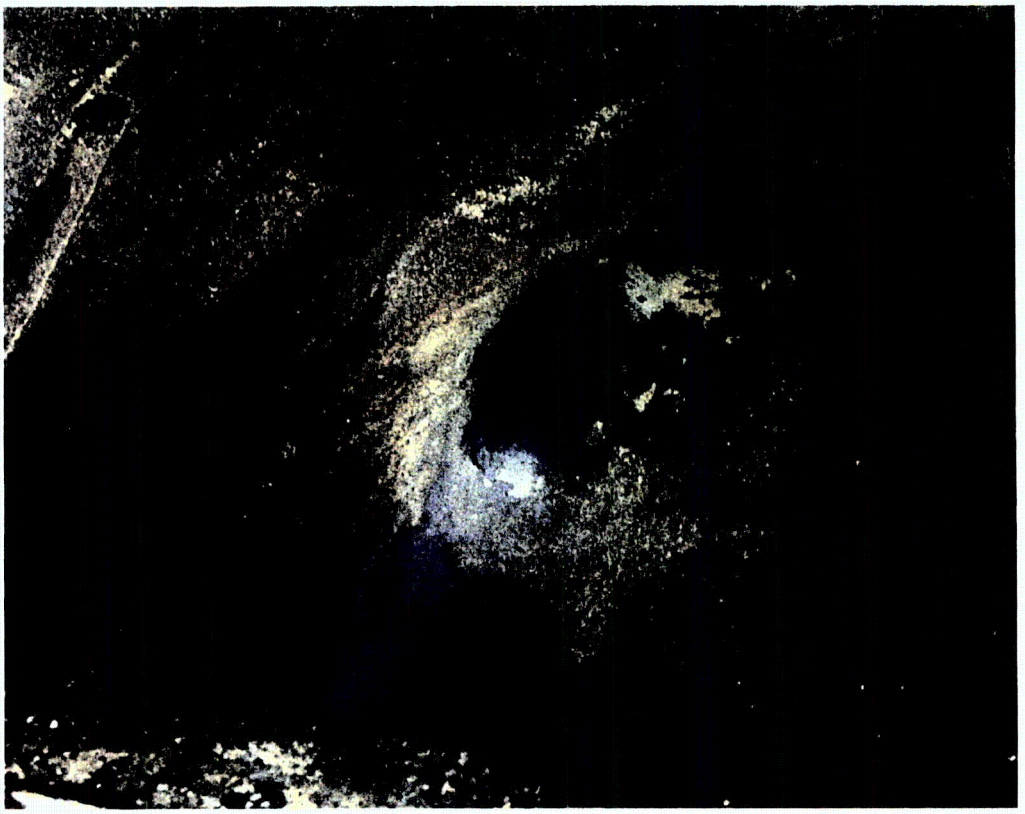

Figure 1.3. Puncture in Tank Car

Ignition of the liquid tripropylene led to the ensuing fire. The exact duration of the fire is not known with certainty. Based on NTSB interviews of emergency responders, it was determined that the most severe portion of the fire in the Howard Street tunnel lasted approximately 3 hours. Less severe fires burned in the tunnel for periods of time greater than 3 hours. Approximately 12 hours after the fire started, firefighters were able to visually confirm that the tripropylene tank car was no longer burning.

Tripropylene, which is also called Nonene, is a liquid hydrocarbon compound that is traditionally used for industrial processes. Table 1.1 lists the heat of combustion for tripropylene and a number of other hydrocarbon fuels that are commonly shipped by rail. Gasoline and jet fuel are also included in the table, but for comparison purposes only, as these fuels are rarely, if ever, transported by rail. Tripropylene has a heat of combustion comparable to that of gasoline, and has a higher heat of combustion than that of jet fuel. When compared to other common hydrocarbon liquids, tripropylene falls near the high end of the range of values for heat of combustion for hydrocarbon liquids. The range of values shown in Table 1.1 for hydrocarbon fuels is relatively narrow, however, which indicates that when burned under the same conditions, these hydrocarbon liquids will generally have similar combustion characteristics. Therefore, while tripropylene was the specific fuel for the Baltimore tunnel fire, its combustion characteristics are generally representative of the behavior of other hydrocarbon fuels.

Table 1.1. Comparison of Various Hydrocarbon Liquids

Liquid Hydrocarbons	Molecular Formula	Heat of Combustion[a] Btu/lb. (kJ/kg)
Propane	C_3H_8	19,800 (46,000)
Butane	C_4H_{10}	19,500 (45,400)
Isobutane	C_4H_{10}	19,600 (45,600)
Pentane	C_5H_{12}	19,300 (45,000)
Hexane	C_6H_{14}	19,200 (44,700)
Heptane	C_7H_{16}	19,200 (44,700)
Toluene	C_7H_8	17,400 (40,500)
Octane	C_8H_{18}	19,100 (44,400)
Nonane	C_9H_{20}	19,000 (44,300)
Nonene (tripropylene)	**C_9H_{18}**	**19, 000 (44,300)**
Decane	$C_{10}H_{22}$	19,000 (44,300)
Undecane	$C_{11}H_{24}$	19,000 (44,300)
Gasoline (mixture of heptanes, octanes, nonanes and decanes)	C_8H_{15}[b]	19,100 (44,500)[b]
Jet Fuel, grade JP-1		18,500 (43,000)
Jet Fuel, grade JP-2		18,700 (43,500)
Jet Fuel, grade JP-3		18,700 (43,500)
Jet Fuel, grade JP-4		18,500 (43,000)

[a]Values derived from Perry, Chilton, and Kirkpatrick, *Perry's Chemical Engineer's Handbook*, 4th Edition, Table 3-202, Page 3-104.
[b]Typical values. Values will vary slightly depending on formulation. Derived from Ferguson and Kirkpatrick, *Internal Combustion Engines, Applied Thermosciences*, 2nd Edition, Page 316 and Table 10.8.

1.4 Implications of the Baltimore Tunnel Fire for Transportation of Spent Nuclear Fuel

As one element of the evaluations related to the Baltimore tunnel fire accident, calculations were performed by NRC for three currently licensed spent nuclear fuel transportation packages. This analysis is a case study of a historic event, with the addition of the involvement of a spent nuclear fuel transportation package and a conservative representation of the possible fire duration. The staff's efforts were focused on providing a realistic transportation accident scenario based on the physical conditions of

the Howard Street tunnel and the actual events surrounding the derailment and ensuing fire. The analysis is not intended to determine a "worst case" tunnel fire accident involving spent nuclear fuel. However, given the extremely low frequency of this type of accident (as discussed in Section 1.2), and the intensity and duration of the fire, this accident imposes extremely severe conditions on an SNF package, and constitutes a 'beyond design-basis' scenario.

This analysis evaluated the performance of the TransNuclear Model No. TN-68 ("TN-68"), the HOLTEC International Model No. HI-STAR 100 ("HI-STAR 100"), and the NAC International Model No. LWT ("NAC LWT") transport packages when subjected to boundary conditions representing the Baltimore tunnel fire. Tunnel air, wall, floor, and ceiling temperatures obtained from fire analyses performed by the National Institute of Standards and Technology (NIST), were used to define the boundary conditions for the transient calculations. The purpose of the evaluation was to obtain an estimate of the temperature response of the various components of each of these packages during and after the fire.

This report presents general descriptions of the transportation package designs analyzed, as well as a detailed description of the analyses conducted including modeling approach, boundary conditions, and computational results. Section 2 describes the NIST tunnel fire model used to develop boundary conditions for the thermal analyses of the spent fuel transportation packages. Section 3 briefly describes the material exposure analysis used to verify the predicted temperatures obtained in the fire simulations performed by NIST. Section 4 presents a detailed description of the spent fuel transportation packages evaluated. The computational models developed for the analyses are described in Section 5. Section 6 presents a detailed description of the analysis method. Section 7 presents the results of the simulation, giving a detailed evaluation of the predicted response for each transportation package during and after the fire. Section 8 provides an analysis to determine the magnitude of any potential radiation hazard or release of radioactive material as a consequence of the effects of the fire on each of the packages.

2 NIST TUNNEL FIRE MODEL

Experts at the National Institute of Standards and Technology (NIST) developed a model [4] of the Baltimore tunnel fire using the Fire Dynamics Simulator (FDS) code [6, 7][12] to assess the thermal environment within the tunnel during the fire. The NIST study was based on information developed by the NTSB investigation of the tunnel fire, including descriptions of the tunnel structural features, the damage to the rail cars, and the sequence of events in the accident. Using this information as the starting point for the calculations, the analysis was extended to include variation of the unknown parameters to predict the range and distribution of temperatures that could have been sustained in the tunnel during and after the fire, and the duration of the fire.

FDS is a computational fluid dynamics (CFD) code that models combustion and flow of hot gas in fire environments. FDS solves the mass, momentum, and energy equations for a given computational grid, and uses a large eddy simulation technique to represent turbulence effects. The source term representing the fire is modeled by solving an additional transport equation for a conserved scalar quantity representing the mixture fraction of fuel and oxygen. Thermal radiation is modeled with the radiative transport equation for a non-scattering grey gas. The code is also able to construct a visual representation of smoke flow in a fire, taking into account the effects of the geometry of the fire environment and the material comprising surrounding structures.

The extensive validation of FDS includes comparisons to results of tunnel fire tests with conditions similar to the Baltimore tunnel fire. NIST developed fire models using FDS based on the geometry and test conditions from a series of tunnel fire experiments conducted by the Federal Highway Administration and Parsons Brinkerhoff, Inc. as part of the Memorial Tunnel Fire Ventilation Test Program [8]. NIST modeled both a 6.83×10^7 Btu/hr (20 MW) and a 1.71×10^8 Btu/hr (50 MW) unventilated fire test from the Memorial Tunnel Test Program, and achieved results using FDS that were within 100°F (56°C) of the recorded data[6,7].

The full-length, 3-dimensional representation of the Howard Street tunnel developed by NIST included the rail cars represented as solid blocks elevated 3.3 ft (1 m) above the rail bed. The rail car blocks can absorb thermal radiation, and provide obstructions to air flow in the tunnel. In the model, the blocks representing the rail cars were positioned in the center of the tunnel for the majority of the calculations. However, sensitivity studies included calculations performed with the rail cars modeled in their derailed positions in the tunnel, as documented by the NTSB. The source of the fire was specified in the simulation as a pool of burning liquid tripropylene[13] positioned below the location of the hole that was punctured in the tripropylene tank car during the derailment. The computational grid for the tunnel fire model was relatively fine in the immediate vicinity of the fire, with nodes on the order of 6 to 12 inches

[12] Formal publication of the FDS code documentation began in 2001 with Version 2. Continuing validation and development of the code led to Version 3 in 2002. Version 3 was used in the FDS analyses discussed in this report.

[13] Combustible materials in nearby box cars ignited during the fire, and continued to smolder for several days, long after the tripropylene fire self-extinguished. However, these materials contributed relatively little energy to the fire, and burned at temperatures far lower than those experienced during the flaming combustion of the liquid hydrocarbon fuel.

(0.15 to 0.30 m) in length, in order to properly capture fire and gas behavior. The mesh size was expanded at distances farther from the fire source, where less resolution was needed. The entire tunnel volume was included in the FDS calculation, in order to appropriately simulate the mixing of air and hot gasses along the full length of the tunnel.

Parametric studies of the burning rate of the fire based on the amount of available fuel, the air flow in the tunnel, the thermal conductivity of the bricks lining the tunnel, and sensitivity studies on the fuel pool area show that the Howard Street tunnel fire was oxygen-limited. In the confined space of the tunnel, the heat release rate of the fire was constrained by the supply of oxygen, rather than the supply of fuel. For a wide range of modeling assumptions, the overall heat release rate (or heat rate) for the fire was predicted to be no more than about 1.71×10^8 Btu/hr (50 MW). The highest peak temperatures predicted in these simulations were 1832-2012°F (1000-1100°C) in the flaming region of the fire. The calculational results showed that the hot gas layer above the rail cars within three to four rail car lengths of the fire was an average of 932°F (500°C). Peak temperatures on the tunnel surfaces were calculated to reach 1472°F (800°C) where flames directly impinged on the ceiling of the tunnel. The average tunnel ceiling temperature within a distance of three to four rail car lengths from the fire was calculated to be 752°F (400°C).

In these FDS simulations, the hottest temperatures occur within the first hour of the fire. After that point, the fire is oxygen-limited and temperatures are generally lower. A considerable fraction of the evaporated fuel does not burn due to lack of oxygen, and instead is predicted to have been carried out of the tunnel with the smoke and other combustion gases. However, these simulations extended only over the first 3 hours of the fire. At that point, the bursting of a water main within the tunnel introduced significant uncertainty in the boundary conditions for the fire within the tunnel. The presence of water in the tunnel would be expected to affect the fire intensity and possibly duration, but there is no means of determining how much water might have actually reached the fire location. The tripropylene fire probably burned more than 3 hours, but it could have done so only at a reduced rate due to lack of sufficient oxygen and it may also have been affected by cooling or quenching due to the presence of water in the tunnel. Within 12 hours, the fire had self-extinguished due to oxygen starvation and possibly water quenching.

Additional FDS simulations were performed using the same model of the Howard Street tunnel, to investigate possible scenarios that could produce long-duration, high-temperature fires within the tunnel environment. In these simulations, the bursting of the water main was ignored, the tunnel was assumed to be ventilated in a manner that allowed the fire to be fully oxygenated, and the fire was assumed to burn until the entire inventory of fuel in the tank car was consumed by combustion. (This assumes that no fuel was lost due to evaporation or by draining away from the fire location or by soaking into the rail bed.) The cross-sectional area of the pool of fuel was assumed to be no more than 600 ft^2 (56 m^2), corresponding to the footprint of the tank car, which is about the smallest pool that could have been sustained within the tunnel. This essentially supposes that the fuel was confined within the low "walls" formed by the rails of the track, that the tank car was fortuitously situated at a slight dip in the rail bed, and the fuel spilled from the puncture in the tank car at a rate that did not overflow this shallow pan before it could be consumed by the fire. Although somewhat unrealistic, these assumptions led to a more conservative fire duration.

This minimum size for the fuel pool was assumed in order to determine the hottest and longest-lasting potential fire conditions for this event. A larger pool size would generally mean a shorter duration for the fire (because a fire burning over a larger area consumes fuel more rapidly) and the possibility of a lower peak temperature (due to the formation of an oxygen starved "core" at the interior of the pool area). The assumed pool size is very conservative for this scenario, since it is reasonable to assume that the fuel spilled freely through the rail bed and along the floor of the Howard Street tunnel and, therefore, would have burned over a larger area and at lower temperatures than were calculated for the assumed minimal fuel pool size in the FDS calculation.

If the tunnel ventilation system had been operating at the time of the fire, air flow to the fire would have been higher, and the fire would not have been oxygen-starved to the same extent as it was with the ventilation system off. To allow sufficient ventilation within the tunnel for all of the fuel to be consumed by combustion, the FDS model was modified to include holes in the tunnel walls that connected to the ambient environment. Assuming 53.84-ft^2 (5-m^2) holes (3.3 ft (1 m) high by 16.4 ft (5 m) wide, 9.8 ft (3 m) above the tunnel floor), every 328 ft (100 m) along one side of the tunnel produced a fire lasting 6.7 hrs. The peak gas temperatures in this scenario were 2084°F (1140°C) in the flaming region of the fire and 1958°F (1070°C) at 66 ft (20 m) downstream of the fire. At the location 66 ft (20 m) downstream of the fire, peak ceiling temperatures above 1832°F (1000°C) were predicted from about 3 hours until the end of the fire at 6.7 hrs.

The heat rate for the fire in this scenario is approximately 1.71×10^9 Btu/hr (500 MW), which is an order of magnitude higher than the heat rate predicted for the actual fire. The scenario conservatively assumes a sufficient supply of oxygen for the fire (as if the tunnel had been well ventilated) and a minimum credible fuel pool area within the confines of the tunnel. These assumptions produced a fire scenario within the tunnel that is comparable in severity to an open pool fire, and is arguably the most severe fire that could possibly have occurred with the available fuel. The temperatures predicted with FDS for this scenario provided the fire boundary conditions for the ANSYS and COBRA-SFS simulations in the current study. (See Section 6.1 for a complete description of the actual boundary conditions used.)

3 CNWRA MATERIALS FIRE EXPOSURE ANALYSIS

Staff from the Center for Nuclear Waste Regulatory Analysis (CNWRA), along with staff from NRC and NIST, examined rail cars and the tank car removed from the Howard Street tunnel, to evaluate evidence of high temperatures experienced by these components. The examination of physical evidence provided the staff with further insight into the fire environment that existed in the tunnel during the accident. Staff from CNWRA also collected material samples from these boxcars and the tank car for further analysis.

By performing metallurgical analyses on the material samples collected, including sections of the boxcars exposed to the most severe portion of the fire and an air brake valve from the tripropylene tank car, CNWRA was able to estimate the fire exposure time and temperature for the samples tested. These analyses indicated that material temperatures on the roof of the boxcar located approximately 66 ft (20 m) from the tank car were in the range of 1382-1562°F (750-850°C) for approximately 4 hours. Material temperatures on other components of this boxcar were estimated to have reached values on the order of 1112°F (600°C). (Additional details associated with the analyses performed by CNWRA can be found in the report on the analysis of the rail car components [5].)

The material time and temperature exposures determined by the CNWRA analyses provide objective verification of the detailed predictions of the NIST FDS model of the Howard Street tunnel fire [4]. The FDS calculations predict peak gas temperatures of 1832-2012°F (1000-1100°C) in the flaming region of the fire, with peak surface temperatures of 1472°F (800°C) on the tunnel ceiling. Because of the insulation provided by the brick walls of the tunnel, the calculated temperatures within 3 to 4 rail car lengths (within approximately 200 ft (60 m)) of the fire were relatively uniform, as in an oven or furnace. As a result, the hot gas layer above the rail cars in this region is calculated to sustain an *average* temperature of approximately 932°F (500°C) for at least 3 hours. The local material temperatures estimated in the CNWRA analysis at 66 ft (20 m) from the fire could easily have been sustained in this predicted fire environment.

The fire scenario used to define the boundary conditions for the ANSYS and COBRA-SFS calculations in the current study, however, represents conditions that are more severe than the conditions predicted with FDS using realistic boundary conditions based on available information about the Howard Street tunnel fire. In this scenario, as described in Section 2, the fire is assumed to be fully ventilated and burns for nearly 7 hours, until all of the tripropylene fuel is consumed. The FDS simulation using these assumptions predicts peak gas temperatures above 1400°F (760°C) for more than 5 hours in the region 66 ft (20 m) from the fire center. The peak ceiling temperature at this location is above 1400°F (760°C) for more than 6 hours. This fire environment would result in far more severe conditions at the hypothetical location of an SNF package than are indicated for the actual Baltimore tunnel fire by the results of the CNWRA materials analyses.

4 TRANSPORTATION PACKAGES ANALYZED

As discussed in Section 1, NRC regulations require that spent fuel transportation packages be evaluated for a series of hypothetical accident conditions that include a 30-ft (9 m) drop test, a 40-inch (1 m) pin puncture drop test, and a fully engulfing fire with an average flame temperature of 1472°F (800°C) for a period of 30 minutes. These tests are followed by the immersion of an undamaged package under 50 ft (15 m) of water [1]. The certification process must include either an open pool fire test or an analysis of the package for a fire exposure meeting the aforementioned criteria. Packages must maintain shielding and criticality control functions throughout the hypothetical accident conditions.

This investigation evaluated how a fire similar to the Howard Street tunnel fire might affect three NRC-certified spent fuel transportation package designs. These included the TransNuclear TN-68 and HOLTEC HI-STAR 100 rail transportation packages, and the NAC LWT transportation package. The LWT was selected because it represents a typical truck (over-the-road) package that can also be transported by rail. The design of each of these packages is briefly described in the following sections.

4.1 TransNuclear TN-68 SNF Transportation Package

The TN-68 spent fuel shipping package transports BWR spent fuel assemblies. The basic design is similar to that of the HOLTEC HI-STAR 100, except that the TN-68 package does not include an inner seal-welded canister. The containment boundary is provided by the package shell and lid seals. The TN-68 package holds up to 68 BWR assemblies, with a maximum total decay heat load of 72,334 Btu/hr (21.2 kW). The fuel assemblies are contained within a basket structure consisting of 68 stainless steel tubes that have aluminum and borated aluminum (or boron carbide/aluminum composite) neutron poison plates sandwiched between the steel tubes. The general layout of the TN-68 package is illustrated in Figures 4.1 and 4.2. Detailed information on the design can be found in the appropriate sections of the TN-68 Safety Analysis Report (SAR) [9].

The basket structure is supported by aluminum alloy support rails bolted to the inner carbon steel package shell, which also serves as the inner gamma shield. This inner steel shell is shrink-fitted within an outer carbon steel shell that serves as the outer gamma shield. The gamma shielding is surrounded by the neutron shielding, which consists of a ring of aluminum boxes filled with borated polyester resin. The outer shell of the package is carbon steel.

The package bottom is carbon steel with an inner steel shield plate. The package lid is also carbon steel with a steel inner top shield plate. During transport, the ends of the package are capped with impact limiters made of redwood and balsa and covered in stainless steel plate (depicted in Figure 4.2). The TN-68 weighs approximately 260,400 lb (118,115 kg) when loaded for transport.

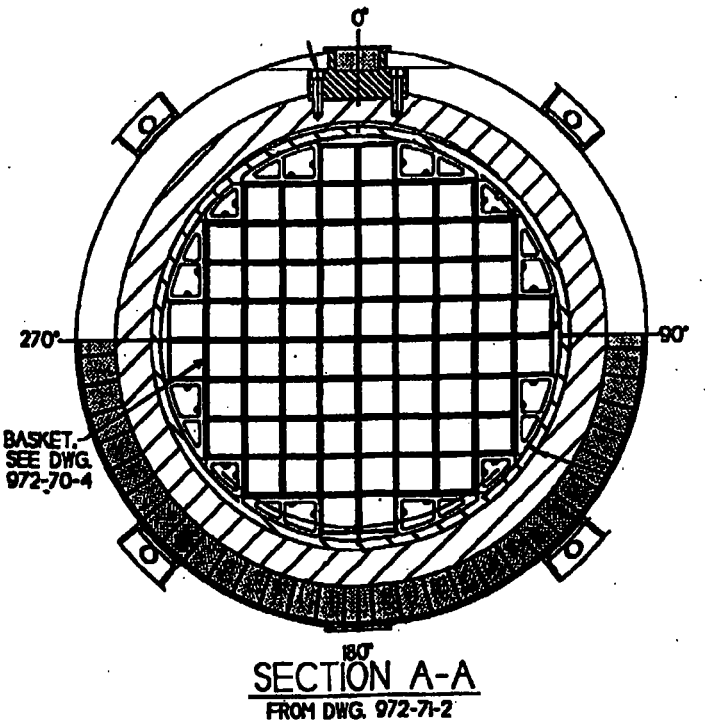

Figure 4.1. Cross-section of TN-68 Package (drawing 972-71-3 Rev. 4, "TN-68 Packaging General Arrangement: Parts List and Details")

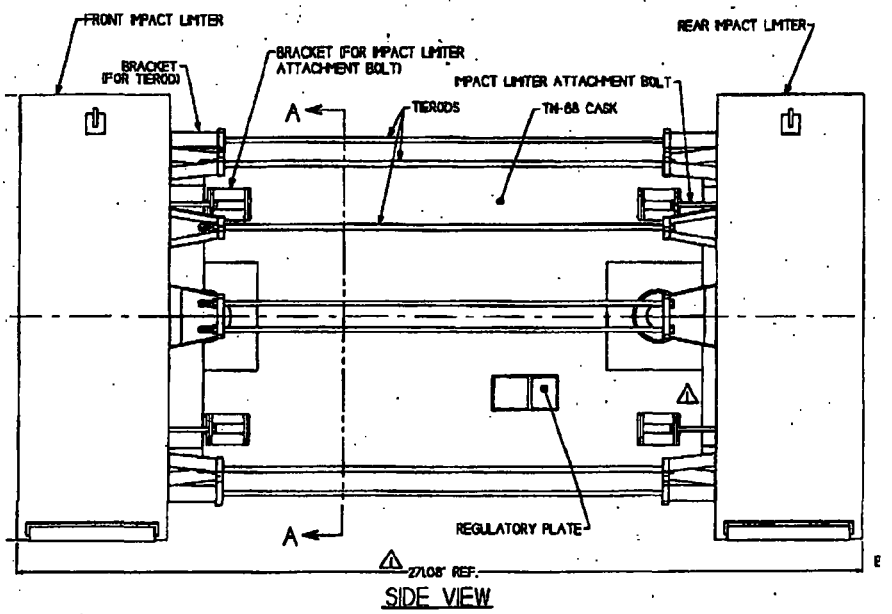

Figure 4.2. TransNuclear TN-68 Spent Fuel Transportation Package

4.2 HOLTEC HI-STAR 100 SNF Transportation Package

This design provides an additional containment boundary in the form of a welded multi-purpose canister (MPC) enclosing the spent fuel. (The outermost containment boundary is provided by the package shell and lid seals.) HOLTEC has MPC designs to accommodate three different spent fuel loading configurations: up to 24 PWR assemblies, up to 32 PWR assemblies, or up to 68 BWR assemblies. The MPC-24 was selected for this evaluation. This design has an integral fuel basket that accommodates 24 PWR spent fuel assemblies with a maximum total decay heat load of 68,240 Btu/hr (20 kW). The MPC is placed in the transportation packaging for shipment after it has been loaded with spent nuclear fuel and welded shut. A diagram of the HI-STAR 100 package system is provided in Figure 4.3. The package inner shell is stainless steel, and six layers of carbon steel plates comprise the gamma shield. The next layer is a polymeric neutron shield, strengthened by a network of carbon steel stiffening fins. The outer shell of the package is carbon steel, with a painted surface.

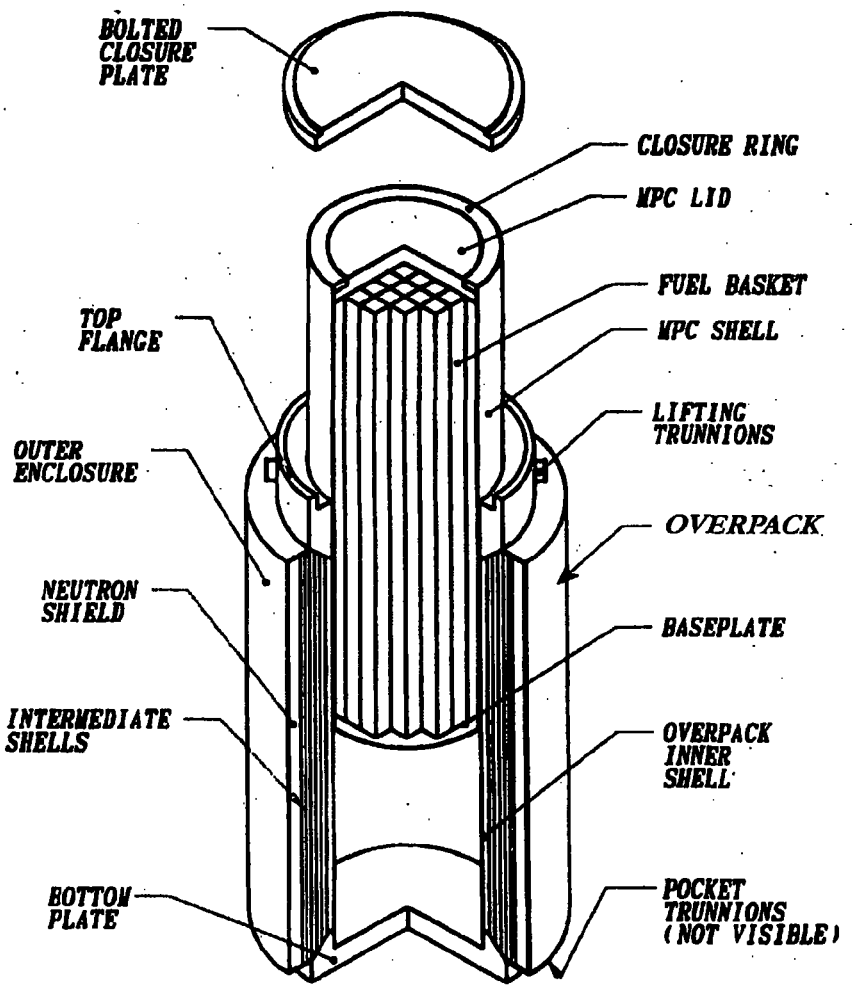

Figure 4.3. HOLTEC HI-STAR 100 Spent Fuel Package

Aluminum honeycomb impact limiters with stainless steel skin are installed on the ends of the package prior to shipping. Impact limiters protect the closure lid, MPC, fuel basket, and contents from damage in the event of a package drop accident. The impact limiters also provide thermal insulation to the lid and port cover components in the event of a fire exposure. Figure 4.4 shows an illustration of this package secured to a rail car, with impact limiters installed. This package weighs approximately 277,300 lb (125,781 kg) when loaded for transport. Additional configuration details are provided in the HI-STAR 100 Package System SAR [10].

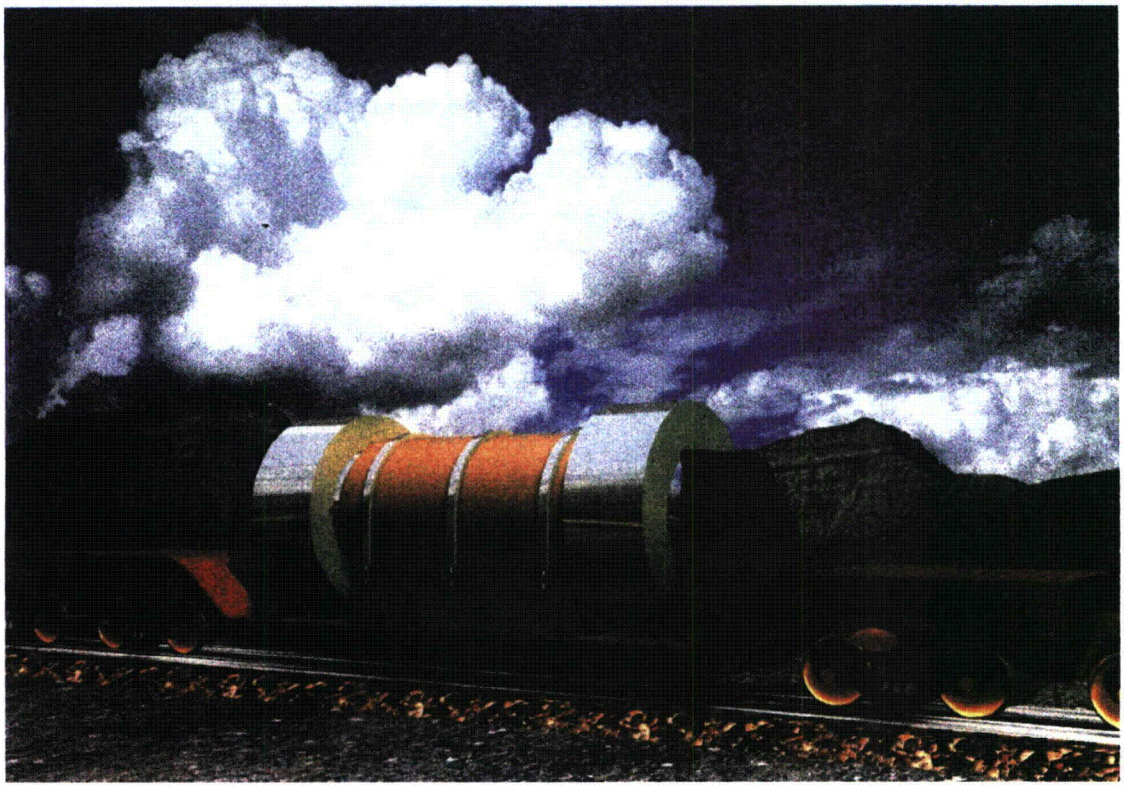

Figure 4.4. Spent Fuel Transportation Package on Rail car[14]

4.3 NAC LWT SNF Transportation Package

The NAC LWT is a small transportation package certified for transport on a standard tractor trailer truck, which can also be transported by rail. The NAC LWT is typically enclosed within an International Organization for Standardization (ISO) shipping container when shipped by rail. The Certificate of Compliance (CoC) for this SNF package requires that it be enclosed in either a personnel barrier (PB) or ISO container. Figure 4.5 shows a picture of a NAC LWT package on a flat-bed trailer with a PB installed, but without an ISO container.

[14] Image courtesy of HOLTEC International.

PBs commonly used for truck shipments are not suitable for rail shipments, so an ISO container would generally be required. Current DOE policy requires an ISO for truck packages shipped by rail, and every rail shipment of the LWT to date has been in an ISO container. Figure 4.6 shows an exterior view of the package within an ISO container on a flat-bed trailer.

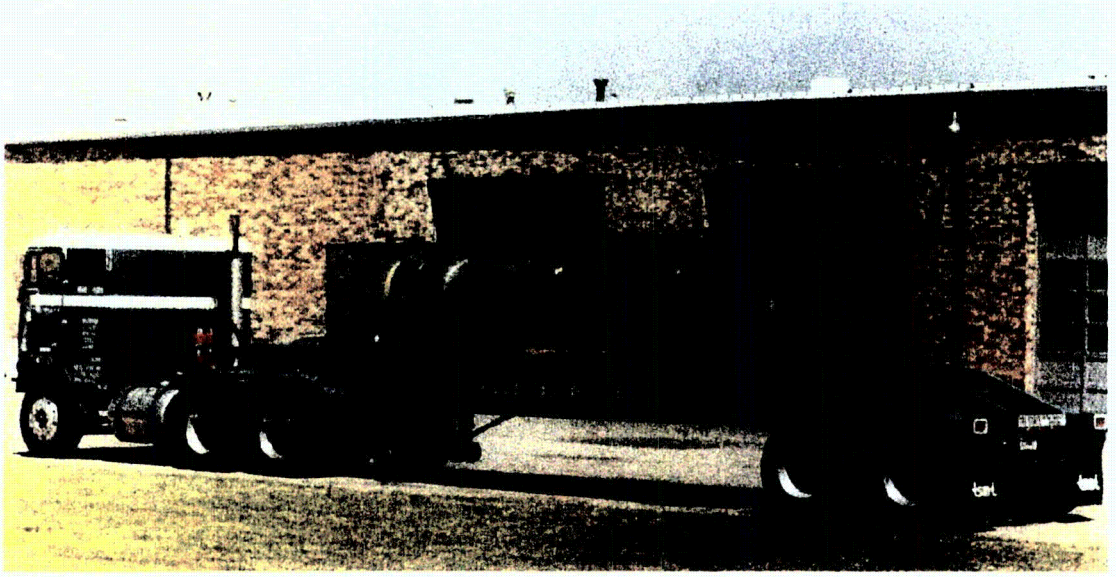

Figure 4.5. NAC LWT Transport Package (without ISO container)

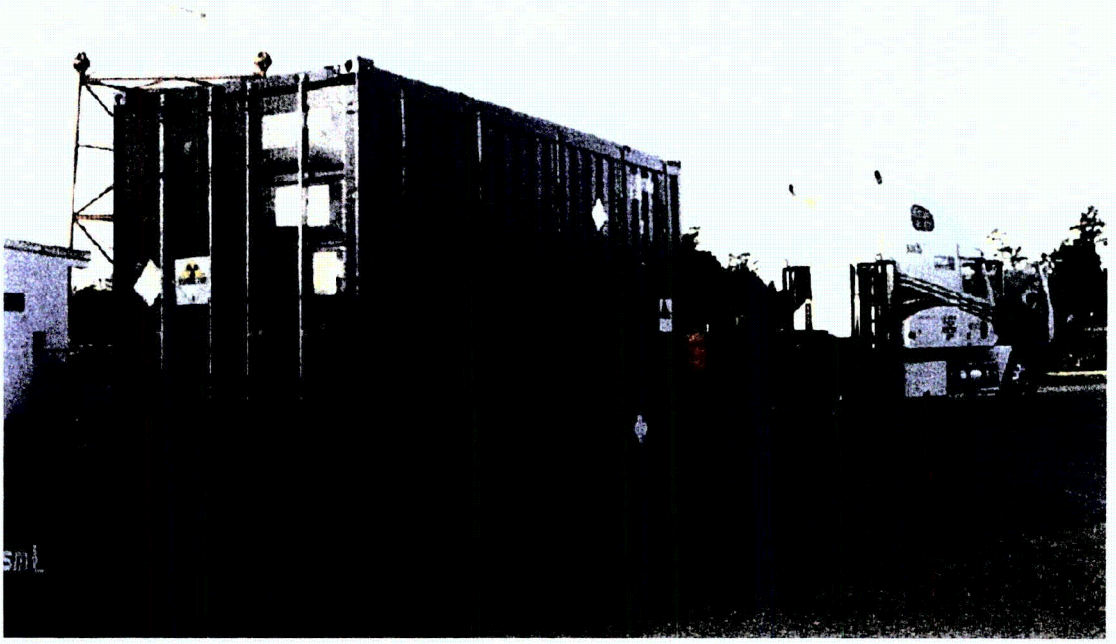

Figure 4.6. NAC LWT Transport Package (within ISO container)

This package is designed to transport a variety of commercial and test reactor fuel types with widely varying maximum decay heat load specifications for the different fuels. For the purpose of this analysis, the package was assumed to contain a single PWR spent nuclear fuel assembly, with a maximum decay heat load of 8,530 Btu/hr (2.5 kW). This fuel configuration and maximum decay heat load is used for the thermal evaluation of the package presented in the SAR [11], and provides a conservative thermal load for the fire accident scenario.

The loaded package weighs approximately 52,000 lb (23,586 kg). The containment boundary provided by the stainless steel package consists of a bottom plate, outer shell, upper ring forging, and closure lid. The package has an additional outer stainless steel shell to protect the containment shell, and also to enclose the lead gamma shield. Neutron shielding is provided by a stainless steel neutron shield tank containing a water/ethylene glycol mixture. An additional annular expansion tank for the mixture is provided, external to the shield tank. This component is strengthened internally by a network of stainless steel stiffeners. Aluminum honeycomb impact limiters covered with an aluminum skin are attached to each end of the package. Additional configuration details are provided in the SAR for this transport package [11].

5 ANALYSIS APPROACH

The analytical approach chosen to evaluate the response of the selected transportation packages was to construct highly detailed analysis models capable of accounting for all the significant heat transfer paths to and from the package by means of conduction, convection, and thermal radiation. All three transportation package models were constructed in parallel to expedite the evaluation. Two different computer analysis codes were used for the large multi-assembly packages, to provide independent verification of the analytical approach. The TN-68 package was modeled using the COBRA-SFS finite-difference thermal-hydraulic analysis code [2]. The HI-STAR 100 and NAC LWT packages were modeled using the ANSYS [3] general purpose FEA code. Three-dimensional (3D) models of each of the packages were developed for these analyses. These models were subjected to boundary conditions (see Section 6) derived from a detailed simulation of the Howard Street tunnel thermal environment during and after the fire, performed with the FDS code. (See Section 2 for a discussion of the NIST analysis of the Howard Street tunnel fire and the selected fire scenario for these analyses.)

Section 5.1 presents a general description of the representation of the SNF packages within the tunnel environment. Section 5.2 contains a detailed description of the COBRA-SFS model of the TN-68 package. The ANSYS model of the HI-Star 100 is described in Section 5.3, and Section 5.4 contains a description of the ANSYS model of the NAC LWT.

5.1 Modeling SNF Packages within Tunnel

Boundary conditions for the models of the SNF packages were taken from the results of the FDS analysis at 66 ft (20 m) down stream of the fire source. This location was determined from the configuration of the rail cars within the tunnel relative to the fire, as shown in Figure 5.1. The selected location corresponds to the shortest possible distance between the tank car carrying liquid tripropylene and the nearest rail car that could have been carrying an SNF package on this particular train.

Other possible derailment configurations were examined by the staff, based on behavior commonly exhibited by rail cars that have derailed. Figure 5.2 depicts a common derailment scenario involving a single bore tunnel where the distance between the side walls is twice the width of a rail car. As can be seen from the diagram, a derailment that results in a decoupling of the rail cars and an "accordion" placement of the rail cars would actually move the cars further apart than an in-line derailment of the type that occurred in the Howard Street tunnel.

The assumed location of the SNF package in this analysis is based on Department of Transportation regulations that require rail cars carrying radioactive materials to be separated from other cars carrying hazardous materials or flammable liquids by at least one innocuous rail car (referred to as a buffer car) [12]. The dimensions of the Howard Street tunnel (depicted in Figure 5.3) would not have allowed a rail car carrying an SNF package to come any closer to the tripropylene tank car. Even if the buffer car is assumed to be a flat rail car, it would be essentially impossible, given the velocity of the train at the time of the derailment, for the buffer car to slide past either the tripropylene tank car or a rail car carrying a SNF package, and thereby decrease the distance between the SNF transportation package and the fire.

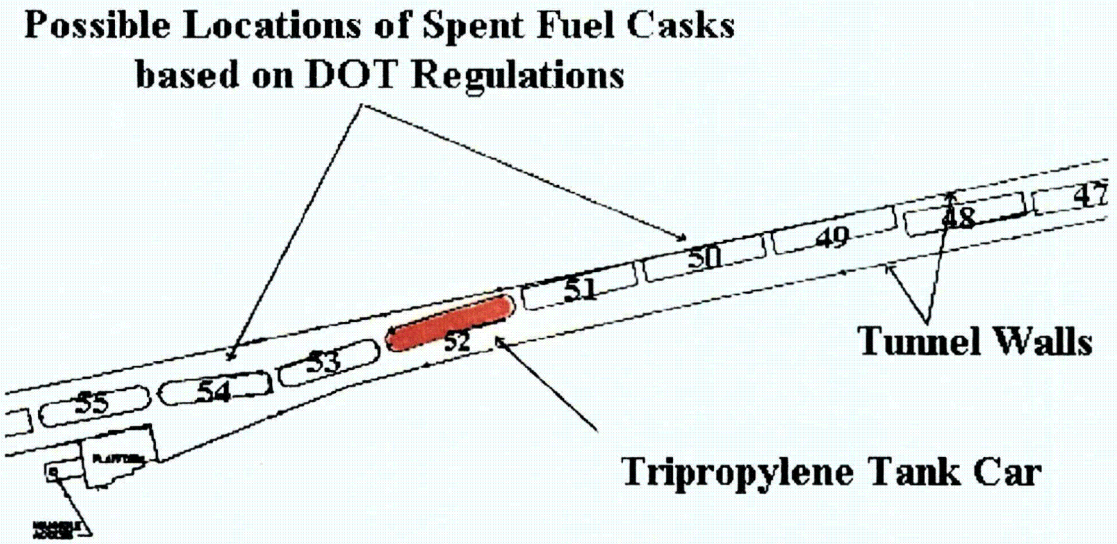

Figure 5.1. Configuration of Derailed Train in Vicinity of Fire

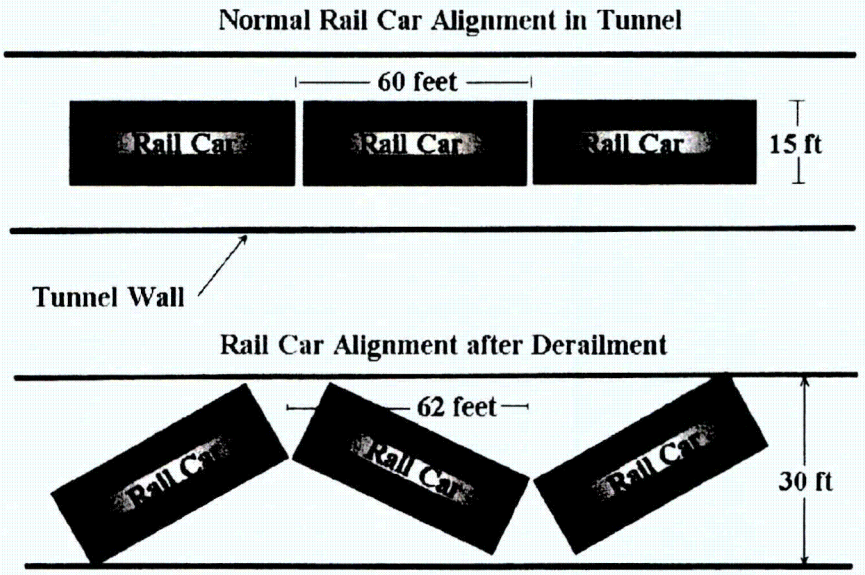

Figure 5.2. Possible Orientation of Derailed Train in Tunnel

The package was assumed to remain on the rail car in a horizontal position with one end of the package facing the fire source. This orientation results in maximum possible exposure to the fire-driven flow of hot gas along the length of the package, and is the most adverse position for free convection cooling of the package during the post-fire cool down. It also results in the maximum exposure of package surfaces to tunnel surfaces for thermal radiation exchange. This is a particularly important consideration, since radiation heat transfer to the package is the most significant mode of heat transfer during and immediately following the fire, by at least an order of magnitude.

Alternative orientations for the SNF package in this accident scenario, however plausible, would result in less severe boundary conditions during the fire transient. A vertical orientation for the package on the rail car would result in decreased exposure to the fire-driven flow of hot gas around the package and enhanced free convection cooling during the post-fire cool down phase of the transient. This orientation would also result in a decrease in thermal radiation interaction with the tunnel surfaces, due to attenuated view factors. In particular, the axial length of the package would not have the direct (essentially parallel) view of the tunnel ceiling that it has on its upper side in the horizontal orientation.

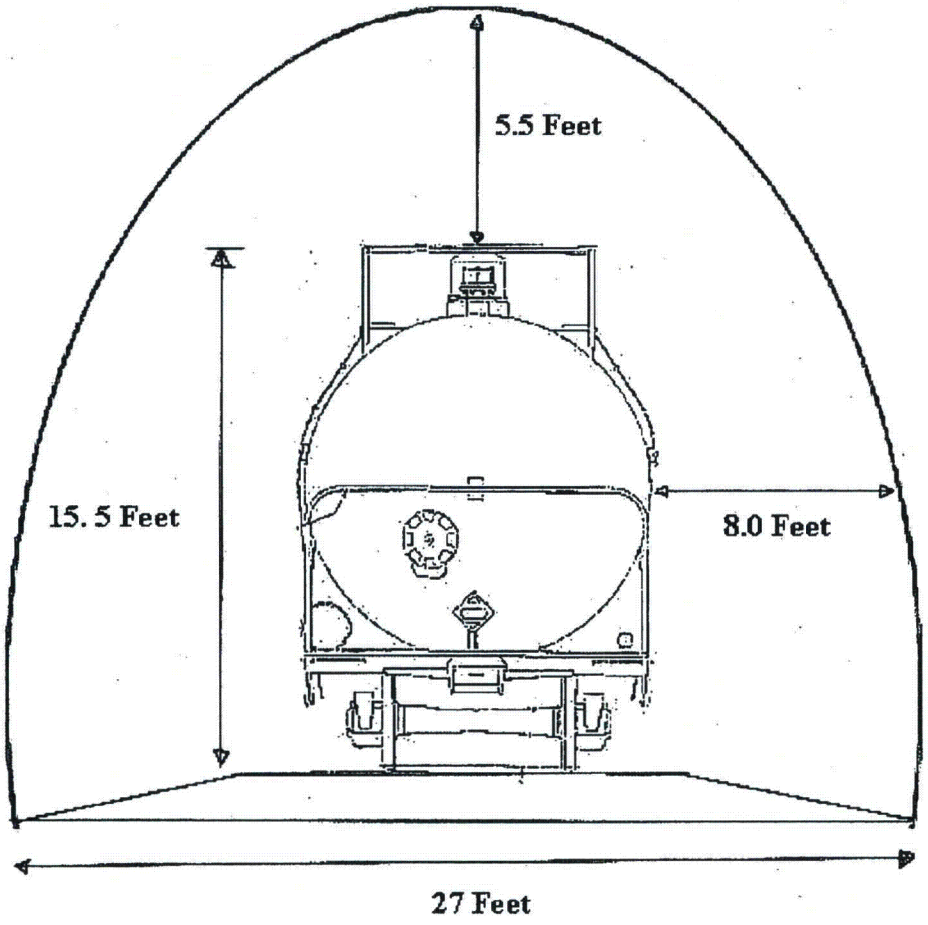

Figure 5.3. Dimensions of Howard Street Tunnel with Tank Car on Track

Postulating that the SNF package would separate from the rail car would also result in less severe boundary conditions on the package, even assuming that the package ended up closer to the fire. In such a scenario, the package would be on the floor of the tunnel, exposed to markedly lower temperatures from the surrounding air and tunnel surfaces, compared to the boundary conditions encountered at the elevation of the package on the rail car at 66 ft (20 m) down-stream of the fire. This position would also tend to attenuate thermal radiation interaction with the hottest surfaces in the tunnel (i.e., the ceiling and upper side walls).

As discussed in Section 2, the FDS simulation used to define the boundary conditions for this analysis modeled a hypothetical fire scenario with greatly enhanced ventilation, in order to fully consume the available fuel supply at a fully oxygenated burn rate, and a minimal fuel pool size, in order to achieve the highest possible fire temperatures. This extremely conservative scenario resulted in a fire lasting approximately 7 hours, with increasing temperatures at the assumed location of the SNF package in the tunnel for the entire fire duration. In the FDS analysis, the calculation was extended out to a 23-hour post-fire cool down, for a total simulation time of 30 hours. To determine the packages' complete transient temperature responses, and to explore the effects of prolonged exposure to post-fire conditions in the tunnel, the COBRA-SFS and ANSYS analyses further extended the post-fire duration to 300 hours. Tunnel wall and air temperatures predicted in the FDS analysis at 30 hours were extrapolated from 30 hours to 300 hours using a power function, to realistically model cool-down of the tunnel environment.

The FDS analysis utilized a fine-mesh noding that yielded detailed predictions of axial and radial distributions of tunnel air temperatures, gas velocities, and tunnel surface temperatures throughout the fire and post-fire cool down period. As a conservative approach to defining the thermal environment seen by the SNF packages during the fire, the peak air temperatures predicted in the FDS simulation in the top, middle, and bottom regions of the tunnel were used to define the boundary conditions around the corresponding regions on the circumference of the package during the transient. These temperatures were used to define the local ambient temperatures for convection heat transfer from the surfaces of the packages. Similarly, the peak tunnel surface temperatures on the ceiling, side walls, and floor were used to define the surface temperature boundary conditions for radiation exchange.

This conservative simplification of the detailed FDS results describing the tunnel thermal environment was implemented by dividing the tunnel cross-section into three regions, as illustrated in Figure 5.4. (This figure is a conceptual diagram, not a scale drawing; proportions have been distorted to permit labeling of boundary regions.) For the air temperature boundary conditions for convection at the package surface, the "bottom" region was defined as extending from the tunnel floor to 1 ft (0.3 m) above the floor. The "side" region was defined as extending from 1 ft (0.3 m) to 15.8 ft (4.8 m) above the tunnel floor. The "top" region was defined as extending from 15.8 ft (4.8 m) above the tunnel floor to the tunnel ceiling at 22 ft (6.7 m). Similarly, for the wall temperature boundary conditions for radiation exchange, the "bottom" region was defined as the tunnel floor; the "side" region was defined as the tunnel wall extending to 15.8 ft (4.8 m) above the tunnel floor. The "top" region included the arch of the tunnel ceiling down to 15.8 ft (4.8 m) above the tunnel floor.

The diagram in Figure 5.4 illustrates the coupling of the external thermal environment to the top, side, and bottom regions of the SNF package model, as implemented for the HI-STAR 100. For the NAC LWT,

the external boundary conditions were imposed on the ISO container, rather than the package surfaces. A similar approach was also used for the TN-68 package, except that in the COBRA-SFS analysis, the rail car and package support cradle were neglected.

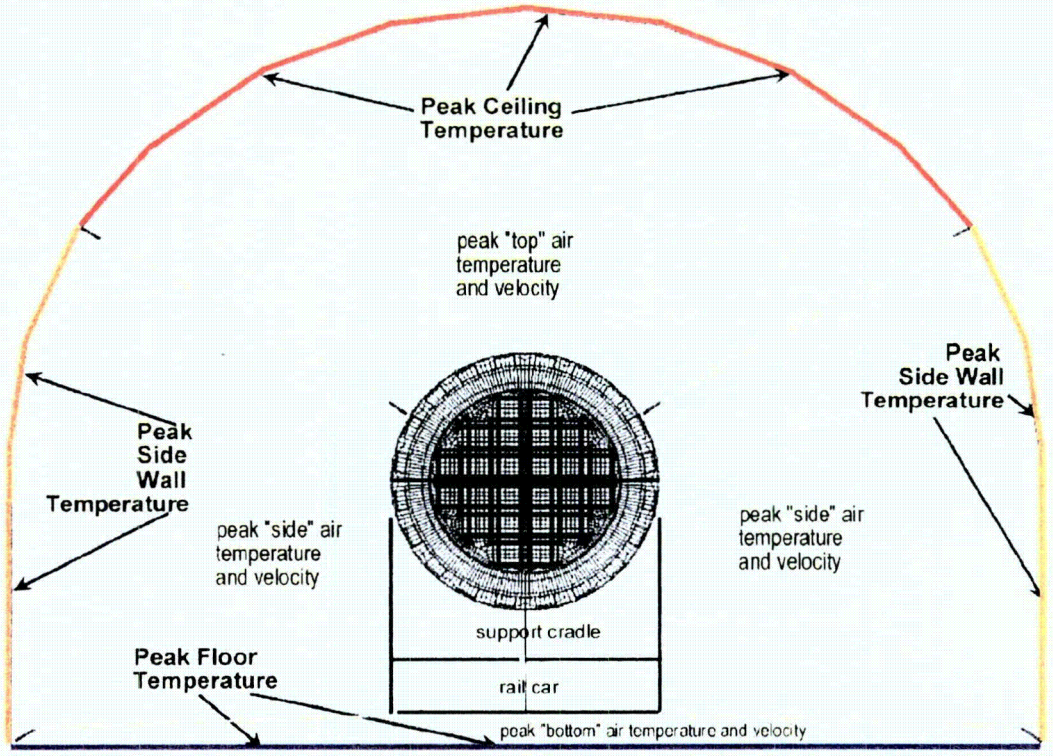

Figure 5.4. Cross-section of Tunnel (diagram not to scale) Showing "Top", "Side", and "Bottom" Regions for Fire Boundary Temperatures

5.2 Model of TN-68 Transportation Package

The TN-68 package was analyzed with COBRA-SFS, a code developed by PNNL for thermal-hydraulic analyses of multi-assembly spent fuel storage and transportation systems. The code uses a lumped-parameter finite-difference approach for predicting flow and temperature distributions in spent fuel storage systems and fuel assemblies under forced and natural circulation flow conditions. It is applicable to both steady-state and transient conditions in single-phase gas-cooled spent fuel packages with radiation, convection, and conduction heat transfer. The code has been validated in blind calculations using test data from spent fuel packages loaded with actual spent fuel assemblies as well as electrically heated single-assembly tests [13,14,15].

The TN-68 package was modeled in COBRA-SFS as a one-half section of symmetry. Figure 5.5 shows a diagram of the center cross-section of the basket and support rails as represented in the COBRA-SFS

model. The fuel assemblies within the basket are each modeled as detailed rod and subchannel arrays, and the tubes containing the fuel assemblies are represented using solid conduction nodes.

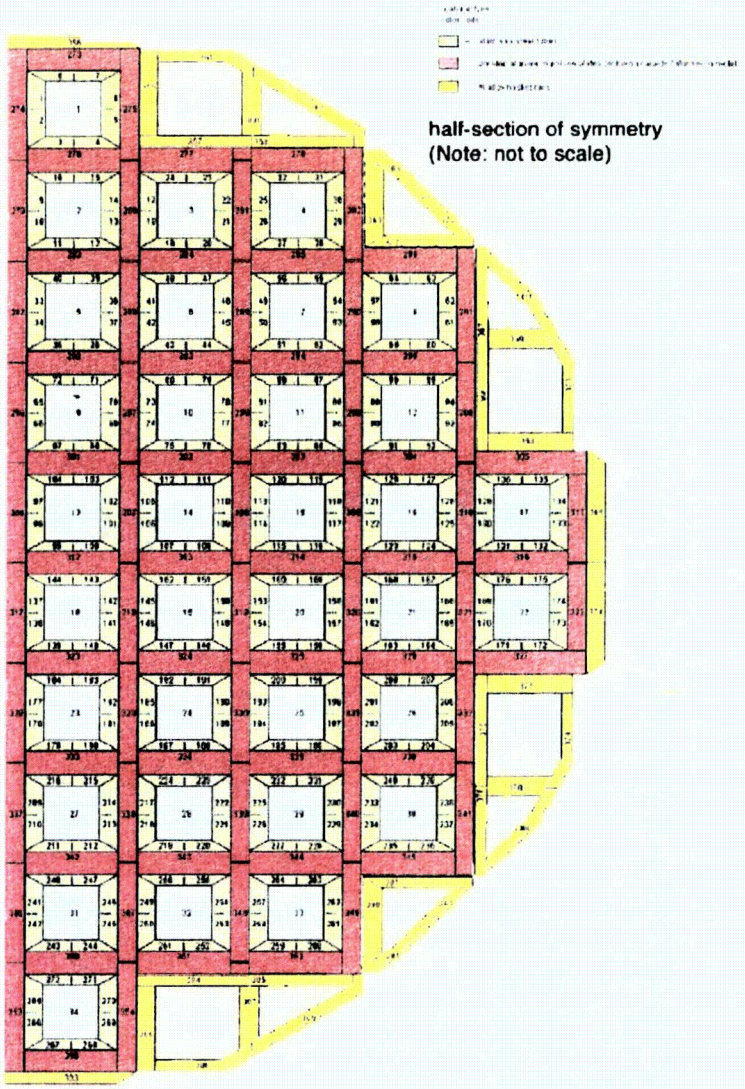

Figure 5.5. COBRA-SFS Model of TN-68 Basket and Support Rails

The aluminum and borated aluminum neutron poison plates sandwiched between the tubes are represented as an interconnected network of solid conduction nodes. The gamma shielding, neutron shielding, and outer steel shell are represented with concentric rings of interconnected solid conduction nodes with appropriate material properties. (For clarity, these nodes are not included in the diagram shown in Figure 5.5.) The half-section of the TN-68 package is represented with approximately 69,000 fluid nodes, 53,000 fuel nodes, and more than 16,000 solid conduction nodes.

The solid conduction nodes extend over 32 axial divisions comprising the axial length of the package. In cross-section, the stainless steel tubes containing the fuel assemblies are represented using two solid conduction nodes on each face of the enclosure, for a total of eight nodes per tube. The aluminum and borated aluminum neutron poison plates sandwiched between the tubes are represented as an interconnected network of solid conduction nodes that are in intimate physical contact with the stainless steel tubes and with each other. A total of 272 nodes are used to represent the 34 steel tubes in the half-section of symmetry. The borated aluminum neutron poison plates making up the rest of the basket are modeled with a total of 83 solid conduction nodes. The aluminum alloy basket rails are represented with a total of 36 solid conduction nodes, and provide appropriate thermal connections between the basket and the steel inner gamma shield.

The gamma shielding, neutron shielding, and outer steel shell are represented in the COBRA-SFS model as concentric rings of interconnected solid conduction nodes. The spent fuel arrays within the basket are assumed to be 7 x 7 BWR assemblies (the design basis fuel loading for the TN-68, as specified in the SAR [9]). Each assembly is modeled in detail, with 49 rods and 64 subchannels.

In cross-section, the gamma shielding is represented with two rings of 16 nodes each, representing the inner and outer steel shells of this component. The neutron shield in cross-section is represented with three rings of nodes (for a total of 48 nodes), with properties and connections defined to represent the material properties and thermal interactions of the ring of aluminum boxes filled with borated polyester. In cross-section, the outer steel shell of the package is represented with a ring of 16 nodes, with appropriate thermal connections to the neutron shielding on one side and ambient air on the other.

The COBRA-SFS model was verified by running the steady-state case for design basis normal hot transport conditions. The predicted peak clad temperature for these conditions was compared with the peak temperature reported in the SAR. The code predicts a peak clad temperature of 485°F (252°C); the SAR gives a value of 490°F (254°C) for these conditions (see Chapter 3, Table 3-1 in the SAR [9]).

The steady-state solution obtained for normal hot transport conditions was used to define the pre-fire condition for the package in the transient calculations simulating the Baltimore tunnel fire. This provides a reasonably conservative estimate of the initial temperatures throughout the package, since the boundary conditions for normal hot transport are specified as 100°F (38°C) ambient temperature in still air with insolation.

The external air temperatures predicted for the fire in the NIST simulation are sufficiently high to boil off the borated polyester neutron shield and completely char the wooden impact limiters. In both cases, the normal material would be replaced with material that would tend to insulate the package from the fire (i.e., air in place of the borated polyester, charred wood in place of the wooden impact limiter material).

To maximize the heat load to the package from the fire, it was assumed for the purposes of the calculation that these materials would persist intact throughout the fire (rather than gradually degrading or burning off). Then at the end of the fire (6.75 hours into the transient), these materials would be instantly transformed to a degraded condition. For the nodes modeling the neutron shield, this was simulated in the calculation by changing the material properties to those of hot air at the end of the fire. The material

properties specified for the nodes modeling the wooden impact limiters were changed from redwood to charcoal at the end of the fire.

The material properties from the package vendor's SAR were verified and then used in the analyses [9]. The material properties used in this evaluation are given in Appendix A.

5.3 Model of HI-STAR 100 Transportation Package

The ANSYS model of the HI-STAR 100 package consists of a detailed three-dimensional representation of a half-section of symmetry for the package, its cradle support[15], and the rail car decking directly below the cradle. (The remainder of the rail car was omitted from the model, as a conservatism, because it would partially shield the package from thermal radiation from the hot tunnel surfaces and block convection heat transfer to the package due to the flow of hot gas generated by the fire.) This half-section model of the package was placed within a complete cross-section of the surrounding tunnel.

The model developed for the HI-STAR 100 package utilized 120,412 SOLID70 and 1,542 SHELL57 thermal elements for conduction. It used two groups of 13,573 SURF152 surface effect elements for handling convection states in the pre-fire steady state and the fire accident transient. For radiation interaction, 288 highly structured AUX-12 generated MATRIX50 superelements were constructed using SHELL57 elements. Solar insolation (from 10CFR71 [1]) for the pre-fire condition was assigned via heat generation to the first group of 13,573 SURF152 surface effect elements. A portion of the model is shown in Figure 5.6. (In this figure most of the tunnel has been omitted for clarity.)

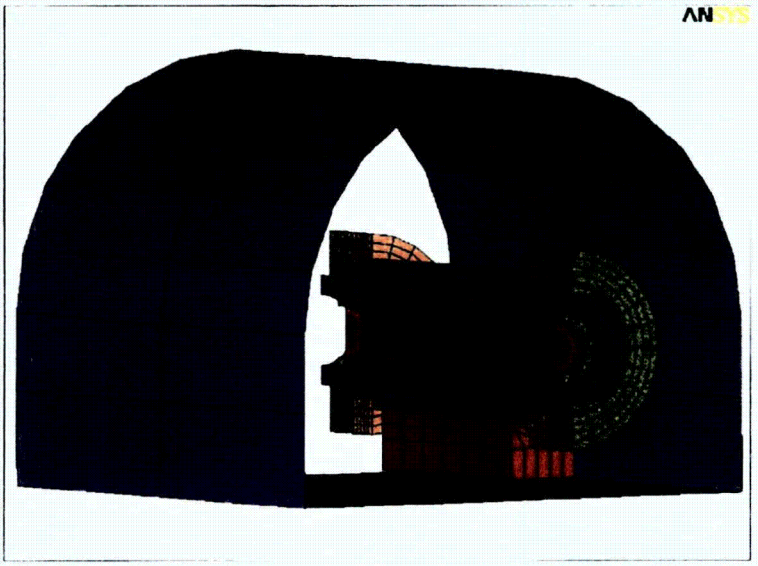

Figure 5.6. ANSYS HI-STAR 100 Package Analysis Model Element Plot

[15]Dimensions and materials for the rail car decking and the cradle were based on specifications (as of June 2005) from the package vendor. Cradle design determines the height of the package within the tunnel, the geometry of direct conduction paths to and from the package, and can affect thermal shielding of the package during the fire.

The material properties from the package vendor's SAR were verified and used in the analysis [10]. The model explicitly represents the geometry of the package, including the internal geometry of the fuel basket, all gaps associated with the basket construction, as well as the integral neutron absorber plates. Figures 5.7 through 5.11 show cross-sections of the HI-STAR model highlighting key features that were included.

Figure 5.7 shows the cross-section of the package, canister, cradle, and transport car section. In this figure, all helium conduction volumes have been removed for visualization purposes. The cradle and rail car sections were modeled as hollow enclosures. All internal thermal radiation exchange for these two enclosures were accounted for using AUX-12 generated MATRIX50 superelements (constructed with SHELL57 elements). Convection influences were accounted for using SURF152 elements with the extra node option.

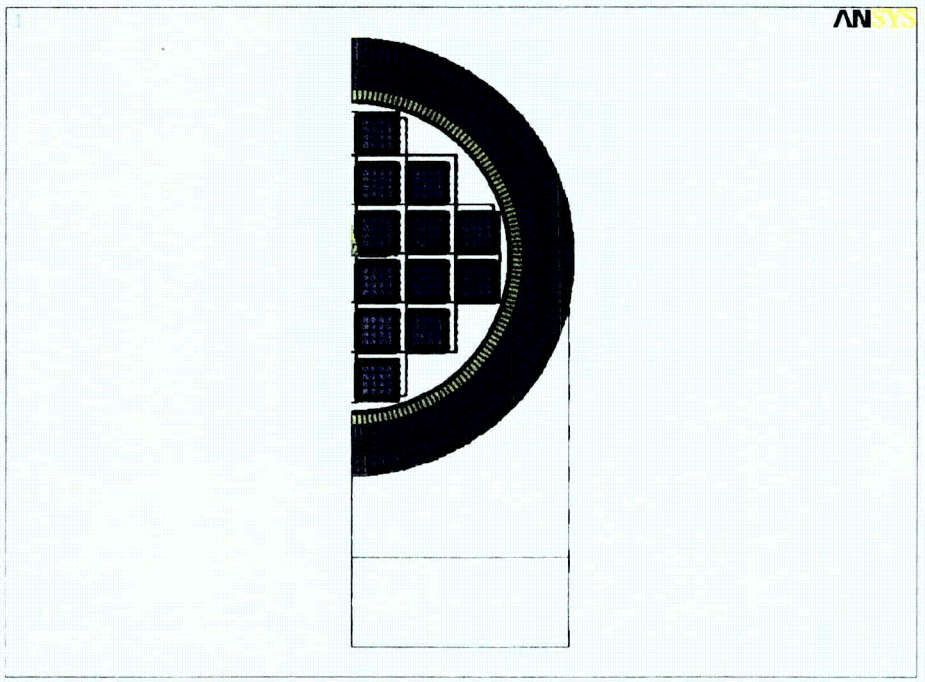

Figure 5.7. Cross-section of Package, Cradle, and Rail Car Section

Conduction within the cradle and trailer material sections was also accounted for using additional SHELL57 elements with thickness option applied. Natural convection correlations and specially constructed automated subroutines written in ANSYS Parametric Design Language (APDL) were used to continuously evaluate and update the convective coefficients of heat conductance. Fourteen separate passive computation nodes were assigned as "extra nodes" for the SURF152 surface effect elements used in specifying the convection interaction within the cradle and rail car section (seven for each – not shown in Figure 5.7). Section 6 presents a discussion of the natural convection correlations used in this analysis.

Figure 5.8 shows the cross-section of the package and canister, with the overall basket structure. As in Figure 5.7, all helium conduction volumes have been removed for visualization purposes. This figure shows the fuel compartment layout within the MPC-24 basket structure, and includes the inner shell (light green), gamma shield (dark blue), and the neutron shield (purple) components of the HI-STAR 100.

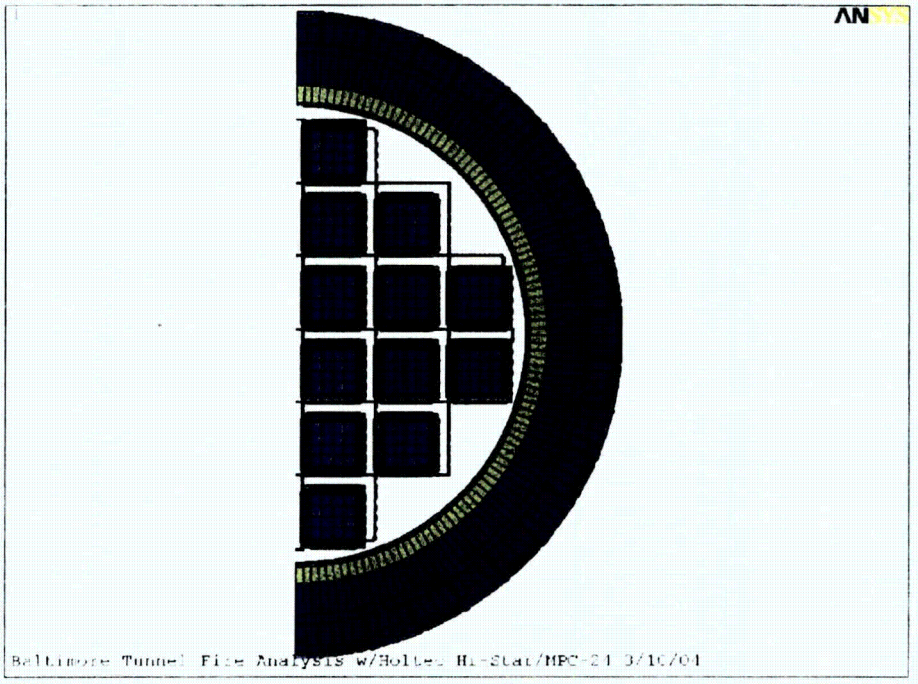

Figure 5.8. Cross-section of HI-STAR Package and MPC-24 Canister

The model cross-section in Figure 5.9 shows that the fillet welds joining the sections of the package outer skin and the expansion foam in the neutron shield area have been modeled explicitly. Special element material definitions were created for the elements providing the connection between the fins enclosing the neutron shield and the gamma shield. The material definition was specified such that the thermal conductivity could be readily degraded to represent the effect of single-sided fillet welds (i.e., not full penetration) that are used in this connection. Since the thermal conductivity through single-sided fillet welds is difficult to determine objectively, the conductivity of this material in the pre-fire steady state and post-fire transient was conservatively reduced to half of that of the solid base material. The effect of this assumption is to conservatively minimize the rejection of internal heat. During the fire, however, the thermal conductivity of these elements was assumed to be the same as the solid base material, mimicking that of a full penetration weld. This approach was used to conservatively maximize the heat input into the package during the fire.

Special material definitions were also created for the elements making up the multi-layer steel gamma shield (dark blue in Figures 5.8 and 5.9). To account for the probability of gaps between the five steel shells due to standard manufacturing practices, a gap of 0.01 inch was assumed to exist between each layer. Effective material thermal conductivities were then calculated for the gaps, accounting for

conduction through gas in the gap and radiation across the gap. These material property definitions were used in the pre-fire steady state and the post-fire transient to conservatively minimize the rejection of internal heat; However, during the fire, the conduction properties of these elements were reassigned to that of solid material (i.e., equivalent to assuming no gaps between these layers during the fire), to conservatively maximize the heat input into the package. A complete list of the material properties used in this evaluation is presented in Appendix B.

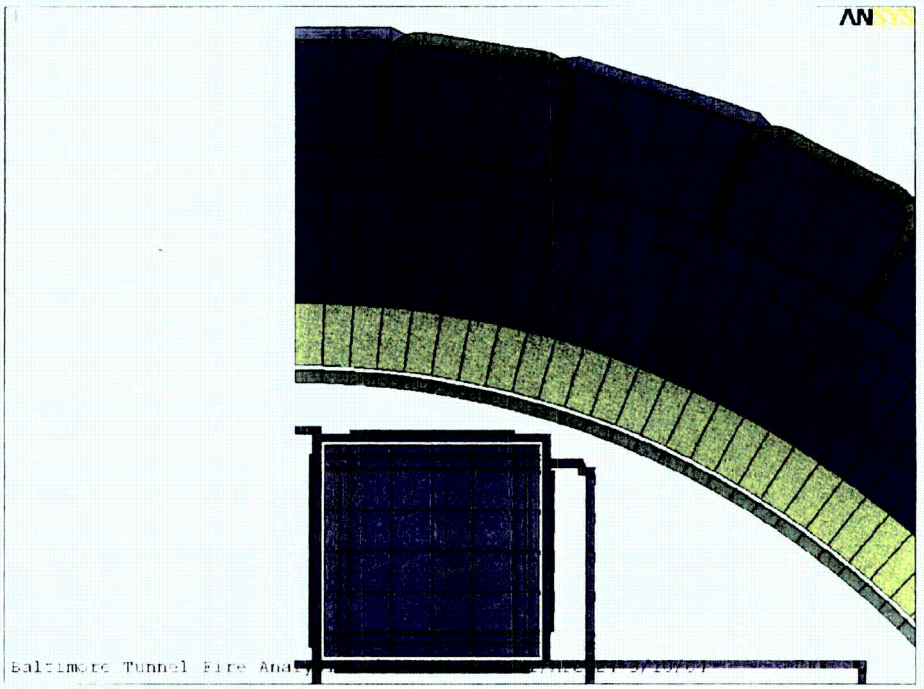

Figure 5.9. Close-up of Package Cross-section

Figure 5.10 presents a detailed view of the basket cross-section showing a typical basket fuel compartment (purple) containing a homogenized fuel assembly (light blue) surrounded by Boral sheets and their associated sheathing. Also shown in this figure are the MPC canister shell (blue-green) and the package containment/inner shell (lime). The same features are shown in Figure 5.11 with the elements for the helium regions included.

Westinghouse 17x17 OFA fuel was modeled in this evaluation. The effective fuel conductivity in the radial direction was determined using the approach documented in the HOLTEC SAR [10]. This approach uses a homogenization scheme similar to that presented by Bahney and Lotz [16], modified to include a helium gap between the homogenized fuel region and the fuel compartment, and the effect of cover gas pressurization.

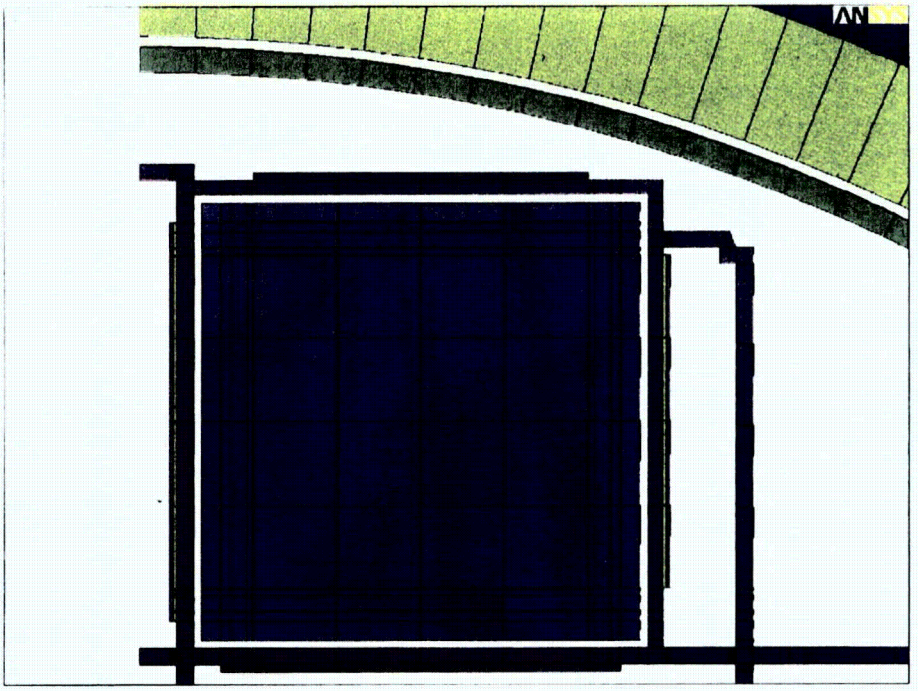

Figure 5.10. Close-up of Canister Basket and Fuel Compartment (without helium elements)

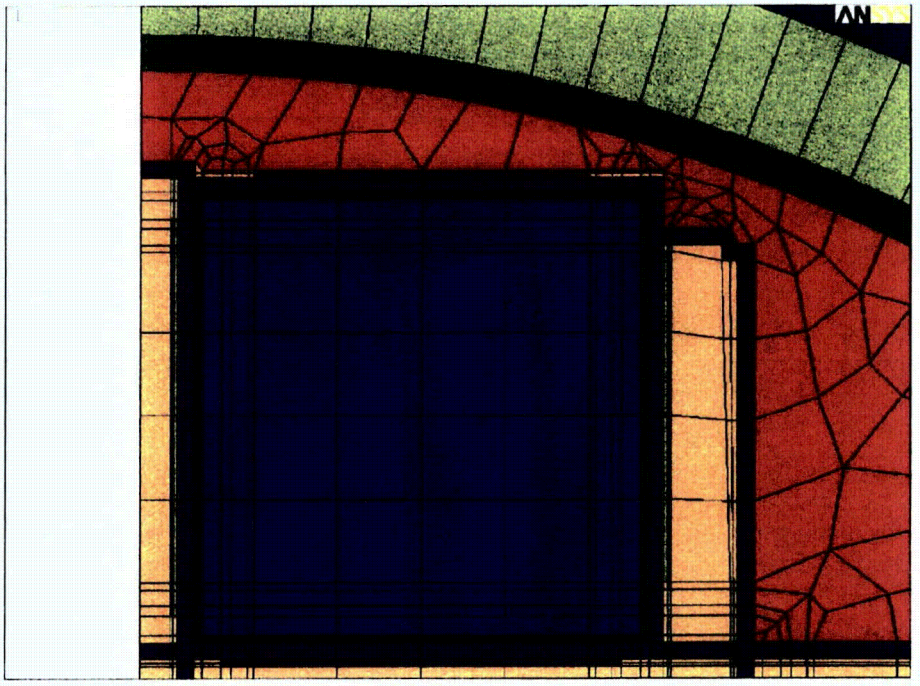

Figure 5.11. Close-up of Canister Basket and Fuel Compartment (with helium elements)

Axial conductivity for the homogenized fuel region was modeled with the cladding as the only conduction medium, using a cross-sectional area weighting scheme. The remaining portion of the homogenized region was considered to be helium. Density and heat capacity were based on volumetric averages of the cover gas, cladding, upper and lower end fittings, and uranium dioxide fuel. A normalized peaking factor of 1.1 (from the design basis axial power distribution in the SAR [10]) was used to establish the volumetric heat generation of 2,843 Btu/hr (0.833 kW) over each assembly along the active fuel length. Orthotropic effective conductivity properties were developed for the Boral to include the radiation and conduction heat transfer components through an assumed helium gap of 0.0035 inch between the Boral sheet and its stainless sheathing, and between the Boral and stainless basket structure.

Radiation interaction within the basket, canister, and package was modeled by unselecting all helium regions and coating each interacting set of surfaces forming an enclosure with SHELL57 elements with specified emissivities. The SHELL57 elements were then used to produce highly structured AUX-12 generated MATRIX50 superelements, each defined by an enclosure. A total of 269 MATRIX50 superelements were defined to capture the radiation interaction within the package and canister. Figure 5.12 shows an element plot of the top impact limiter honeycomb core and steel substructure of the HI-STAR 100 package, including the Holtite-A neutron shield material sections. (The impact limiter skin is omitted for visual clarity.) The bottom impact limiter is similar to the top impact limiter, except for the bolting configuration and the extended steel ring covering the top forging, lid, and buttress plate. Figure 5.13 shows the top impact limiter skin and support structure, without the honeycomb core and the neutron shield materials included.

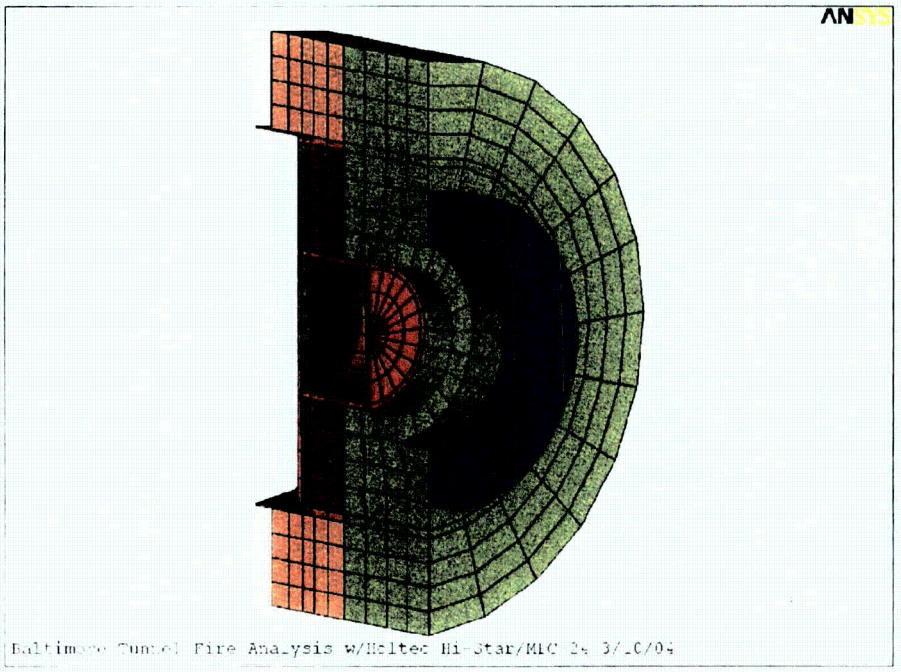

Figure 5.12. Complete Impact Limiter (Except Skin)

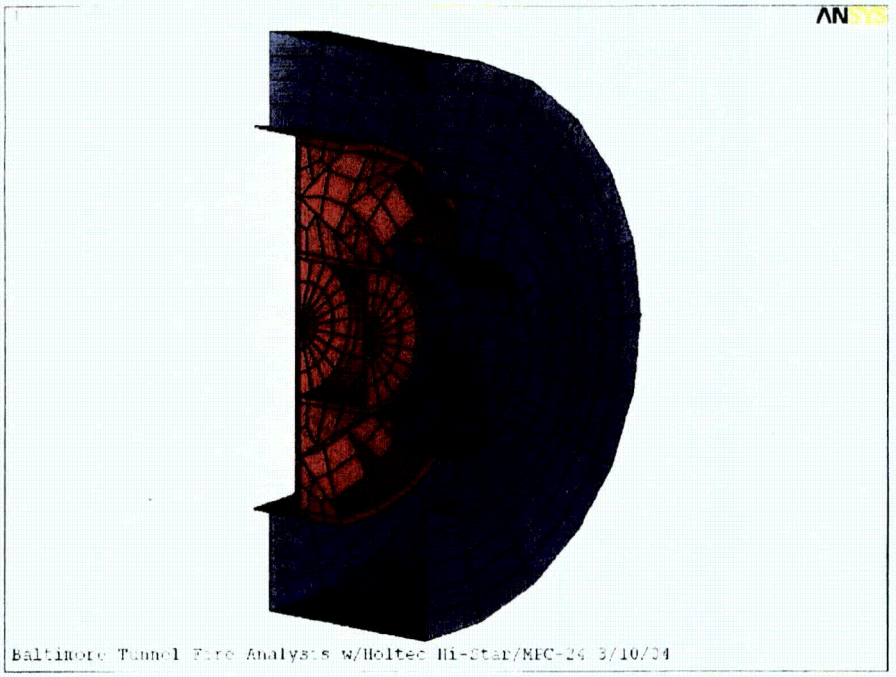

Figure 5.13. Impact Limiter Skin and Primary Support Structure

The impact limiters are assembled with five different types of honeycomb sections. Gaps between the honeycomb sections, the steel substructure, and skin were conservatively ignored to maximize heat input during the fire. Thermal properties for the honeycomb sections were based on volumetric averages of each section using properties published by the honeycomb manufacturer [17]. Radiation interaction between the package ends and impact limiters was modeled by coating each respective interacting set of surfaces with SHELL57 elements with specified emissive material properties. The SHELL57 elements were then used to produce highly structured AUX-12 generated MATRIX50 superelements. A total of 16 MATRIX50 superelements were defined to capture the radiation interaction between the package and impact limiter surfaces.

Conduction and natural convection heat transfer between the package and impact limiter surfaces was handled using SURF152 surface effect elements. Correlations and specially constructed automated subroutines written in APDL were used to continuously evaluate and update the assigned convection coefficients of heat conductance.

Sixteen separate passive computation nodes were assigned as "extra nodes" for the SURF152 surface effect elements used in specifying the convection interaction within the cradle and rail car section. (The natural convection correlations used are presented in Section 6.) Convection coefficients of heat conductance were conservatively boosted by a multiplicative factor of 100 between limiter and package during the fire to mimic enhanced heat conduction at this interface due to rapid thermal expansion. These values were returned to normal after the end of the fire.

The tunnel structure was represented by an enclosure approximately 22 ft (6.7 m) high by 27 ft (8.2 m) wide and 42 ft (12.8 m) long. The tunnel enclosure was divided into three regions; top, side, and bottom (as illustrated in Figure 5.4). The bottom region consisted of the floor of the enclosure. The top region was conservatively considered to be all surfaces in the range from 15.8 to 22 ft (4.8 to 6.7 m). All surfaces from the floor to 15.8 ft (4.8 m) were considered to be the side region. The specified boundary temperatures for each region section are the maximum calculated in that region (top, side, and bottom, corresponding to ceiling, wall, and floor in the FDS simulation from NIST; see Section 6). The enclosure was capped at both ends and assigned the same boundary condition on the end caps as on the walls and ceiling. As specified by dimensions of the rail car decking and cradle, the transport system was located such that the center axis was 8.2 ft (2.5 m) above the tunnel floor, leaving 12.2 inches (31 cm) underneath the lowest part of the rail car decking.

To determine the convection heat transfer to the package during the fire scenario, the exposed surfaces of the package were also divided into three regions. The top region was defined as all surfaces above an elevation of 9.4 ft (2.9 m). The bottom section was defined as the bottom of the rail car segment of the model. The side surfaces of the package were conservatively defined to be all remaining outer surfaces of the package. The surface elements of each of these sections are pictured in Figures 5.14, 5.15 and 5.16. Forced and natural convection correlations and specially constructed automated subroutines written in APDL were used to continuously evaluate and update the assigned convective coefficients of heat conductance for the surface of the package during pre-fire, fire, and post-fire phases based on gas velocity. The bottom surface of the rail car section was the only surface influenced by convection heat transfer in the bottom gas region. In actuality, none of the "top" surfaces would be directly exposed to the highest temperature gas region at the top of the tunnel, because the package is not positioned that high in the tunnel. This assumption therefore represents an additional conservatism in the analysis.

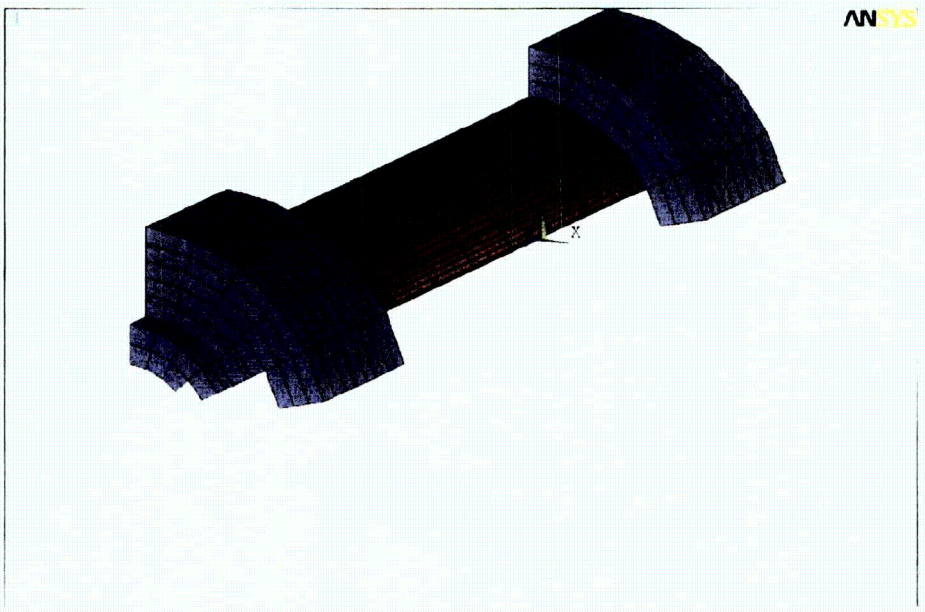

Figure 5.14. Surfaces Defined for Interaction with "Top" Gas Region

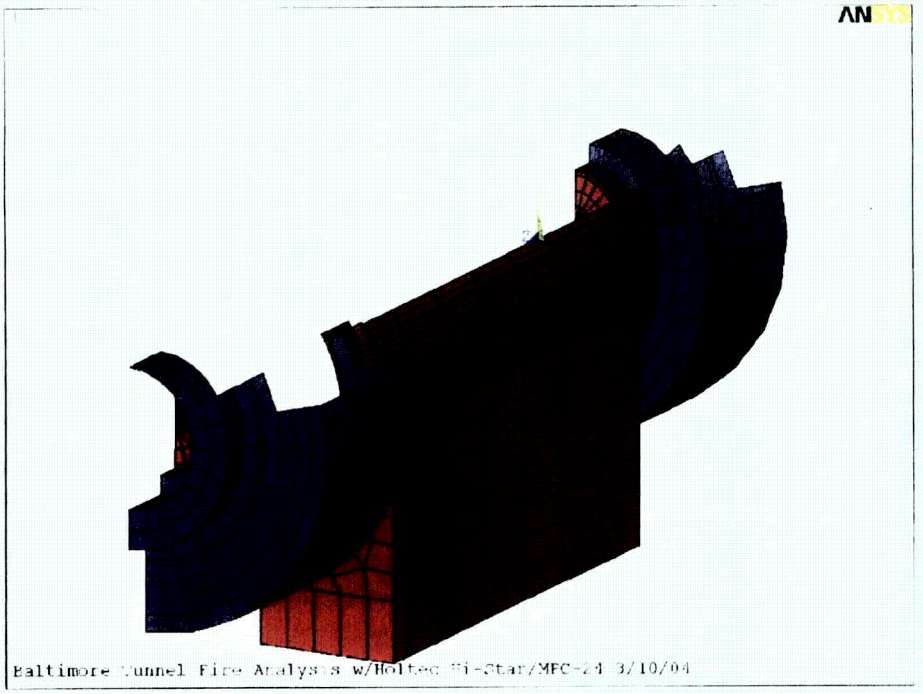

Figure 5.15. Surfaces Defined for Interaction with "Side" Gas Region

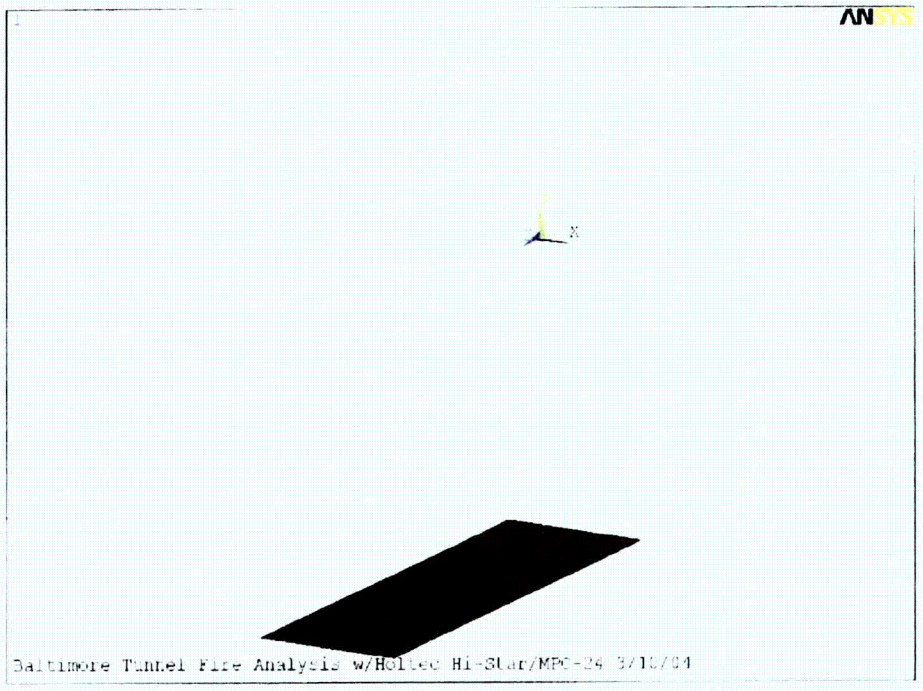

Figure 5.16. Surfaces Defined for Interaction with "Bottom" Gas Region

Radiation interaction between the transport system (with its partial conveyance) and the tunnel surfaces was established by coating all respective interacting surfaces with SHELL57 elements with specified emissive material properties. The SHELL57 elements were then used to produce a highly structured AUX-12 generated MATRIX50 superelement.

The Baltimore tunnel fire evaluation of the HI-STAR 100 was conducted in three phases. These were the pre-fire, fire, and post-fire phases. For the pre-fire phase, the hot-normal conditions of transport were evaluated assuming solar insolation and a 100°F (38°C) ambient temperature, in accordance with 10CFR71.71 [1]. This conservatively established initial component temperatures. During this phase, the fillet welds joining the fins to the gamma shield were specified with their realistically reduced conduction and conservative gas gaps were assumed between the layers of the gamma shield.

For the fire phase of the evaluation ($0 < t \leq 7$ hr), solar insolation was shut off, the tunnel surfaces were introduced, and the transport package and tunnel surfaces were assigned an emissivity of 0.9 to represent surfaces affected by sooting. Air gaps originally assumed to be present between the gamma shield plates in the initial pre-fire steady state were closed, and perfect contact for conduction was assumed to exist where the heat fins attach to the gamma shield. Convection coefficients of heat conductance were conservatively multiplied by a factor of 100 between the impact limiters and package body to mimic enhanced heat conduction due to rapid thermal expansion. In addition to these conservative measures, all aluminum honeycomb and neutron shield resin materials were assumed to remain intact during the full duration of the fire, to maximize heat input during the fire.

For the post-fire phase ($t > 7$ hr), aluminum honeycomb sections that exceeded an average temperature of 1220°F (660°C) and all neutron shield material sections were degraded to thermal properties of air. The energy that would be absorbed due to phase change in this material was not subtracted from the heat input into the package. In addition, all gamma shield gaps and reduced fin fillet weld conduction properties were reintroduced. Finally, convection coefficients of heat conductance between the impact limiters and package body were returned to normal for the remainder of the simulation.

5.4 Model of NAC LWT Transportation Package

The model for the NAC LWT package constructed in ANSYS is similar in structure to the HI-STAR 100 model described in Section 5.3, with the additional feature that the NAC LWT package is enclosed in an ISO container[16]. A detailed 3-D model of a half-section of symmetry was developed for the package and ISO container, within the same tunnel geometry as that used for the HI-STAR 100 model. A diagram of the package and shipping container model and partial tunnel is shown in Figure 5.17. The model used 40,333 SOLID70 8-node brick elements and 3,409 SHELL57 4-node quadrilateral thermal elements to represent the structural components. A total of 6,931 SURF152 elements were used to incorporate radiation and convection heat transfer to the ISO container and tunnel environment for the various surfaces, and 12 MATRIX50 elements were used to model radiation heat exchange between package

[16] The CoC for this SNF package requires that it be enclosed in either a personnel barrier (PB) or an ISO container. Current DOE policy requires an ISO for truck casks shipped by rail, and every rail shipment of the LWT to date has been in an ISO container.

surfaces. The surface effect elements were also used to generate solar insolation loads for calculation of the initial temperature distribution for the package.

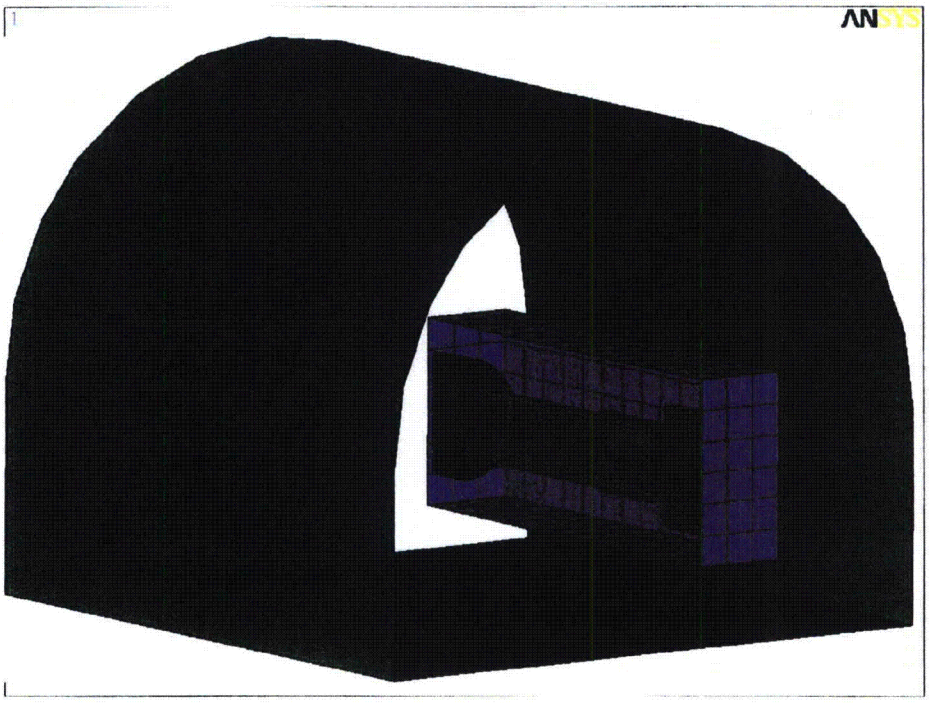

Figure 5.17. ANSYS NAC LWT Package Analysis Model Element Plot

The model geometry was developed from the vendor's engineering drawings from the package SAR [11]. The model cross-section is shown in Figure 5.18. The package contains a cylindrical solid aluminum basket that holds a single fuel assembly. The helium gaps between the fuel and the basket, and between the basket and package shell, were explicitly modeled with solid elements.

The package body is constructed of several stainless steel shells to provide structural support and gamma shielding. The innermost shell is surrounded by a layer of lead that acts as a gamma shield. The outermost stainless steel shell is surrounded by an annular tank containing a solution of ethylene glycol and water which acts as a neutron shield. The tank is contained by an outer stainless steel skin and an annular overflow tank that extends approximately one-third of the axial length of the package body. All of these components were modeled using brick elements.

The tank is constructed with eight stainless steel support ribs (in the half section) connecting the skin to the outer shell. These structures were modeled with shell elements. The package bottom is constructed with a stainless steel base, a layer of lead shielding, and a steel cover. The upper end of the package is sealed with a stainless steel lid (see Figure 5.19). Impact limiters attached to the ends of the package consist of an internal aluminum honeycomb structure covered by an aluminum skin. The expansion tank to handle overflow of the liquid neutron shield consists of an outer stainless steel skin.

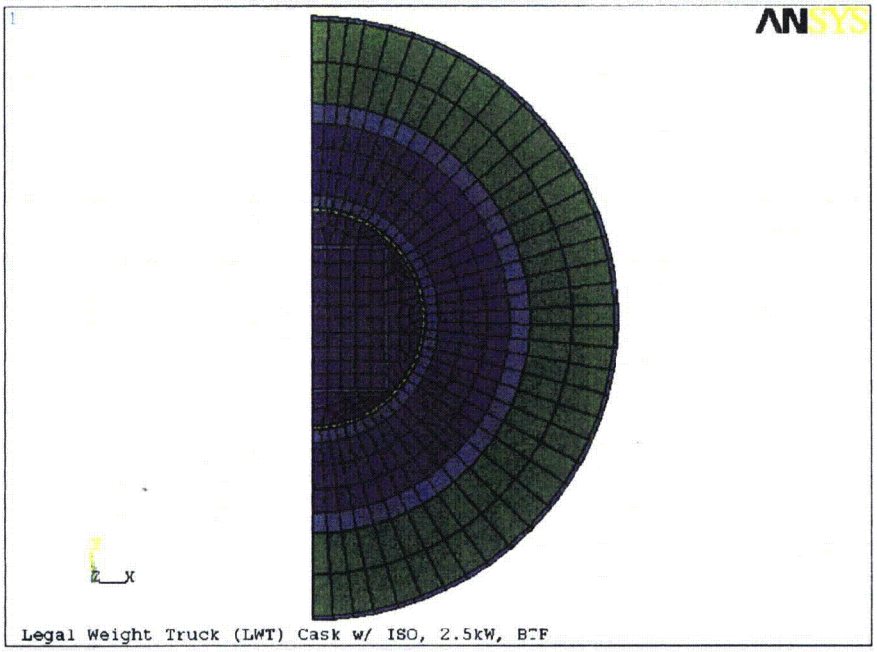

Figure 5.18. Cross-section of NAC LWT Package

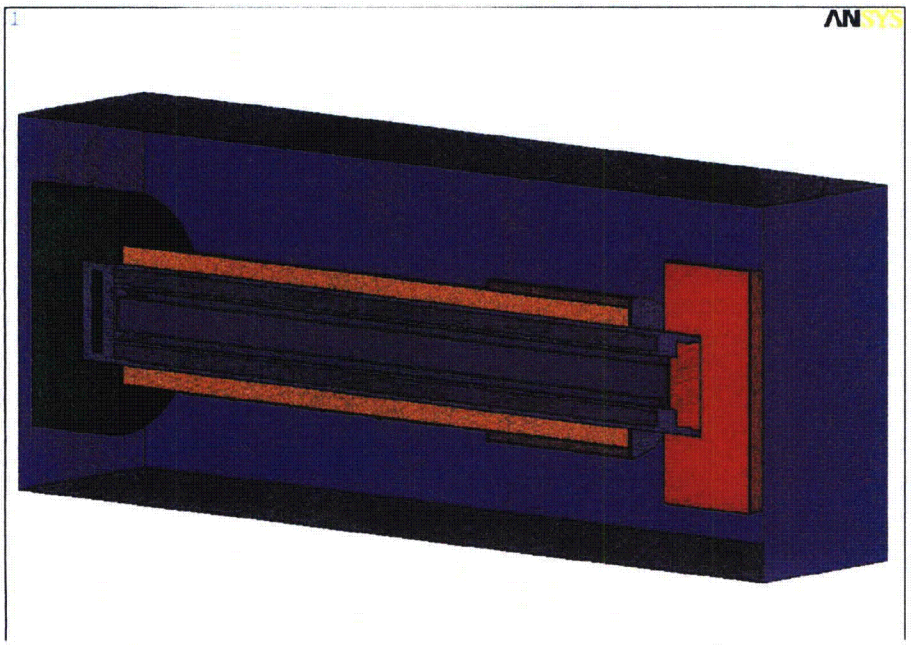

Figure 5.19. NAC LWT Package Geometry

The entire package is contained in an ISO container constructed of stainless steel plate. This is based on the assumption that an ISO container would be required if the NAC LWT were shipped by rail. (The consequences of this hypothetical accident scenario on a package shipped without an ISO container are discussed with the results of this analysis in Section 7.3.) The model of the package and container is oriented horizontally in the tunnel with the center of the ISO container 97.7 inches (248 cm) above the tunnel floor.

Heat exchange via conduction, convection, and radiation was modeled in appropriate detail between all of the components to provide a sound estimate of package temperatures during the transient fire event. Conduction is handled inherently by the elements modeling each component, but convective and radiation mechanisms must be separately implemented.

Westinghouse 17x17 OFA fuel was modeled in this evaluation. The fuel region was represented with an effective conductivity determined using a homogenization scheme similar to that presented by Bahney and Lotz [16], modified to include a helium gap between the homogenized fuel region and the fuel basket. This yields a more realistic representation of the temperature profile through the assembly, and takes into account the effect of the non-uniform wall temperature distribution around the assembly.

Axial conduction in the homogeneous fuel region was conservatively neglected in the fuel itself, and was modeled only in the cladding, using the conductivity of Zircaloy modified by a weighting scheme based on the cross-sectional area. The effective density and heat capacity for the fuel region was based on volumetric averages of the properties of the helium cover gas, fuel rod cladding, and uranium oxide fuel pellets. The design basis axial power profile from the SAR [11], which has a normalized peaking factor of 1.2, was used to establish the volumetric heat generation of 8,532 Btu/hr (2.5 kW) over the assembly along the active fuel length.

The 0.225-inch (0.57-cm) gap filled with helium cover gas between the fuel and the basket was modeled with solid elements and used standard helium thermal properties for conduction and specific heat. Convection was ignored in this small gap. Radiation exchange between the adjacent surfaces was modeled using MATRIX50 superelements. These were created by using SHELL57 elements to designate the discrete enclosure, and the AUX-12 hidden ray-tracing method was used to compute view factors for each element in the superelement. The 0.25-inch (0.64-cm) gap between the basket and the inner shell was modeled in the same manner, also assuming negligible convection.

The entire package model was enclosed within elements modeling the ISO container. For the large air volumes in the ISO container, conduction across the gaseous medium is negligible but significant convection currents will be created by the buoyant forces due to the heated surfaces. Surfaces with unobstructed views of other surfaces will also experience significant radiation exchange that is highly dependent on the surface geometry and physical condition. Therefore, heat exchange between the package exterior and the container interior was modeled with internal free convection and radiation between adjacent surfaces.

The radiation was implemented using the MATRIX50 superelement procedure described in Section 5.3 for the Holtec HI-STAR 100 model. The convection calculations were based on empirical relations for

free convection over flat plates and cylinders (see Section 6). Convection was implemented using SURF152 elements. These elements are defined on the exterior surface of a body and connect to the designated sink temperature assigned to a single node (called a "space node") to compute the heat flux. Because convection heat transfer rates are expected to vary in different regions throughout the ISO container, the single volume was divided into 17 zones. These consisted of a zone on each end of the package, three zones representing the top, side, and bottom radial surfaces for each impact limiter, and similar zones for the package for three locations along its axial length (see Figure 5.20).

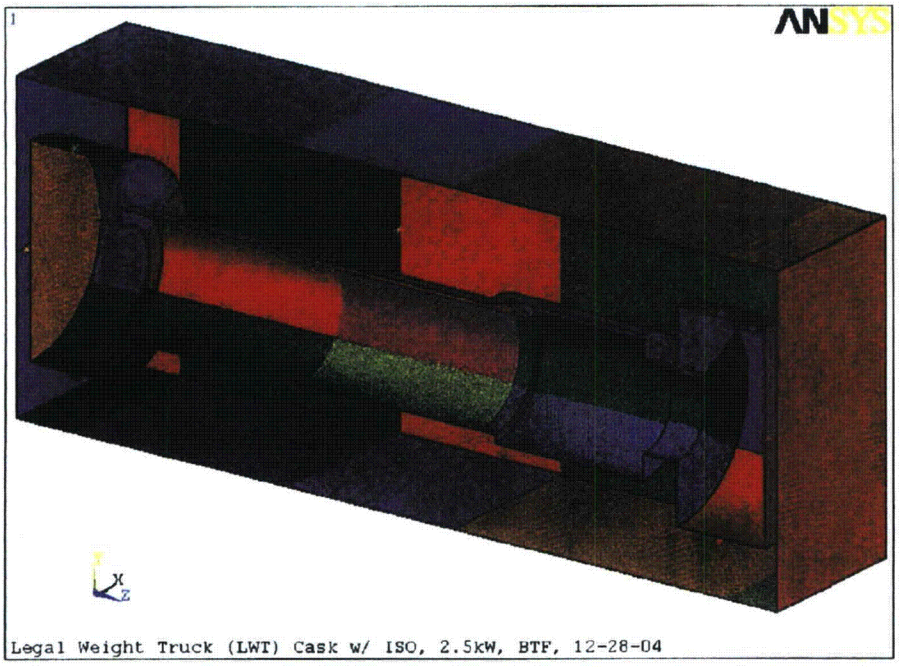

Figure 5.20. Zones for Convection Heat Transfer Within the ISO Container

A sink temperature was defined for each zone, computed as the average surface temperature of the participating package and container elements for that zone. The convective heat transfer coefficient was assigned to the package and container elements based on the temperature difference between the surface and sink temperature, and the surface geometry, as described in Section 6. The heat exchange between these surfaces and the space node was then computed by ANSYS during the solution.

Convection and radiation are also the two mechanisms required to model thermal exchange from the exterior of the ISO container. In the fire analysis, the initial temperature distribution is obtained from a steady-state solution with conditions specified by 10CFR71.71 [1], followed by a transient solution representative of the fire. For the steady-state solution, convection is handled by SURF152 elements with a constant convection coefficient of 0.891 Btu/hr-ft^2-°F (5.06 W/m^2-°K) and an ambient temperature of 100°F (38°C). Solar insolation is incorporated by using SURF152 elements with heat generation on the outer surface at the rate specified in 10CFR71 [1].

During the fire, the sink node temperature for each of the SURF152 elements is set and the external convection coefficient is computed using a forced convection relation derived using the gas temperatures and velocities from the results of the NIST fire simulation using FDS. These results were obtained for the top, side, and bottom of the tunnel, and applied to three zones defined on the top, sides, and bottom of the ISO container, as illustrated in Figure 5.21. By the end of the transient simulation using FDS (i.e., 30 hours), the predicted gas velocities have dropped to the point that free convection is the only significant mode of convection heat transfer. From this point in the transient, the convection coefficient is computed in the same manner as described for the steady-state initial conditions.

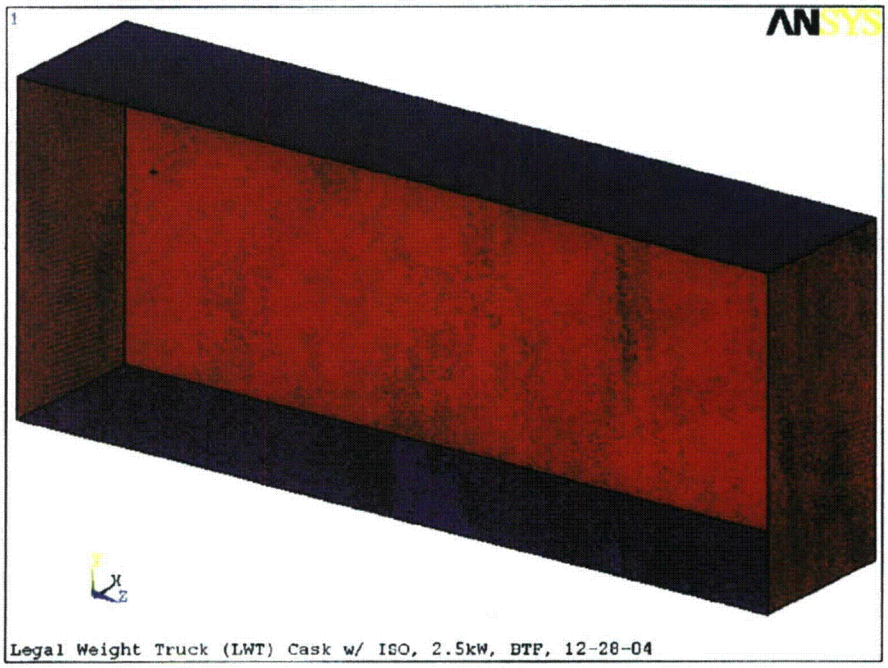

Figure 5.21. Zones for External Radiation Between ISO Container and Tunnel Surfaces

Thermal radiation between the container and the tunnel during and after the fire is incorporated by the MATRIX50 elements, as described previously, where the top, side, and bottom temperatures of the tunnel from the NIST fire simulation are imposed as boundary conditions. A conservative emissivity value of 0.9 was used for the tunnel surfaces and ISO container exterior, to account for the effect of sooting.

The material properties used in the thermal model are listed in Appendix C, and were obtained primarily from the vendor's SAR [11]. Some modifications were made to the material properties to account for structural configuration and expected effects of the fire. More comprehensive material properties were needed for the lead comprising the gamma shielding, to accommodate the effects of melting and resolidification during the transient. For the impact limiters, the significant void volume of the aluminum honeycomb material reduces the heat transfer capability compared to the same thickness of solid material. The thermal conductivity assigned to elements modeling the impact limiters was scaled by the ratio of the honeycomb density to the solid aluminum density.

Modeling of the liquid neutron shield was complicated by the expectation that the 56% ethylene glycol liquid will exceed its boiling point during a fire transient, leading to tank rupture and vaporization of the contents, which significantly affects the heat transfer of the package. Prior to rupture, the liquid in the tank is expected to sustain convective currents due to temperature gradients through the liquid between the tank surfaces. After rupture, empirical relations were used to obtain separate effective conductivities for the shield tank and expansion tank.

The empirical relations were based on correlations by Raithby and Hollands [18], as described in Section 6. The effective conductivity was then determined as a function of the average tank temperature and the radial temperature difference between the tank inner and outer surfaces. The material properties were updated between each time step during the transient solution using APDL. They were computed for the 56% ethylene glycol solution up to the point where the average temperature reached its boiling point of 350°F (177°C).

When the average temperature in the tank exceeded the boiling point, it was assumed that rupture occurred and the liquid was immediately vaporized. After that point, the effective conductivity was computed using dry air as the medium. This calculation was continued during the cool down period also. This formulation conservatively neglects energy absorbed by the phase change (i.e., the heat of vaporization for the liquid), although this is mainly as a matter of convenience, since this would constitute a relatively small deduction from the total energy imparted to the package.

The general solution procedure for this model was similar to that for the HI-STAR 100 described previously. The steady-state temperature solution for normal hot conditions was computed using solar insolation and 100°F (38°C) ambient temperature per 10CFR71.71 [1], and used as the initial temperature state. The insolation was removed and the tunnel was introduced for the transient fire analysis. The transient solution was then obtained for the 30 hours of the NIST simulation, representing the 7-hour fire and 23-hour cool down. The solution was also extended for a total simulation time of 300 hours, in the same fashion as described in Sections 5.1 and 5.2 for the other two package models.

6 ANALYSIS METHOD

The National Institute of Standards and Technology (NIST) performed analyses using the FDS code, to determine the type of fire that could have been sustained during the accident in the Howard Street tunnel and the possible fire duration. A conservative simulation was used to define the boundary conditions for COBRA-SFS and ANSYS evaluations of the thermal response of the selected spent fuel transportation packages. Section 6.1 lists the assumptions underlying the analytical approach used and describes in detail the boundary conditions obtained from the selected FDS simulation. This includes temperature boundary conditions and the approach used to define convection and radiation heat transfer rates. Section 6.2 describes the initial steady-state conditions defined for each package. Section 6.3 describes the procedure used for the transient calculations.

6.1 Modeling Assumptions and Boundary Conditions

A number of conservative assumptions were made in the evaluations of the thermal response of the three spent fuel transport packages (TN-68, HI-STAR 100, and NAC LWT) to the Baltimore tunnel fire transient. The assumptions of greatest impact are listed below.

(1) Boundary conditions were taken from a conservative simulation in which the fire is predicted to burn at a rate that is approximately an order of magnitude hotter than the rate predicted for the actual environment within the tunnel. In this conservative simulation, the fire was assumed to be fully ventilated, with a relatively small pool area, and burned until the entire supply of tripropylene fuel was consumed by combustion (as described in Section 2).

(2) Boundary temperatures for the analyses in the current study were taken from predictions of peak gas temperatures in the lower, middle, and upper zones of the tunnel and peak surface temperatures on the tunnel floor, walls, and ceiling. The peak values in each region were used to define boundary temperatures over the entire region, rather than using the local or average temperatures predicted in the FDS calculation. This approach ensures a conservative estimate of the boundary temperatures, since the package does not see the peak temperatures on all surfaces, and in some regions may not see the peak temperature on any surface. (For example, the uppermost surface of the package (in the horizontal orientation) is not high enough to be exposed to the peak gas temperature at the top of the tunnel, but this value was used as the ambient temperature for convective heat transfer to the upper surface of the package.)

(3) The package cradle and the rail car section beneath the cradle were included in the ANSYS model of the HI-STAR 100, but the rail car ends and honeycomb end blocks adjacent to the impact limiters were omitted. These structures were neglected because they would partially shield the package from thermal radiation from the hot tunnel surfaces and block convection heat transfer to the package due to the flow of hot gas generated by the fire. The rail car was omitted from the COBRA-SFS model of the TN-68 package and the ANSYS model of the NAC LWT package within the ISO container. This approach eliminated any shielding of these packages from thermal radiation and convective heat transfer from the tunnel environment.

(4) During the fire ($0 < t < 7$ hr) and in the short-term post-fire cool down (7 hr $< t < 30$ hr), it was assumed that convection heat transfer at the package surface was forced convection only (due to air flow induced in the tunnel by the temperature gradients of the fire), using gas velocities predicted in the NIST analysis. This approach neglects the possible contribution of free convection around the package (due to non-uniform circumferential temperatures around the package outer shell), which would tend to remove heat from the package. The boundary condition was switched to solely free convection after 30 hours, in the extrapolated portion of the transient. This conservatively neglects any forced convection cooling of the package during the extended cool down period, when the gas velocities in the tunnel are predicted to have dropped to relatively small values.

(5) The effect of optical densification due to combustion products and material degradation, which would tend to attenuate the radiation influence between the tunnel and package surfaces, was not taken into account in the boundary conditions defining the fire. Radiation views were treated as clear and unobscured at all times. Radiation attenuation was also neglected between the ISO container inner surfaces and the NAC LWT package surfaces.

(6) The wooden impact limiters on the TN-68 were assumed to remain intact during the fire, to maximize the heat input into the package. At the end of the fire, the thermal conductivity value for the nodes representing this material was reduced to that of charcoal. As a result, these components then present an added thermal barrier to heat removal from the package after the fire.

(7) Similarly, the aluminum honeycomb impact limiters on the NAC LWT and the HI-STAR 100 were assumed to remain intact during the fire. At the end of the fire, the thermal conductivity values for the portions of the impact limiters that had exceeded the melting temperature of aluminum were reduced to that of air. The thermal energy absorbed in the melting process, however, was conservatively neglected, and was not subtracted from the heat input to the package during the fire.

(8) For the TN-68 and the HI-STAR 100, the resin materials comprising their neutron shielding were assumed to remain intact during the fire, to maximize the heat input into the package. At the end of the fire, the thermal conductivity values for these materials were reduced to that of air. As a result, the neutron shield region then presents an added thermal barrier to heat removal from the package following the fire; however, the thermal energy absorbed in the process of melting and volatizing the resin material of the neutron shielding was conservatively neglected, and was not subtracted from the heat input to the package during the fire.

(9) For the NAC LWT, the ethylene glycol and water mixture comprising the package's neutron shielding was assumed to remain in liquid form during the fire until the average temperature in the shield tank reached the boiling point of the fluid. The fluid in the expansion tank was treated in a similar manner. This conservative approach acts to maximize the heat input into the package during the fire. After the average temperature in the tank exceeded the boiling point of the fluid, heat transfer through the tank was reduced to conduction and thermal radiation through air. As a result, the neutron shield region then presents an added thermal barrier to heat removal from the package; however, the thermal energy absorbed in the process of boiling off the large mass of liquid was conservatively neglected, and was not subtracted from the heat input to the package.

(10) In all three analyses, the package was assumed to be only 66 ft (20 m) from the center of the fire, in order to obtain the highest possible boundary temperatures due to the fire. Based on Department of Transportation regulations [12] that require rail cars carrying radioactive materials to be separated by at least one rail car (a buffer car) from other cars carrying hazardous materials or flammable liquids, 66 ft (20 m) is the shortest possible distance in this fire scenario between a hypothetical rail car carrying an SNF package and the tank car carrying liquid tripropylene.

Given these assumptions, the ANSYS and COBRA-SFS analyses constitute conservative evaluations of the response of the spent fuel transportation packages. The FDS simulations for the NIST model of the Howard Street tunnel fire produced detailed predictions of gas flow rates, gas temperatures, and tunnel wall, ceiling, and floor temperatures during the 7-hour fire and 23-hour post-fire cool down.

6.1.1 Boundary Temperatures from FDS

The FDS simulations included the entire tunnel length, from the west portal (tunnel entrance) to the east portal (tunnel exit). The results obtained for the radial plane at the location 66 ft (20 m) from the center of the fire were used to define the boundary conditions for the analyses with COBRA-SFS and ANSYS. As a conservative simplification of the finely detailed noding in the FDS simulation, the tunnel radial geometry was divided into three regions; top, side, and bottom (see Figure 5.4). Within each of these regions, the predicted peak wall temperatures and peak gas temperatures as a function of time (with the associated gas velocities) were taken as representative of the transient behavior of the entire region, rather than following the local gradients obtained in the detailed NIST simulation with FDS.

The peak temperature-vs.-time and velocity-vs.-time values from the FDS simulation were smoothed to conservatively remove the rapid stochastic variations typical of dynamic fire behavior, preserving only the major peaks and troughs related to the general physical behavior of the simulated fire. (The selected FDS results for this simulation are shown graphically in Appendix D, along with the smoothed values used in the ANSYS and COBRA-SFS calculations.) Figure 6.1 shows these smoothed peak air temperatures for the top, sides, and bottom regions in the tunnel at 66 ft (20 m) from the fire center. The smoothed peak surface temperatures for the walls, floor, and ceiling of the tunnel at this location are shown in Figure 6.2. Figure 6.3 shows the smoothed velocities predicted in the NIST analyses at the locations of the peak gas temperatures shown in Figure 6.1.

The gas temperatures (Figure 6.1) and velocities (Figure 6.3) were used to define convection heat transfer on the top, side, and bottom regions of the package surfaces. The peak tunnel surface temperatures (Figure 6.2) were used to define the boundary conditions for radiation heat transfer between tunnel surfaces and the exposed surfaces of the package. For the ANSYS models of the HI-STAR 100 and LWT packages, these temperatures were applied to corresponding tunnel surface elements comprising the ceiling, walls, and floor. For the COBRA-SFS model of the TN-68 package, radiation exchange with the tunnel walls, ceiling, and floor was incorporated by calculating a radiation heat flux at the package surface using the local package surface temperature and the regional tunnel surface temperatures defined in Figure 6.2. Blackbody view factors between the package surface and the tunnel surfaces were determined using a conventional ray-tracing scheme. (These view factors are listed in Appendix E.)

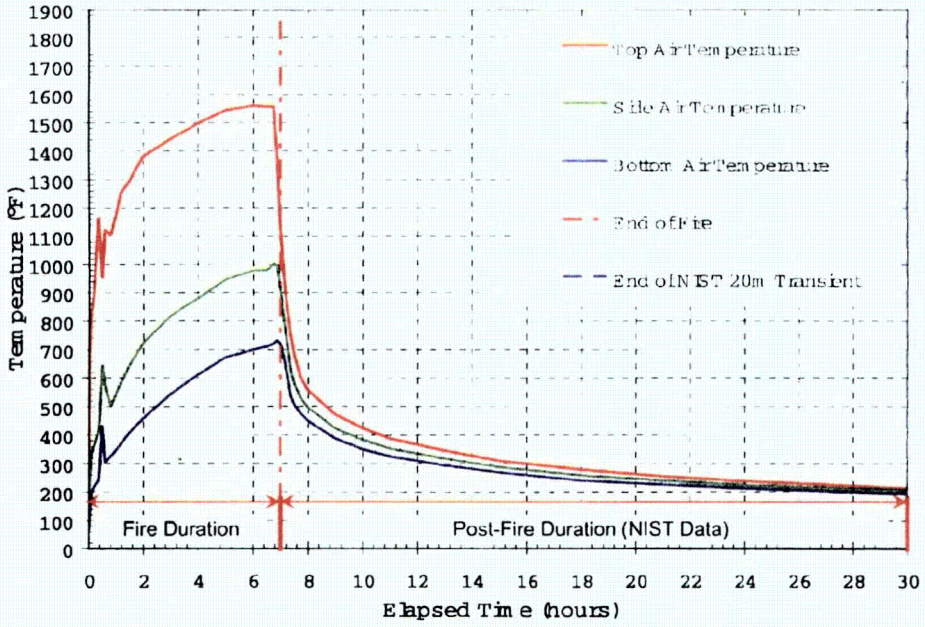

Figure 6.1. BTF Peak Transient Ambient Air Temperatures (smoothed values, NIST 20-m data)

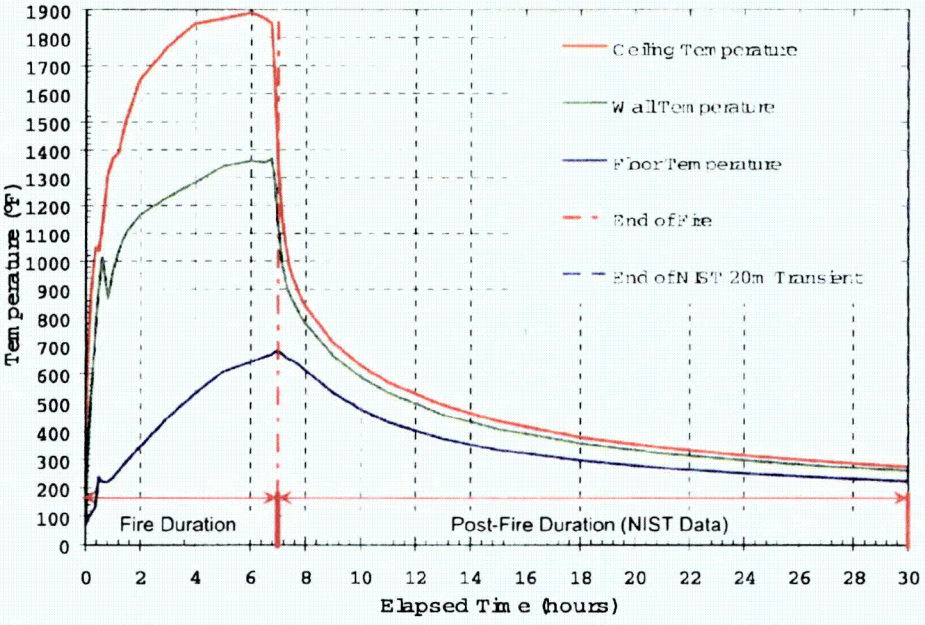

Figure 6.2. BTF Peak Transient Tunnel Surface Temperatures for Floor, Walls, and Ceiling (smoothed values, NIST 20-m data)

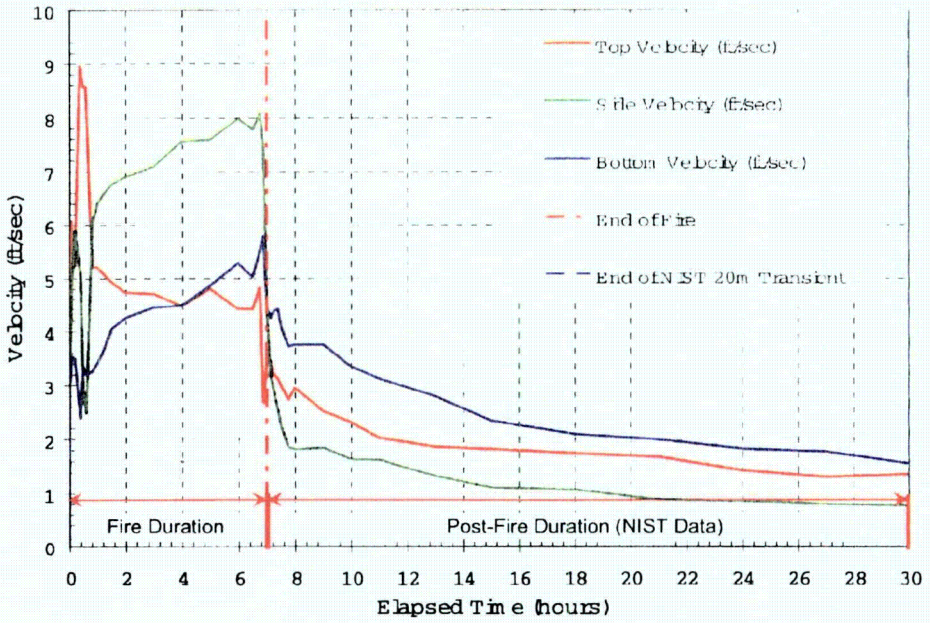

Figure 6.3. BTF Peak Transient Horizontal Velocities near Package Surface (smoothed values, NIST 20-m data)

6.1.2 Convection and Radiative Heat Transfer Boundary Conditions

The NIST analyses showed that the thermal gradients created in the tunnel due to the fire would result in significant air flow past a body located near the fire. This fire-forced convection would significantly affect heat transfer around the package and could have a strong influence on the package outer shell surface temperatures. The smoothed air temperatures in Figure 6.1 and velocities in Figure 6.3 were used to define local time-dependent Nusselt number values at the top, sides and bottom of the package. These values were used to define the local surface heat transfer coefficient for the three computational models.

To maintain consistency between the three models, the same Nusselt number correlation was used to define convection heat transfer at the package surface. The selected correlation gives the Nusselt number for gas flow over a flat or slightly curved surface at zero angle of attack [19], and has the form

for laminar flow ($Re_L < 500{,}000$), $\quad Nu_L = 0.665\, Re_L^{1/2}\, Pr^{1/3}$

for turbulent flow ($Re_L > 500{,}000$), $\quad Nu_L = 0.032\, Re_L^{0.8}\, Pr^{1/3}$

The characteristic length, L, used to define the Nusselt number and Reynolds number for this application is the package body horizontal length. For the TN-68, a value of 160 inches was used, and for the HI-STAR 100, a value of 173 inches was used. Both were based on the length of exposed package body. For the NAC LWT, a value of 240 inches was used, based on the ISO container wetted surface length.

The peak air temperatures (see Figure 6.1) from the NIST analysis define the ambient sink temperature around the package during the fire and post-fire intervals. The Nusselt number defines the rate of heat transfer from the package surface, which allows both codes (COBRA-SFS and ANSYS) to calculate the convection heat flux at the package surface. Using the above relationship, local surface temperatures, T_s, are calculated, and the convection component of the heat flux at the surface is solved for using the formula

$$q''_{conv} = Nu_L \frac{k}{L}(T_s - T_{air})$$

where k = thermal conductivity of ambient air
L = characteristic length
T_s = package surface temperature
T_{air} = ambient external air temperature.

Separate boundary types were defined for the top, sides, and bottom surfaces of the package using the external air temperatures shown in Figure 6.1. The velocities in Figure 6.3 were used to define the Reynolds number so the boundary conditions on the package could change with time as the transient proceeded. Figure 6.4 shows the resulting local convection heat transfer coefficients calculated at the top, sides and bottom of the TN-68 package with the COBRA-SFS model during the 30 hours of the NIST transient simulation.

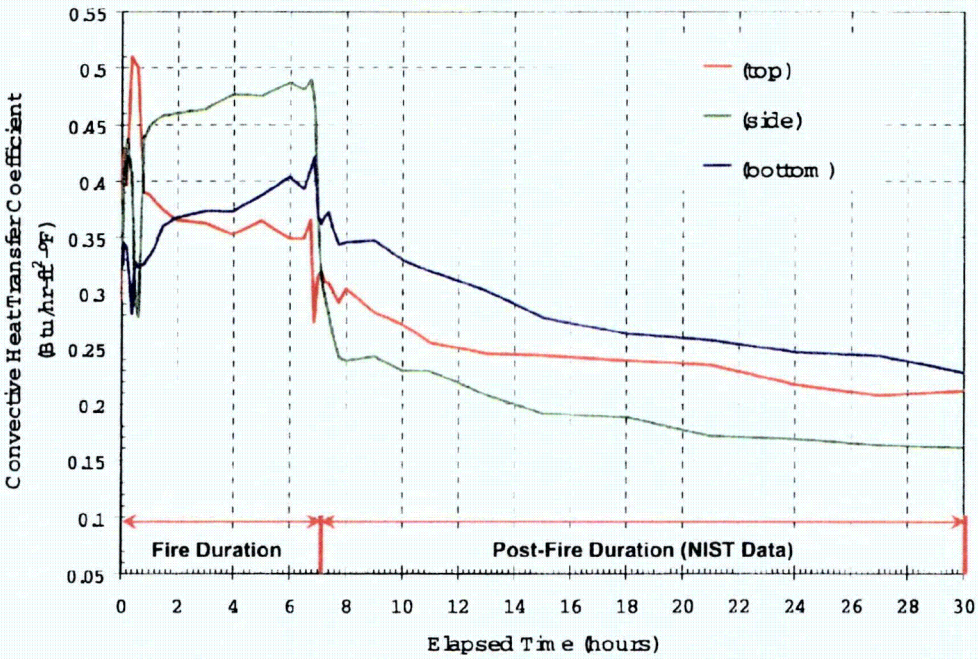

Figure 6.4. Convection Heat Transfer Coefficients at Package Surface from NIST 20 m Air Temperature and Velocity Predictions

In addition to convection heat transfer between the transport package and the surrounding air during the transient, radiation heat transfer between the package surface and the tunnel ceiling, walls, and floor was also captured. Boundary conditions to define radiation heat transfer between the package surface and the tunnel ceiling, walls, and floor were included in the COBRA-SFS model in the following fashion. The total heat flux at the surface of the package is the sum of the two components:

$$q'' = q''_{conv} + q''_{rad}$$

The tunnel surface temperature profiles shown in Figure 6.2 were used to define the radiation heat flux as an additional boundary condition at the package surface using the relationship

$$q''_{rad} = \varepsilon_i B_{ij} \sigma_{SB} \left(T^4_{package} - T^4_{surf} \right)$$

where
ε_i = emissivity of surface i
B_{ij} = blackbody viewfactor from surface i to j
σ_{SB} = Stefan-Boltzmann constant
T_{surf} = tunnel ceiling, wall or floor surface temperature
$T_{package}$ = package surface temperature.

The blackbody view factors between the package surface and the tunnel ceiling, walls, and floor were determined using a Monte Carlo ray tracing scheme based on the package diameter and a uniform axial node length along the length of the package. (See Appendix E.)

Radiation interaction between the tunnel surfaces and the package surfaces in the HI-STAR 100 model was established through the use of ANSYS superelement definitions, as described in Section 5 above. (The same approach was used to define thermal radiation between the tunnel and the ISO container surfaces in the NAC LWT system) The NIST tunnel surface temperature predictions (see Figure 6.2) were then used to establish the tunnel surface boundary condition temperatures. The emissivity of all tunnel surfaces and the package surface was assumed to be 0.9 for all evaluations during the fire and post-fire transient.

6.1.3 Extrapolated Boundary Conditions for Long-Term Cool Down

NIST's FDS analysis was carried out for a 7-hour fire and 23-hour post-fire cool-down. To determine the long-term temperature responses and explore the effects of prolonged exposure to post-fire conditions in the tunnel, the transient was extended to 300 hours (293 hours after the end of the fire). Temperatures predicted in the NIST analysis for 30 hours were extrapolated from 30 hours to 300 hours using a power function to realistically model cool-down of the tunnel environment. The extrapolated values are presented in Figures 6.5 for the air temperatures and in Figure 6.6 for the wall temperatures.

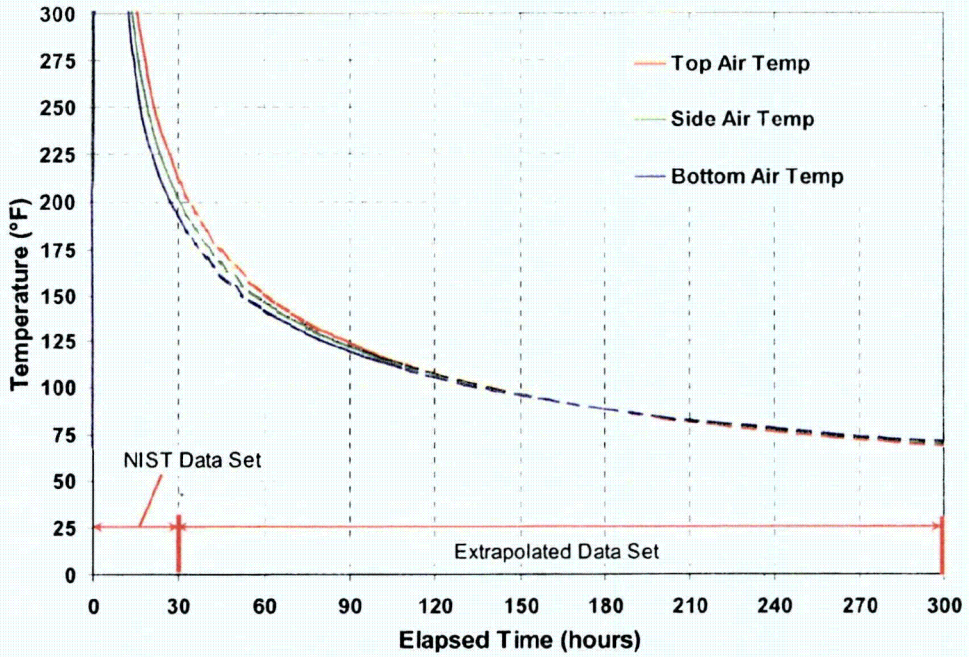

Figure 6.5. BTF Peak Transient Air Temperatures for Top, Side, and Bottom Regions (NIST Data Set and Extrapolated Values)

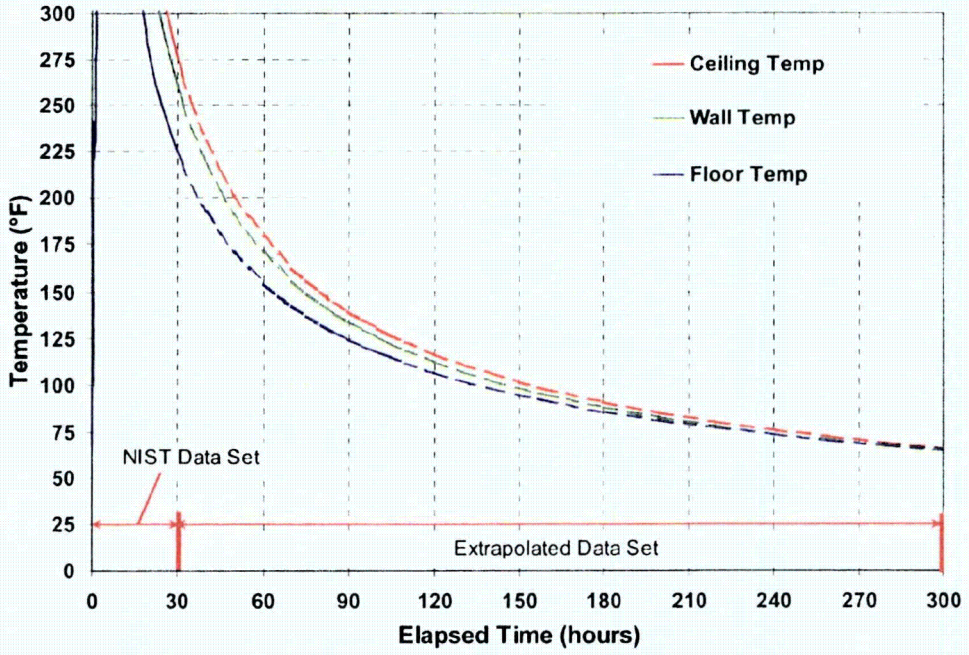

Figure 6.6. BTF Peak Transient Surface Temperatures for Floor, Walls, and Ceiling (NIST Data Set and Extrapolated Values)

About 20 hours into the transient, the velocities predicted in the NIST calculations have dropped to values of 1 to 2 ft/s (0.3 to 0.6 m/s) or less (refer to Figure 6.3). Heat transfer at the package surface for these flow conditions is a complex mixture of forced convection (due to air flow induced in the tunnel by the wall temperature gradients of the fire) and free convection (driven by the non-uniform circumferential temperatures of the package outer shell). At velocities below about 3 to 5 ft/s (1 to 1.5 m/s), heat transfer rates predicted assuming forced convection are generally lower than the heat transfer rates due to natural convection around the package body for these temperature conditions.

To avoid the modeling uncertainties associated with mixed-mode heat transfer, forced convection only was assumed until the end of the NIST simulation, at 30 hours into the transient. From 30 hours to 300 hours, the heat transfer was assumed to be natural convection only. This ensured a conservative treatment of convection heat transfer from the package surface during the entire calculation, since free convection to surface heat transfer from the package is ignored in the cool down from 7 to 30 hours, and forced convection is neglected in the period from 30 to 300 hours.

For consistency, the natural or buoyant convection coefficients were those utilized for determining the pre-fire component temperature distributions (i.e., Hot-Normal Conditions of Transport, as defined in 10 CFR 71.71(c)(1)([1]). The heat transfer coefficients were defined for the appropriate surface geometries using the following relationships [20]:

For flow along a vertical plane or cylinder :

--laminar flow ($10^4 < Gr_f \cdot Pr_f < 10^9$) $\quad h = 1.42\left(\frac{\Delta T}{L}\right)^{1/4}$

--turbulent flow ($Gr_f \cdot Pr_f > 10^9$) $\quad h = 1.31(\Delta T)^{1/3}$

where
- h = heat transfer coefficient, $W/(m - °C)$
- ΔT = $T_w - T_\infty$, $°C$
- T_w = surface or wall temperature, $°C$
- T_∞ = ambient temperature, $°C$
- L = vertical or horizontal dimension, m
- Gr_f = Grashoff number of the gas at film temperature,
- Pr_f = Prandtl number of the gas at film temperature

where film temperature is $T_f = (T_w + T_\infty)/2$

For flow over a horizontal cylinder:

--laminar flow ($10^4 < Gr_f \cdot Pr_f < 10^9$) $\quad h = 1.32\left(\frac{\Delta T}{d}\right)^{1/4}$

where d = diameter, m

--turbulent flow ($Gr_f \cdot Pr_f > 10^9$) $\quad h = 1.24(\Delta T)^{1/3}$

For flow over a horizontal heated plate facing upward (cool side facing downward):

-- laminar flow ($10^4 < Gr_f \cdot Pr_f < 10^9$) $\quad h = 1.32\left(\frac{\Delta T}{L}\right)^{1/4}$

-- turbulent flow ($Gr_f \cdot Pr_f > 10^9$) $\quad h = 1.52(\Delta T)^{1/3}$

For laminar flow ($10^4 < Gr_f \cdot Pr_f < 10^9$) over a heated plate facing downward (cool side facing upward):

$$h = 0.59\left(\frac{\Delta T}{L}\right)^{1/4}$$

Definitions of material properties for use with these correlations were taken from Table A-3 of Kreith [21].

6.1.4 Heat Transfer through NAC LWT Liquid Neutron Shield

An empirical relationship for effective conductivity incorporating the effects of both conduction and convection was used to determine heat exchange through the liquid neutron shield. In the SAR analysis for the LWT package [11], the effective conductivity of the ethylene glycol mixture for conditions below 350°F was determined using the correlation of Bucholz [22], which defines the ratio of the effective conductivity to the actual thermal conductivity as equal to the Nusselt number, such that

$$\frac{k_{eff}}{k_c} = Nu = 0.135(Pr^2\, Gr/(1.36 + Pr))^{0.278}$$

where k_{eff} = effective thermal conductivity of material
k_c = thermal conductivity of motionless fluid
Nu = Nusselt number
Pr = Prandtl number
Gr = Grashoff number

The Baltimore tunnel fire transient is outside the range of the Bucholz correlation, and it yields unrealistically large values for k_{eff} for these conditions. An alternative correlation from Raithby and Hollands [18], based on heat transfer between two concentric cylinders, was used in this analysis instead. This correlation produces reasonable values of k_{eff}, and the transient conditions are generally within its applicable range. The form of this correlation is similar to the Bucholz correlation in that it equates the Nusselt number to the ratio of the effective conductivity over the actual conductivity, but in the Raithby and Hollands formulation, the Nusselt number is expressed as

$$\frac{k_{eff}}{k_c} = Nu = 0.386 D_r (Pr/(0.861 + Pr))^{0.25}\, Ra^{0.25}$$

where Ra = Rayleigh number (Ra = Pr*Gr)
Gr = Grashoff number (based on the temperature difference across the annular gap)

The variable D_t is a dimensionless parameter based on the geometry of the annulus, and is defined:

$$D_t = \frac{\ln(D_o / D_i)}{d^{3/4}(1/D_i^{3/5} + 1/D_o^{3/5})^{5/4}}$$

where D_o = annulus outer diameter
D_i = annulus inner diameter
d = width of annulus.

Figure 6.7 shows a plot of the Nusselt number predicted with these two correlations for the liquid (56% ethylene glycol and water mixture) in the neutron shield annulus. Figure 6.8 shows the effective conductivity for the annulus as a function of the average temperature and temperature difference for the liquid neutron shield tank. Figure 6.9 shows the same relationship for the expansion tank. (The sharp discontinuity in the curves on both plots represents the phase change when the average temperature of the liquid reaches the boiling point of the ethylene glycol and water mixture.) For low values of the temperature difference, the results approach those for the conduction-only case.

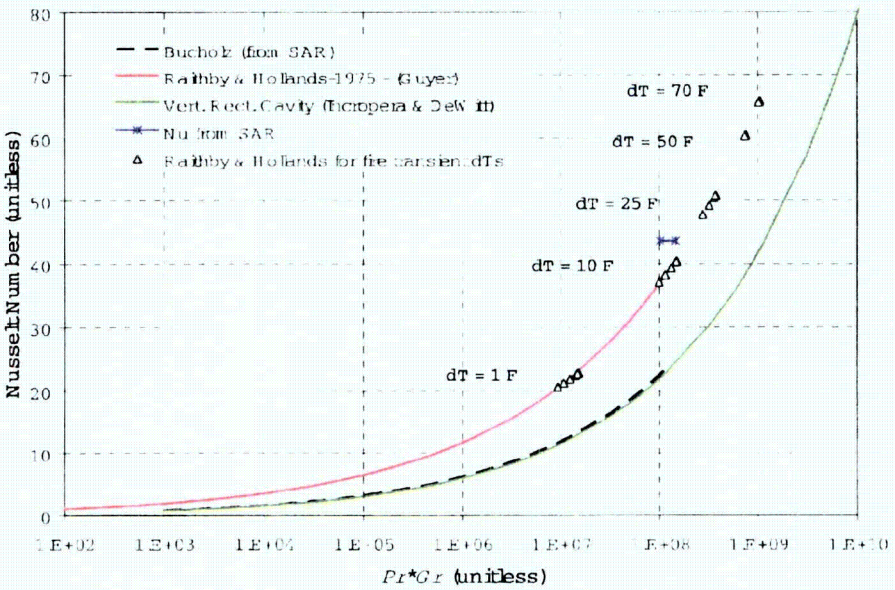

Figure 6.7. Nusselt Number for Heat Transfer in Liquid Neutron Shield

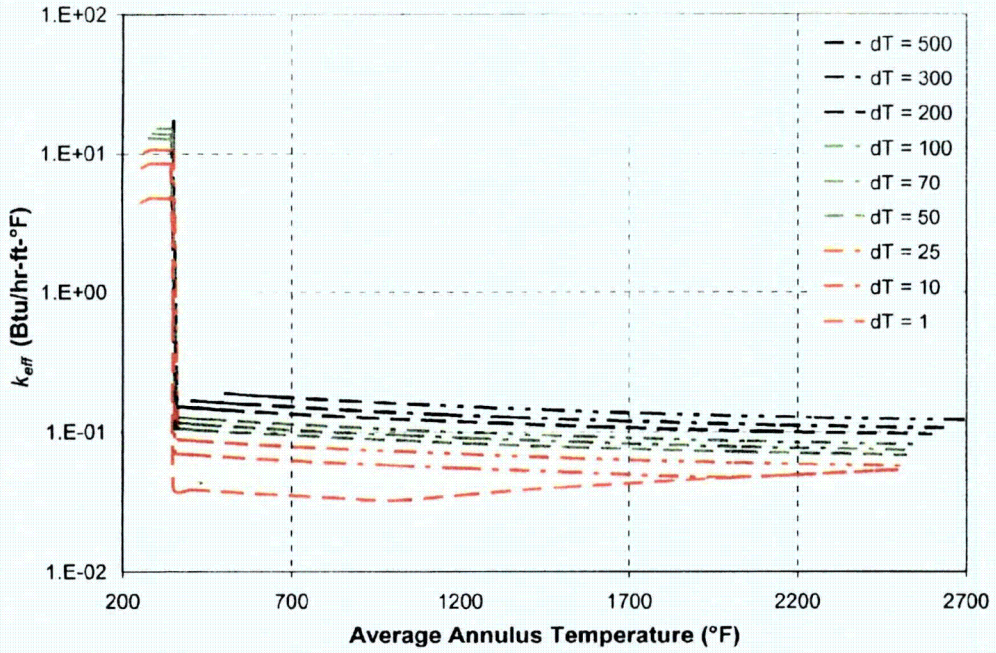

Figure 6.8. Effective Conductivity of Neutron Shield Tank Contents

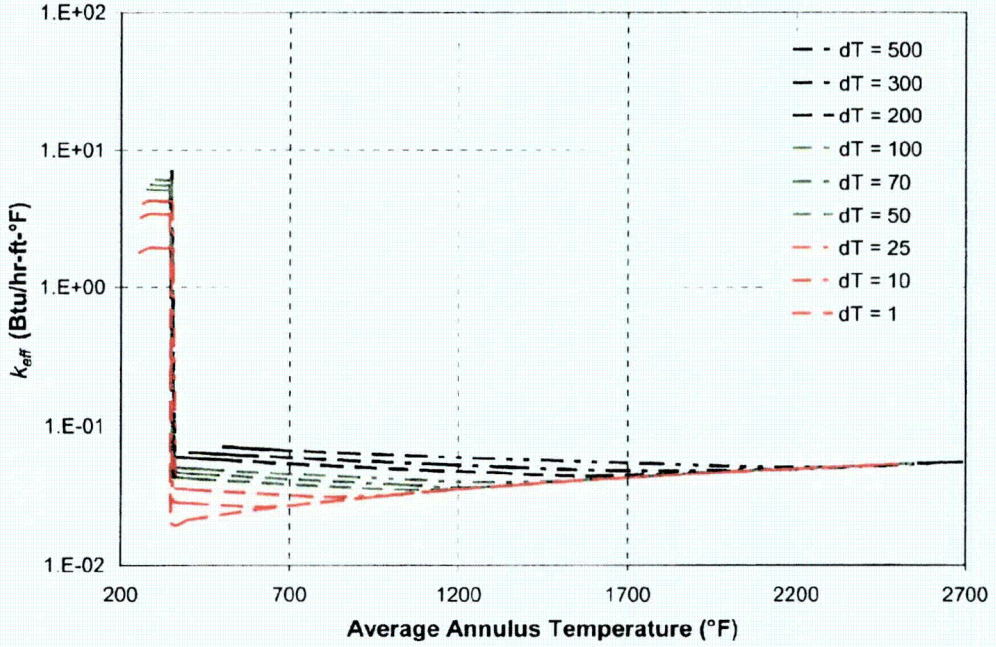

Figure 6.9. Effective Conductivity of Expansion Tank Contents

6.1.5 Heat Transfer through NAC LWT Lead Gamma Shield

Temperatures encountered in the Baltimore tunnel fire scenario are high enough to expect that the lead gamma shielding in the NAC LWT would melt in the fire transient. It would be conservative to neglect this process in the thermal analysis, since taking into account the thermal effects of lead melting would tend to slow the rate of heat input into the package. The melting of the lead absorbs energy from the fire due to the latent heat of fusion, which for lead is 10.4 Btu/lbm (24.2 kJ/kg). The lead shielding consists of about 27,134 lbm (12,308 kg) of lead, and would absorb approximately 83 kW-hr in the process of phase change. This heat would otherwise be conducted through the lead shielding to the package interior, contributing to higher basket and fuel temperatures within the package. In addition, the local temperature of the lead cannot rise above the melting temperature until the phase change is complete at that point. This will tend to slow the rate of temperature increase in the gamma shield region, and therefore slow the overall rate of temperature increase for the package internals. The thermal conductivity of molten lead is approximately 50% lower than that of solid lead. This lower conductivity would further slow the rate of heat input to the package during the hottest portion of the fire.

However, the behavior of the lead as shielding material is also an important consideration in the analysis of the response of the NAC LWT to the fire scenario. Complete evaluation of the transient requires a realistic representation of the thermal response of the package, including the effects of melting and resolidification of the material in the course of the transient. Including the effect of phase change in the lead comprising the gamma shield of the NAC LWT package involves two major considerations in the specification of the lead material properties. First, the energy absorbed in the process of melting the material must be taken into account in the process of determining the local material temperature. Second, the thermal conductivity for elements representing this material must include values for both solid and molten conditions as a function of temperature.

Figure 6.10 shows the enthalpy of lead as a function of temperature, including the 'jump' at the point of phase change. This step change corresponds to the latent heat of fusion for lead. Figure 6.11 shows the thermal conductivity for lead as a function of temperature used in the ANSYS analysis, compared to the values used for this material property from the package SAR [11]. (See Appendix C, Table C.6 for the thermal properties of lead used in this analysis.) The solid phase values from the SAR at temperatures approaching the melting point of lead conservatively ramp down to an average value of thermal conductivity for the liquid phase. The actual thermal conductivity of lead remains at a relatively high value for the solid phase all the way to the melting temperature. Upon melting, the thermal conductivity drops by more than 50%, then gradually increases with increasing temperature of the molten material.

6.2 Initial System Component Temperatures

The normal conditions of transport described in 10 CFR 71.71 [1] were used as initial conditions for each analysis. All three packages were subjected to an ambient temperature of 100°F (38°C), with solar insolation. For pre-fire conditions, the package surface was given an emissivity value representative of its surface finish (e.g., 0.3 for bare stainless steel, 0.85 for painted surfaces). In the ANSYS models for the HI-STAR 100 and NAC LWT systems, thermal radiation heat transfer to ambient was modeled using surface effect elements (SURF152).

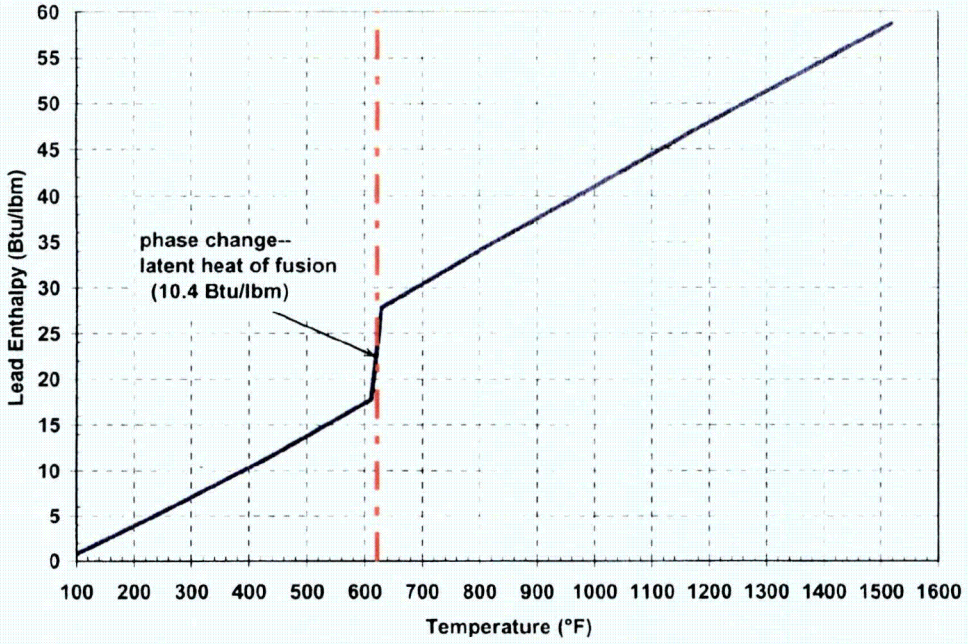

Figure 6.10. Solid and Molten Lead: Enthalpy as a Function of Temperature

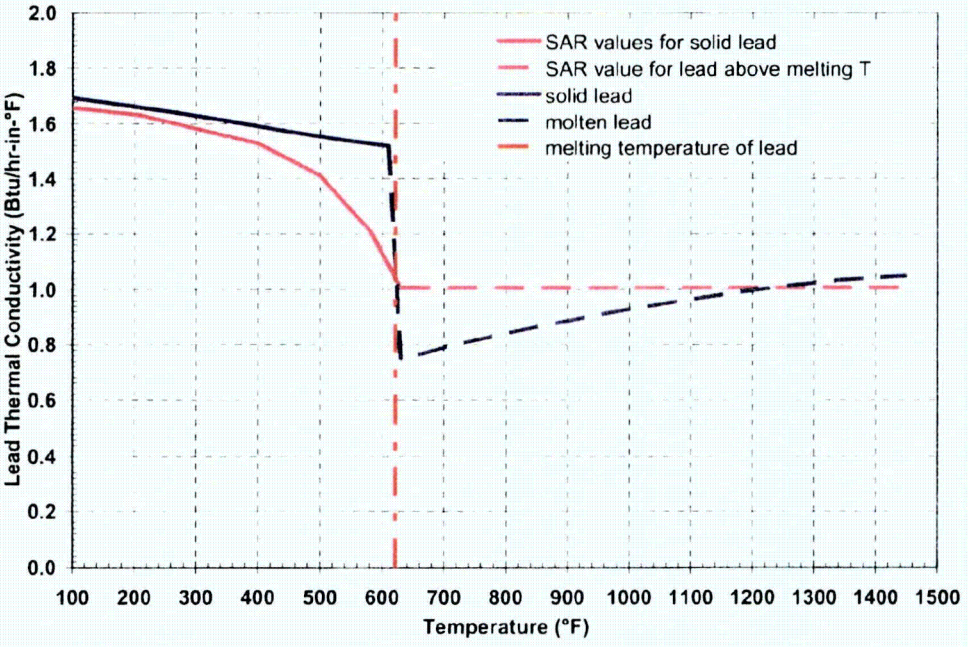

Figure 6.11. Solid and Molten Lead: Thermal Conductivity as a Function of Temperature

Convection from the surface of each package was modeled with a similar set of surface effect elements. The natural convection correlations for buoyancy driven flow discussed above were used to simulate convection heat transfer at the package surface. For the COBRA-SFS model of the TN-68 package, the surface boundary conditions also included natural convection and thermal radiation.

For the TN-68, the heat generation rate was specified as 72,334 Btu/hr (21.2 kW). For the HOLTEC HI-STAR 100, the heat generation rate was specified for a decay heat load of 68,240 Btu/hr (20 kW). For the NAC LWT, the heat generation rate was specified as 8,530 Btu/hr (2.5 kW). For all three packages, appropriate peaking factors (as reported in the respective SAR documents), were applied over the active fuel region.

A steady state normal condition temperature distribution for each package was obtained to establish pre-fire conditions. The hot-normal condition temperatures for each package were verified against the results reported in the relevant SAR. Normal condition temperatures from the ANSYS solution for the HI-STAR 100 are provided in Figure 6.12. (Appendix F contains additional plots showing the detailed steady-state temperature distributions for these conditions predicted for the HI-STAR 100.) The peak clad temperature predicted with ANSYS for the HI-STAR 100 is 738°F (392°C), compared to 701°F (372°C) reported in the SAR[10].

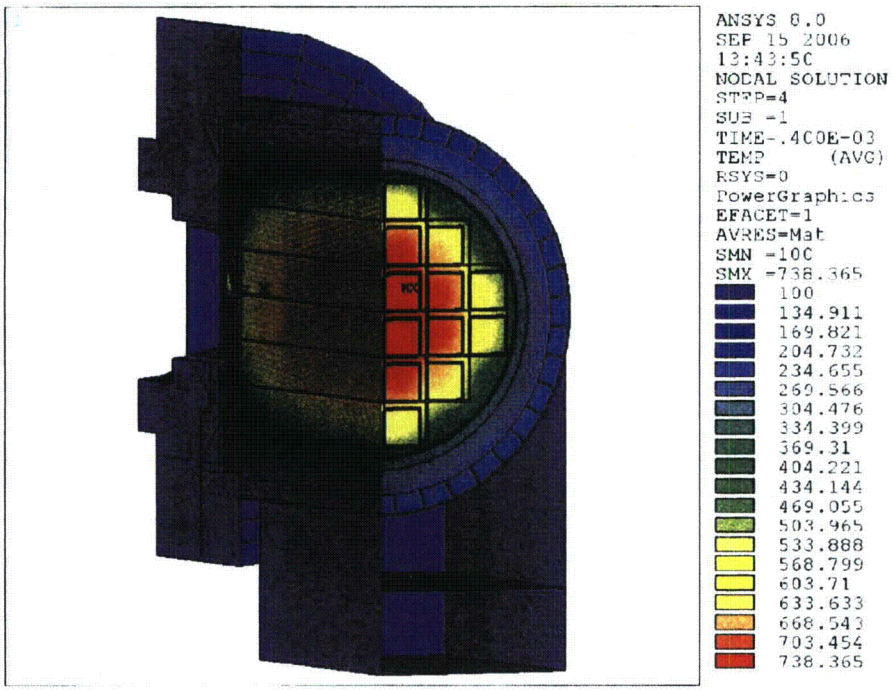

Figure 6.12. HI-STAR 100 Package Hot-Normal Condition Temperature Distribution

Since COBRA-SFS does not have a graphical post-processing module, it is not possible to produce similar color-flooded thermographs for the TN-68 evaluation. However, the analysis results are similarly

in very good agreement with the corresponding SAR values. The COBRA-SFS calculations predicted a peak clad temperature of 485°F (252°C) in the TN-68 package, compared to 490°F (254°C) reported in the TN-68 SAR [9].

Component temperature comparisons of results determined in this study and those published in the applicant's SAR documentation are presented in Table 6.1 for the TN-68 analysis with COBRA-SFS and Table 6.2 for the HI-STAR 100 analysis with ANSYS.

Table 6.1. TN-68 Hot-Normal Component Temperatures

Component	Current Study (COBRA-SFS) °F (°C)	SAR Values °F (°C) (Table 3-1 [9])
Fuel Cladding	485 (252)	490 (254)
Basket plate	467 (242)	469 (243)
Basket Rail	332 (167)	319 (159)
Inner Shell	292 (144)	262 (128)
Gamma Shell	285 (141)	260 (127)
Package Bottom	261 (127)	254 (123)
Seals	260 (127)	234 (112)
Radial Neutron Shield	256 (124)	244 (118)
Outer Shell	243 (117)	204 (96)

Table 6.2. HOLTEC HI-STAR 100 Hot-Normal Component Temperatures

Component	Current Study (ANSYS) °F (°C)	SAR Values °F (°C) (Table 3.4.10 [10])
Fuel Cladding	738 (392)	701 (372)
MPC Basket Centerline	717 (381)	667 (353)
MPC Basket Periphery	447 (231)	430 (221)
MPC Outer Shell	347 (175)	315 (157)
MPC/Overpack Helium Gap Outer Surface	299 (148)	291 (144)
Radial Neutron Shield Inner Surface	258 (126)	271 (133)
Overpack Enclosure Shell Surface	253 (123)	222 (106)
Axial Neutron Shield	228 (109)	292 (144)
Impact Limiter Exposed Surface	165 (74)	121 (49)
Overpack Closure Plate	270 (132)**	163 (73)
Overpack Bottom Plate	409 (209)**	295 (146)

** Temperatures elevated due to superimposed gap conductance between impact limiters and cask body. This gap conductance is replaced with intimate contact during the fire duration.

These tables show that the analytical results obtained for the TN-68 and HI-STAR 100 are in very good agreement with the results presented for the corresponding cases in the respective SARs. Minor differences between the SAR results and those obtained in the current study are due to differences in modeling detail and simplifying assumptions employed in the SAR models. For example, the SAR analysis of the HI-STAR 100 neglects the effect of the support cradle and possible limited gap conductance on component temperatures in the evaluation for the hot-normal conditions of transport.

For the TN-68 model and the HI-STAR 100 model, the results presented in Tables 6.1 and 6.2 are the initial conditions for the fire transient analysis. For the NAC LWT, the steady-state initial conditions for the fire transient analysis were based on similar assumptions, but direct comparison with the steady-state results presented in the SAR is not possible, due to the large number of significant differences between the approach used in the SAR analyses and the detailed modeling approach used in the current study

In the 3-D ANSYS model of the NAC LWT (shown in Figures 5.18 and 5.19), convection from the surface of the ISO container was modeled with a set of surface effect elements similar to those used in the model of the HI-STAR 100. The natural convection correlations for buoyancy-driven flow described in Section 6.1.3 were used to simulate the convective heat transfer within the ISO container and on the external surface. A heat generation rate equivalent to a decay heat load of 8,530 Btu/hr (2.5 kW) was applied, with appropriate peaking factor, over the active fuel region. This value was selected because the bounding thermal evaluation in the SAR [11] for the NAC LWT is for an intact PWR fuel assembly with a maximum decay heat load of 2.5 kW. This approach ensures a conservative decay heat load for the package in the fire transient analysis.

The steady-state initial condition temperature distribution predicted for the NAC LWT package was compared to the results reported in the SAR [11], but direct correspondence between the two sets of results is not to be expected, because the SAR [11] does not include any analytical cases similar to the detailed 3-D model used in the current study. Due to the relatively low associated decay heat load capacity of the package, the applicant chose to perform a series of highly conservative evaluations using much simpler models to qualify the system for its Certificate of Compliance (CoC).

The most complex models presented in the SAR [11] involve simple 2-D ANSYS cross-sections in which the cutting plane includes the expansion tank as well as the neutron shield tank. This approach does not allow axial heat flow out of the plane of the 2-D cross-section, and also assumes that the decay heat load axial peak occurs on that cutting plane, placing the spent nuclear fuel peak decay heat location under two concentric neutron shields. This provides conservatism for a steady-state analysis, since the expansion tank makes a longer conduction path over which to dissipate the decay heat. For the fire transient, however, the assumptions in this 2-D model would have the effect of limiting the heat input to the package from the fire, and would not constitute a conservative approach.

ANSYS 2-D cross-sectional models were also used in the SAR [11] to represent a 1.41 kW 25-rod BWR basket assembly and a 2.1 kW high burn-up PWR assembly, with detailed representation of the fuel pins, pin tubes, and can weldments with the pins resting on the pin tubes via point contact. These models included the ISO container, with boundary conditions that included solar insolation and 100°F (38°C) ambient temperature. The design basis model presented in Amendment 34 of the SAR [11] for a 2.5 kW

PWR assembly also used a 2D representation of the package. This is a HEATING5 model, and consists of a 2-D axisymmetric representation using effective diameters for the basket and fuel assembly. This model does not include an ISO container or impact limiters, convection at the assembly end cavities is neglected, and the ambient temperature boundary is specified as 130°F (54°C).

None of these cases from the SAR [11] use assumptions or boundary conditions identical to the initial conditions assumed for the fire transient in this analysis, but there are sufficient similarities to allow reasonable comparisons to be made for verification of the 3-D ANSYS model predictions. The results for these three cases are reported in Table 6.3.

Table 6.3. NAC LWT Component Temperatures at Various Decay Heat Loads

Component	2.5 kW °F (°C) (Table 3.4-2 [11])	1.41 kW °F (°C) (Table 3.4-7 [11])	2.1 kW °F (°C) (Table 3.4-10 [11])
Fuel Cladding	472 (244)	358 (181)	671 (355)
Aluminum PWR Insert	276 (136)	*	394 (201)
Inner Shell	274 (134)	249 (121)	385 (196)
Gamma Shield	273 (134)	248 (120)	375 (191)
Outer Package Surface	229 (109)	185 (85)	308 (153)
Neutron Shield	238 (114)	235 (113)	306 (152)
Lid Seal	227 (108)	*	*
Drain/Vent Ports	231 (111)	*	*
Impact Limiters	*	*	*
ISO Container	*	*	*

* value not reported by applicant

Figure 6.13 shows the predicted temperature distribution from the ANSYS solution for the 3-D model developed for the current study, obtained using 130°F (54°C) ambient temperature with a 2.5 kW decay heat load. This calculation was performed in addition to the initial conditions case at 100°F (38°C) ambient temperature, as a verification case for comparison to the results obtained for the 2.5 kW case reported in the SAR [11]. The 2-D axisymmetric model in the SAR [11], which used an ambient temperature of 130°F (54°C), is the most similar to the initial conditions in the fire transient for the purposes of this comparison, despite the exclusion of the ISO container.

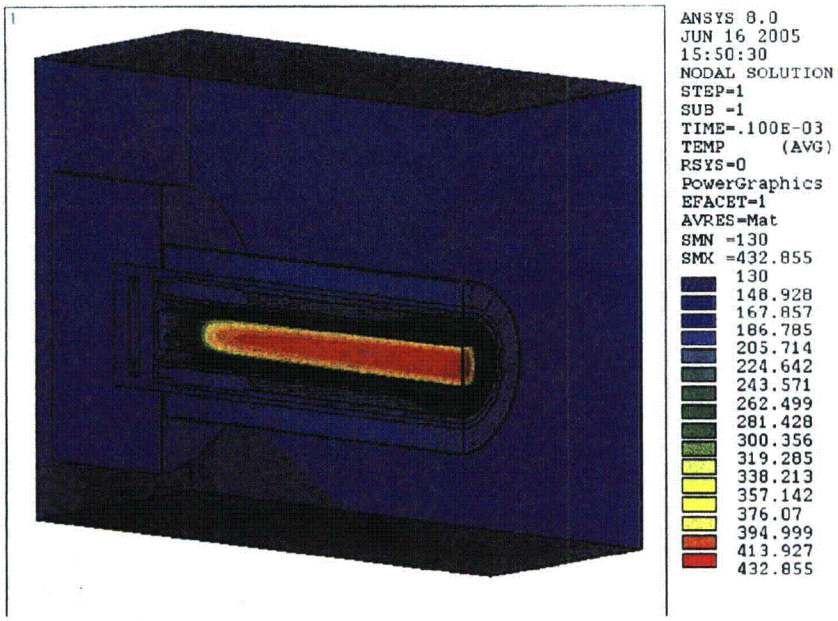

Figure 6.13. LWT Package Hot-Normal Condition Temperature Distribution (2.5 kW Decay Heat)

Table 6.4 presents detailed component temperature results obtained with the 3-D ANSYS model, compared to the values published in the SAR [11] for this decay heat load.

Table 6.4. NAC LWT Component Temperatures at 2.5 kW Decay Heat and 130°F Ambient

Component	Current Study (ANSYS) °F (°C)	SAR Values (Table 3.4-2 [11]) °F (°C)	ΔT °F (°C)
Fuel Cladding	434 (223)	472 (244)	38 (21)
Aluminum PWR Insert	265 (129)	276 (136)	11 (6)
Inner Shell	228 (109)	274 (134)	46 (26)
Gamma Shield	227 (108)	273 (134)	46 (26)
Outer Package Surface	200 (93)	229 (109)	29 (16)
Neutron Shield	204 (96)	238 (114)	34 (19)
Lid Seal	164 (73)	227 (108)	63 (35)
Drain/Vent Ports	164 (73)	231 (111)	67 (37)
Impact Limiters	167 (75)	Not Modeled	--
ISO Container	167 (75)	Not Modeled	--

At first glance, the differences between the results obtained with the two models appear to be rather sizable. The peak clad temperature predicted with the ANSYS 3-D model is 434°F (223°C), compared to

472°F (244°C) reported in the SAR [11]. The other temperatures shown in the table are also considerably lower for the ANSYS model, compared to the corresponding SAR values. However, this is an expected result, given the modeling differences between the two cases.

A more significant observation for the purposes of this comparison is to note that the differences in peak component temperatures between the two models are consistent. The radial temperature drop from the peak fuel cladding temperature to the outer package surface temperature is 234 °F (130 °C) for the 3-D ANSYS model used in the current study, compared to a temperature drop of 243 °F (135 °C) for the HEATING5 axisymmetric model used in the SAR [11]. This close agreement strongly suggests that the axisymmetric model featured in the SAR predicts essentially the same temperature distribution as the more detailed ANSYS model used in the current study. Most of the differences in the point-to-point temperatures predicted with each model are due to the differences in assumed external boundary conditions (100°F (38°C) for the current study, compared to 130°F (54°C) in the SAR analysis), and differences in modeling details.

Figure 6.14 shows the temperature distribution predicted with the ANSYS 3-D model for the initial steady-state conditions before the fire transient. The boundary conditions for this calculation are from the Normal Transport Condition case, as described in 10 CFR 71.21 [1].

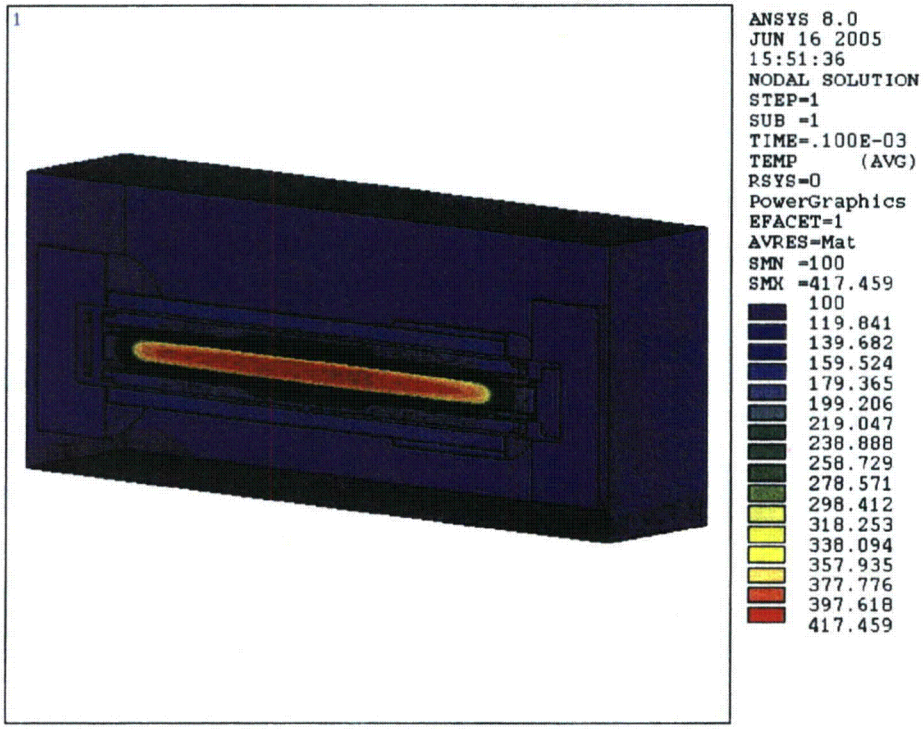

Figure 6.14. LWT Package Normal Condition Temperature Distribution (2.5 kW Decay Heat)

The hottest fuel temperature is predicted to occur near the center of the assembly, at a location that corresponds closely to the cross-section with the highest decay heat (i.e., the location of the maximum axial peaking factor). This location is some distance away from the part of the package covered by the expansion tank. This shows that the assumption placing the peak location under the expansion tank, which was used in the 2-D cross-section model in the SAR [11], is markedly-conservative, and therefore can be expected to yield a higher estimate of the peak temperature.

As shown in Figure 6.14, the temperature gradients in the package are such that heat spreads and dissipates axially as well as radially. As a result, the 3D geometry yields a more realistic representation of the heat flow in the package. The conservative measures used in the simpler 2-D ANSYS cross-sectional models and the HEATING5 axisymmetric cross-sectional model (as reported in the SAR [11]) will tend to result in higher predicted temperatures for steady-state conditions. Other associated modeling assumptions and simplifications, including boundary conditions developed by the applicant, also tend to drive up component temperatures, compared to what might be obtained with a detailed 3-D representation.

The main concern in analyses for normal transport conditions is to determine a conservative rate of heat removal *from* the package. The approach employed in the SAR should yield conservative estimates of peak internal temperatures for the analysis. However, for the fire transient, the main concern is the amount of heat that the external fire can put *into* the package. In the fire transient calculations, a best estimate of component temperature distributions and heat transfer paths is more appropriate.

The conservative approach for the fire analysis in the current study is to choose assumptions that tend to enhance the heat transfer paths, making it easier for heat to move into the package from outside. For example, the treatment of internal gaps between components is conservative in the SAR, in that gaps are assumed to be as large as possible. In the ANSYS model for the fire analysis, the shrinkage gap between the lead shielding and package shell is included during the initial steady-state calculation, but is ignored during the fire transient. This approach tends to minimize heat loss from the package at the initial conditions, but then maximizes the heat input into the package internal components during the fire.

The pre-fire peak component temperature results determined in this study for the Normal Transport Condition case at 100°F (38°C), as described in 10 CFR 71.71 [1], are shown in Table 6.5.

Table 6.5. NAC LWT Pre-Fire Component Temperatures at 2.5 kW Decay Heat Load and 100°F Ambient

Component	Component Temperature °F (°C)
Fuel Cladding	418 (214)
Aluminum PWR Insert	242 (117)
Inner Shell	205 (96)
Gamma Shield	204 (96)
Outer Package Surface	176 (80)
Neutron Shield	180 (82)
Lid Seal	138 (59)
Drain/Vent Ports	138 (59)
Impact Limiters	141 (61)
ISO Container	140 (60)

6.3 Tunnel Fire Evaluations of Rail Packages

The Baltimore tunnel fire simulations for the three transport packages were conducted in three phases. These were the pre-fire steady-state (hot-normal) conditions of transport, the fire (consisting of the first 7 hours of the transient), and the post-fire phase. For the pre-fire steady state, the hot-normal conditions of transport were evaluated with solar insolation and a 100°F (38°C) ambient temperature, according to 10 CFR 71.71(c)(1) [1]. External heat transfer was assumed to be free convection in still air with thermal radiation exchange with the environment. This conservatively established component temperatures to serve as initial conditions for the transient.

For the fire phase of the evaluation ($0 \leq t \leq 7$ hours), the energy input due to solar insolation was set to zero, the tunnel surfaces were introduced, and the transport package and tunnel surfaces were assign an emissivity of 0.9 to represent surfaces affected by sooting. A forced convection regime was assumed to exist on the exterior of the package, based on the gas velocity results from the analysis performed by NIST. These results were used to determine the surface heat transfer coefficient, and with the gas temperatures from the NIST analysis defining the ambient boundary temperature, the convective heat flux at the package surface could be determined in the solution for the local surface temperature. Tunnel wall temperatures were also taken as boundary conditions from the NIST calculations, and thermal radiation exchange between the tunnel walls and the package was also accounted for in the evaluations. In addition to these measures, all aluminum honeycomb, neutron shield resin materials, or wood were assumed to remain intact during the full duration of the fire to maximize heat input during the fire.

For the post-fire phase of the evaluation ($t > 7$ hours), properties of the neutron shield resin materials, wood, and selected portions of aluminum honeycomb sections were replaced with thermal properties

identical to those of air. This change in material properties simulates the degradation of the materials due to the fire and has the effect of reducing the rate of heat release during the post-fire phase. Conservatively, the energy absorbed in the degradation of these materials was not subtracted from the heat input of the fire to the package. Other model-specific conservatisms were also incorporated, as described above in Section 5.

Analysis of the post-fire phase was carried out for a duration of 293 hours. This included the 23 hours of the post-fire portion of the transient predicted by the FDS analysis, plus an additional 270 hours in which boundary conditions at 30 hours were extrapolated to 300 hours, using a power function (as discussed in Section 5 above). Purely forced convection heat transfer correlations (based on the NIST gas velocities and temperatures) were imposed for the post-fire phase of the simulation from 7 hours to 30 hours. The forced convection boundary condition at the package surface was then transitioned to free convection correlations, to establish the buoyant convective coefficients of heat conductance for the remainder of the evaluation period.

Results obtained in the evaluations of the three packages are discussed in Section 7.